

Whereas the first GRB (and its prompt emission) was discovered in 1967, the first GRB afterglow was discovered 30 years later in 1997. Despite the short history of afterglow studies, we know the physics of afterglow much better than that of prompt emission. The reason is that afterglow physics is relatively simple, invoking the interaction between a relativistic jet and an ambient medium. The afterglow model is quite *generic* and is usually independent of the messy physics related to the progenitor (massive star core collapse or compact star coalescence), central engine (a hyper-accreting black hole or a millisecond magnetar), and jet composition (a fireball or a Poynting-flux-dominated jet). As a result, the afterglow theory predated observations (Mészáros and Rees, 1997a), and the model predictions were nicely confirmed by later observations.

On the other hand, afterglow theory covers a wide range of subjects. There are many variants of the models that invoke different dynamics and spectral/temporal regimes. In any case, even with several free parameters, these models have *predictive* power regarding the temporal and spectral indices and their relations, and are therefore *falsifiable*. The inability of these models to account for some observed afterglow data therefore points towards an *internal* origin of the emission, which sheds light on the underlying central engine physics.

This chapter deals with the details of afterglow physics. Section 8.1 deals with the deceleration dynamics in the self-similar regime (no reverse shock), which lays the foundation for calculating afterglow lightcurves. In §8.2, a prescription on how to calculate the characteristic frequencies of the afterglow synchrotron emission is presented. The detailed afterglow models are then introduced in the subsequent sections: §8.3 introduces the standard synchrotron forward shock model in the self-similar regime, with the consideration of different medium profiles (ISM vs. wind) as well as the possibility of energy injection; §8.4 delineates the physics of the *jet break*, i.e. a geometrically collimated jet and its predicted observational signature. The transition from the relativistic phase to the non-relativistic phase is studied in §8.5, and the contribution from the SSC emission component is discussed in §8.6. In §8.7, the afterglow properties during the early deceleration phase with the contribution from a reverse shock are introduced in detail. Some other effects such as neutron decay and pair generation at the radiation front are briefly introduced in §8.8. The theory of afterglow polarization is discussed in §8.9. Finally, we review how the afterglow models confront the afterglow data in §8.10.

8.1 Deceleration Dynamics in the Self-Similar Regime

As discussed in §7.3.4, the GRB blastwave starts to decelerate significantly as the mass collected from the ambient medium becomes comparable to the mass in the jet divided by the bulk Lorentz factor of the blastwave (see Eq. (7.76)). For a *thin shell* (central engine duration shorter than the deceleration time, see definition in §7.3.4), this radius is also about the radius at which a reverse shock crosses the ejecta. We will postpone the details of reverse shock crossing physics to §8.7, and only consider the phase after the reverse shock crossing in this section. This is because the blastwave dynamics in this phase are relatively simple and can serve as an example on how to derive afterglow lightcurves based on the synchrotron radiation model.

8.1.1 Basic Scalings

Once a decelerating blastwave enters the *self-similar* regime (i.e. after the reverse shock crosses the ejecta), its dynamics depend only on the *energy* in the blastwave and the *density* of the circumburst medium (see §8.1.2 below for details). The simplest model invokes a constant energy (adiabatic and no energy injection) and a constant medium density (the case of an interstellar medium, ISM). Built upon this, one may also discuss the dynamics of a blastwave with a varying ambient medium density (e.g. stellar wind), or a varying total energy in the blastwave (e.g. with radiative loss or with energy injection). In the following, we derive the basic scalings of the blastwave dynamics for these cases.

Constant Energy, Constant Density

We first consider the case of a constant energy E (i.e. an adiabatic fireball with no energy loss or energy injection) and a constant medium density n (i.e. ISM) (Mészáros and Rees, 1997a; Sari et al., 1998).

The energy conservation condition may be written as

$$E \simeq V \rho c^2 \hat{\gamma} \Gamma^2 \simeq \frac{4\pi}{3} r^3 n m_p c^2 \cdot \hat{\gamma} \Gamma^2 = \text{const}, \quad (8.1)$$

where the volume the fireball sweeps is $V = (4\pi/3)r^3$, $\rho = n m_p$ is the mass density of the ambient medium, the effective mass energy density in the shocked region is $\sim \hat{\gamma} \Gamma \rho c^2$ (recall that besides the rest mass energy density ρc^2 , it also includes the internal energy density e in the shocked region, which is $\sim \Gamma$ times the upstream rest mass energy density, which is $\gg \rho c^2$, as well as the pressure $p = (\hat{\gamma} - 1)e$), and another factor Γ is the Lorentz boost.

One therefore has $\Gamma^2 r^3 = \text{const}$, or

$$\Gamma \propto r^{-3/2}, \quad r \propto \Gamma^{-2/3}. \quad (8.2)$$

The observer time (t_{obs} , for simplicity hereafter denoted t) is

$$t = t_{\text{obs}} \sim \frac{r}{2\Gamma^2 c} \propto r \Gamma^{-2} \propto \begin{cases} \Gamma^{-2/3} \cdot \Gamma^{-2} \propto \Gamma^{-8/3}, \\ r \cdot r^3 \propto r^4, \end{cases} \quad (8.3)$$

so that one has

$$\Gamma \propto r^{-3/2} \propto t^{-3/8}, \quad r \propto t^{1/4}. \quad (8.4)$$

Constant Energy, Density Stratification

We now introduce a general density profile with a stratification parameter k , i.e.¹

$$n = n_0 \left(\frac{r}{r_0} \right)^{-k}. \quad (8.5)$$

The energy conservation equation can then be written as

$$E \sim \int 4\pi r^2 n_0 \left(\frac{r}{r_0} \right)^{-k} m_p c^2 \hat{\gamma} \Gamma^2 dr = \text{const}, \quad (8.6)$$

or $r^{3-k}\Gamma^2 = \text{const}$. Carrying out the same exercise, one has the observer time

$$t \sim \frac{r}{2\Gamma^2 c} \propto r\Gamma^{-2} \propto \begin{cases} \Gamma^{\frac{2}{k-3}} \cdot \Gamma^{-2} \propto \Gamma^{\frac{8-2k}{k-3}}, \\ r \cdot r^{3-k} \propto r^{4-k}, \end{cases} \quad (8.7)$$

and

$$\Gamma \propto r^{\frac{k-3}{2}} \propto t^{\frac{k-3}{8-2k}}, \quad r \propto t^{\frac{1}{4-k}}. \quad (8.8)$$

These scalings are reduced to (8.4) for $k = 0$ (constant density). For a free wind with constant mass loss rate \dot{M}_w and wind speed v_w (i.e. $\dot{M} = 4\pi r^2 n v_w = \text{const}$), one has $n \propto r^{-2}$ and $k = 2$, which gives the scaling law (Dai and Lu, 1998b; Chevalier and Li, 1999)

$$\Gamma \propto r^{-1/2} \propto t^{-1/4}, \quad r \propto t^{1/2}. \quad (8.9)$$

Radiative Fireball

If the blastwave is highly radiative, i.e. all the shocked energy is emitted away quickly, one has a radiative fireball. Energy is decreasing with time.

Let us consider the constant density case as an example. Instead of having a constant blastwave energy $E \propto nr^3\Gamma^2 = \text{const}$, one would have an approximately constant blastwave momentum, i.e.

$$p \propto nr^3\beta\Gamma \simeq \text{const}, \quad (8.10)$$

or $r^3\Gamma \simeq \text{const}$. This gives $E \propto \Gamma$, which is decreasing with distance/time. Noting

$$t \sim \frac{r}{2\Gamma^2 c} \propto r\Gamma^{-2} \propto \begin{cases} \Gamma^{-1/3} \cdot \Gamma^{-2} \propto \Gamma^{-7/3}, \\ r \cdot r^6 \propto r^7, \end{cases} \quad (8.11)$$

one gets

$$E \propto \Gamma \propto r^{-3} \propto t^{-3/7}, \quad r \propto t^{1/7}. \quad (8.12)$$

In reality, a radiative fireball can be achieved only if $\epsilon_e \sim 1$, and $v_c < v_m$ (fast cooling). Since afterglow modeling shows ϵ_e is typically $\ll 1$, one may not have a fully radiative

¹ The following scaling discussions apply to the regime $k < 3$. For $k \geq 3$, the self-similar solutions are more complicated, and require separate treatments (e.g. Waxman and Shvarts, 1993; Best and Sari, 2000; Sari, 2006).

fireball. More generally, one may consider a modified adiabatic fireball model with a radiative loss correction (see §8.1.3 for detailed discussion).

Energy Injection

It is possible that the blastwave energy continuously increases with time. This is relevant when the blastwave is fed by a long-lasting Poynting-flux-dominated wind (so that the reverse shock is weak or does not exist). Effectively, the energy from the central engine wind is continuously injected into the blastwave.

Let the central engine have a luminosity history

$$L(t) = L_0 \left(\frac{t}{t_0} \right)^{-q}. \quad (8.13)$$

Here t is the central engine time, which is the same as the time in the observer frame if the cosmological time dilation factor $(1+z)$ is ignored. The total energy in the blastwave (when reverse shock does not exist or is extremely weak) can then be expressed as

$$E_{\text{tot}} = E_0 + E_{\text{inj}}, \quad (8.14)$$

where E_0 is the initial energy in the blastwave, and

$$E_{\text{inj}} = \int_{t_0}^t L(t) dt = \begin{cases} \frac{L_0 t_0^q}{1-q} (t^{1-q} - t_0^{1-q}) \simeq \frac{L_0 t_0^q}{1-q} t^{1-q}, & \text{for } t \gg t_0, \quad q < 1, \\ L_0 t_0 \ln \left(\frac{t}{t_0} \right), & q = 1, \\ \frac{L_0 t_0^q}{q-1} (t_0^{1-q} - t^{1-q}) \simeq \frac{L_0 t_0}{q-1}, & \text{for } t \gg t_0, \quad q > 1, \end{cases} \quad (8.15)$$

is the energy injected into the blastwave from the long-lasting central engine. One can immediately see that E_{inj} does not depend on t (essentially a constant) when $q \geq 1$. Only when $q < 1$ can the total energy in the blastwave significantly increase with time.

For $q < 1$ the blastwave scaling remains the same as the constant E case early on, when $E_{\text{inj}} \ll E_0$. However, when E_{inj} exceeds E_0 , the blastwave dynamics scaling law is modified (Zhang and Mészáros, 2001a). In the regime of $E_{\text{inj}} \gg E_0$, the total energy in the blastwave,

$$E_{\text{tot}} \sim E_{\text{inj}} \propto t^{1-q}, \quad (8.16)$$

is no longer a constant, but increases with time. The blastwave dynamics are modified accordingly.

For the ISM (constant density) case, one has

$$\Gamma^2 r^3 \propto t^{1-q}. \quad (8.17)$$

Again taking $t \propto r \cdot \Gamma^{-2}$, one can derive

$$\Gamma^2 r^3 \propto r^{1-q} \Gamma^{2(q-1)}. \quad (8.18)$$

Regrouping the parameters, one finally gets

$$\Gamma \propto r^{-\frac{2+q}{4-2q}} \propto t^{-\frac{2+q}{8}}, \quad r \propto t^{\frac{2-q}{4}}. \quad (8.19)$$

For the wind case, one has

$$\Gamma^2 r \propto t^{1-q} \propto r^{1-q} \Gamma^{2q-2}. \quad (8.20)$$

The scaling laws can be derived as

$$\Gamma \propto r^{\frac{q}{2q-4}} \propto t^{-\frac{q}{4}}, \quad r \propto t^{\frac{2-q}{2}}. \quad (8.21)$$

Notice that all the above scaling laws are valid only when $q < 1$ is satisfied. All the scaling relations can be reduced to the constant energy case if one adopts $q = 1$ in the above relations. These relations are not physical for $q > 1$.

More generally, the scaling laws in a stratified medium with energy injection can be derived (Exercise 8.1).

8.1.2 Blandford–McKee Self-Similar Solution

Blandford and McKee (1976) discovered a self-similar solution of relativistic blastwaves. It describes the internal structure of the blastwave, i.e. density, Lorentz factor, and internal energy density as a function of a spatial coordinate, which can be cast into a simple function form.

By very generally assuming

$$\Gamma^2 \propto r^{-\mu} \quad (\mu > -1), \quad (8.22)$$

Blandford and McKee (1976) found that the spatial coordinate can be expressed as

$$\chi(r) = [1 + 2(\mu + 1)(\Gamma(\hat{t}))^2] \left(1 - \frac{r(\hat{t})}{R(\hat{t})} \right), \quad (8.23)$$

where $\Gamma(\hat{t})$ is the Lorentz factor of the shock itself at a lab-frame (not observer-frame) time \hat{t} , $R(\hat{t}) = c\beta\hat{t} \simeq c\hat{t}$ is the distance of the shock front from the engine, and $r(\hat{t})$ is the distance of a fluid element from the engine at the same lab-frame time.

Considering an impulsive blastwave entering a stratified medium with $\rho = Ar^{-k}$, one has $\mu = 3 - k$ and $k < 4$. The χ coordinate is now written as

$$\chi(r) = [1 + 2(4 - k)(\Gamma(\hat{t}))^2] \left(1 - \frac{r(\hat{t})}{R(\hat{t})} \right). \quad (8.24)$$

The Blandford–McKee solution reads (Blandford and McKee, 1976; Granot and Sari, 2002)

$$n(r, \hat{t}) = 2^{3/2} \Gamma(\hat{t}) n \chi^{-(10-3k)/(8-2k)}, \quad (8.25)$$

$$\gamma(r, \hat{t}) = 2^{-1/2} \Gamma(\hat{t}) \chi^{-1/2}, \quad (8.26)$$

$$p(r, \hat{t}) = \frac{2}{3} [\Gamma(\hat{t})]^2 n m_p c^2 \chi^{-(17-4k)/(12-3k)}. \quad (8.27)$$

In a blastwave, the coordinate χ of a fluid element is given by

$$\chi = \left(\frac{R(\hat{t})}{R(\hat{t}_0)} \right)^{4-k} = \left(\frac{\hat{t}}{\hat{t}_0} \right)^{4-k}, \quad (8.28)$$

where $R(\hat{t}_0)$ is the shock front radius as the fluid element crosses the shock at the lab-frame time \hat{t}_0 . One can see that the Blandford–McKee profile shows a concentration of matter in a thin shell near the shock front.

An afterglow modeler cares about how the shock front radius (R) and the Lorentz factor of the blastwave fluid just behind the shock front ($\Gamma_{\text{bw}} = \Gamma/\sqrt{2}$) evolves as a function of the observer time t . According to Eq. (69) of Blandford and McKee (1976), the total energy in a stratified ejecta ($\rho = AR^{-k}$) reads (Granot and Sari, 2002)

$$E = \frac{8\pi}{(17-4k)} AR^{-2} (c\hat{t})^3 [\Gamma(\hat{t})]^2, \quad (8.29)$$

which is written in terms of the lab-frame time \hat{t} and the shock front Lorentz factor $\Gamma(\hat{t})$. This gives

$$R(t) = \left(\frac{(17-4k)(4-k)Et}{4\pi Ac} \right)^{1/(4-k)}, \quad (8.30)$$

$$\Gamma_{\text{bw}}(t) = \left(\frac{(17-4k)E}{4^{5-k}(4-k)^{3-k}\pi Ac^{5-k}t^{3-k}} \right)^{\frac{1}{2(4-k)}}. \quad (8.31)$$

For $k = 0$ (a constant density medium), this reads

$$R(t) = \left(\frac{17Et}{\pi m_p n c} \right)^{1/4} \simeq (3.2 \times 10^{16} \text{ cm}) E_{52}^{1/4} n^{-1/4} t^{1/4}, \quad (8.32)$$

$$\Gamma_{\text{bw}}(t) = \frac{1}{4} \left(\frac{17E}{\pi n m_p c^5 t^3} \right)^{1/8} \simeq 260 E_{52}^{1/8} n^{-1/8} t^{-3/8}. \quad (8.33)$$

However, such expressions are not precise to describe the global evolution of the blastwave. This is because the observed emission comes from a layer of fluid behind the shock and also from a solid angle within the $1/\Gamma_{\text{bw}}$ cone. The above expressions only apply to the fluid immediately behind the shock along the line of sight.

For a more precise treatment, below we discuss the constant density case ($k = 0$) in detail. The Blandford–McKee solution for such a case reads

$$n(r, \hat{t}) = 2^{3/2} \Gamma(\hat{t}) n \chi^{-5/4}, \quad (8.34)$$

$$\gamma(r, \hat{t}) = 2^{-1/2} \Gamma(\hat{t}) \chi^{-1/2}, \quad (8.35)$$

$$p(r, \hat{t}) = \frac{2}{3} [\Gamma(\hat{t})]^2 n m_p c^2 \chi^{-17/12}. \quad (8.36)$$

According to Eq. (43) of Blandford and McKee (1976), the total energy in the blastwave can be written as

$$E = \frac{8\pi}{17} n m_p c^2 (c\hat{t})^3 [\Gamma(\hat{t})]^2. \quad (8.37)$$

In the differential form, the lab-frame time \hat{t} and the observer time t are related through $d\hat{t} = (1 - \beta)^{-1} dt \simeq 2\Gamma_{\text{bw}}^2 dt$, where the cosmological factor $(1 + z)$ is not included. In the integrated form, however, the coefficient 2 should be replaced by a different coefficient, which takes care of the history of blastwave deceleration as well as the contributions of

fluid elements from a range of angles within the $1/\Gamma_{\text{bw}}$ cone. Let us generally write it in the form of $\hat{t} = a\Gamma_{\text{bw}}^2 t$. Considering Eq. (8.37) and $R \simeq c\hat{t}$, one can derive (Exercise 8.2)

$$R(t) = \left(\frac{17aEt}{16\pi n m_p c} \right)^{1/4}, \quad (8.38)$$

$$\Gamma_{\text{bw}}(t) = \left(\frac{17E}{16\pi a^3 n m_p c^5 t^3} \right)^{1/8}. \quad (8.39)$$

For the constant energy, constant density ($k = 0$) case, Sari (1997) suggested that the coefficient should be $a = 16$. However, Waxman (1997a) showed that this would cause some inconsistency with data and argued that the coefficient should be close to 2. More detailed numerical calculations give the coefficient between 3 and 7, depending on the details of the hydrodynamic evolution. Sari et al. (1998) adopted $a = 4$ in their afterglow calculations.

If one takes $a = 16$, one derives Eqs. (8.32) and (8.33) above. However, if one takes a more reasonable value $a = 4$, the R - t and Γ_{bw} - t relations can be written as (Sari et al., 1998)

$$R(t) = \left(\frac{17Et}{4\pi n m_p c} \right)^{1/4} \simeq (2.3 \times 10^{16} \text{ cm}) E_{52}^{1/4} n^{-1/4} t^{1/4}, \quad (8.40)$$

$$\Gamma_{\text{bw}}(t) = \left(\frac{17E}{1024\pi n m_p c^5 t^3} \right)^{1/8} \simeq 436 E_{52}^{1/8} n^{-1/8} t^{-3/8}. \quad (8.41)$$

These expressions may be adopted to calculate the dynamical evolution and synchrotron radiation from the blastwave for the constant energy, constant density case.

8.1.3 Blastwave Dynamics: Differential Equations

Compared with the simple scaling relations in §8.1.1, the blastwave dynamics can be more precisely delineated with a set of differential equations. Below we discuss the simplest 1-D model that solves Γ as a function of r in a uniform, isotropic blastwave without considering the internal structure of the blastwave (Blandford–McKee profile) and the luminosity/Lorentz factor structure of the jet (which will be discussed later in §8.4.4). Such a model has been widely used by various authors to solve the afterglow problems (e.g. Chiang and Dermer, 1999; Moderski et al., 2000; Huang et al., 2000; Dermer and Humi, 2001; Uhm, 2011; Pe’er, 2012; Nava et al., 2013).

Constructing such a 1-D model is non-trivial. The ultimate goal is to write a differential equation $d\Gamma/dr$, i.e. the change of Γ when the blastwave advances a distance dr in the circumburst medium. Since the blastwave is decelerating, this quantity is negative.

Early Attempts

Let us consider a blastwave with an initial mass M_0 which at a certain radius (r) or observer time (t) has collected (and shock heated) a certain mass m from the medium. At any instant, in the *rest frame comoving with the blast*, one may define an effective “rest mass” of the

blastwave, which also includes the internal energy U of the shock-heated medium besides the masses from the jet (M_0) and from the medium (m), i.e.

$$M = M_0 + m + U/c^2. \quad (8.42)$$

As will soon be evident, this treatment is still incomplete, since the pressure should also be included.

In most early blastwave papers (e.g. Chiang and Dermer, 1999; Piran, 1999; Huang et al., 1999, 2000; Moderski et al., 2000; Dermer and Humi, 2001), a simple (but inaccurate) treatment was adopted by expressing the total blastwave energy in *the observer frame* as

$$E_{\text{bw}} = \Gamma M c^2. \quad (8.43)$$

With another ad hoc assumption (we will explain why it is ad hoc later)

$$U = (\Gamma - 1) m c^2, \quad (8.44)$$

one gets $M = M_0 + \Gamma m$. Neglecting radiative loss, energy conservation before and after the blastwave shocks an increment of mass dm is given by

$$d(E_{\text{bw}}) = c^2 dm, \quad (8.45)$$

since for each step an additional rest mass energy $d(mc^2)$ is added to the blastwave. Noting Eq. (8.43), one gets

$$M d\Gamma + \Gamma dM - dm = 0. \quad (8.46)$$

With Eq. (8.42) and

$$dM = dm + dU/c^2 = dm + (\Gamma - 1)dm = \Gamma dm, \quad (8.47)$$

one gets a simple (but inaccurate) equation

$$\frac{d\Gamma}{dm} = -\frac{\Gamma^2 - 1}{M}. \quad (8.48)$$

To complete the problem, one needs to quantify dm/dr , i.e. to make a connection between distance and the amount of ambient medium collected. This is straightforward for an isotropic blastwave. Considering an ambient density profile $\rho(r)$, one has

$$\frac{dm}{dr} = 4\pi r^2 \rho(r). \quad (8.49)$$

Two commonly discussed models are $\rho(r) = \text{const}$ (ISM) and $\rho(r) = Ar^{-2}$ (wind).

Observers care more about how Γ evolves with the observer's time t . For the 1-D problem, one can ignore the complications of equal-arrival-time surface (§3.4.2) and directly make a connection between dr and dt , i.e.

$$\frac{dr}{dt} = \frac{\beta c}{1 - \beta} = (\Gamma \sqrt{\Gamma^2 - 1} + \Gamma^2 - 1)c. \quad (8.50)$$

Combining Eq. (8.50) with Eqs. (8.46) and (8.49), one can solve Γ as a function of t .

It was soon realized that Eq. (8.48) fails to reproduce the dynamics in the non-relativistic regime (Huang et al., 1999, 2000). Several authors (Huang et al., 1999, 2000; Pe'er, 2012;

Nava et al., 2013) later made attempts to revise Eq. (8.48) to more correctly delineate the blastwave dynamics.

Huang et al. (1999, 2000) argued that the key correction should be to Eq. (8.47). Instead of introducing $dU = (\Gamma - 1)dm c^2$, they argued that one should adopt $dU = d[(\Gamma - 1)m]c^2 = (\Gamma - 1)dm c^2 + mc^2 d\Gamma$. Also, by introducing an energy loss parameter ϵ ($\epsilon = 0$ for adiabatic and $\epsilon = 1$ for radiative), they derived a modified differential equation

$$\frac{d\Gamma}{dm} = -\frac{\Gamma^2 - 1}{M_0 + \epsilon m + 2(1 - \epsilon)\Gamma m} \quad (8.51)$$

to replace Eq. (8.48). This formula appears to match both the Blandford–McKee solution in the ultra-relativistic regime and the Sedov solution in the non-relativistic regime.

Even though Eq. (8.51) approximately delineates the blastwave dynamics, there are three issues in the treatment.

First, the differential equation $dU = (\Gamma - 1)dm c^2$ comes directly from the relativistic shock jump condition, i.e. the internal energy gain is defined by the instantaneous Lorentz factor of the blastwave (§4.2.3), and therefore is justified. The treatment in Eq. (8.44), on the other hand, is imposed by hand even though it may be approximately valid. In principle, the internal energy U in the blastwave region is subject to increase due to heating at the shock front, and decrease due to adiabatic loss and radiative loss. Equation (8.44) has implicitly introduced the assumption that adiabatic and radiative losses of the blastwave keep the internal energy satisfying Eq. (8.44). As a result, this treatment is regarded as an ad hoc solution (Nava et al., 2013).

Second, related to the above point, the adiabatic loss of the blastwave is not properly treated in Eq. (8.51). This effect may not be significant for the usual ISM and wind models, but is needed to conserve energy and correctly describe the “adiabatic” acceleration effect for more complicated blastwave problems (e.g. Uhm et al., 2012; Uhm and Zhang, 2014a; Nava et al., 2013).

Finally, Eqs. (8.42) and (8.43) are inaccurate. In the *observer frame*, the rest-frame pressure also enters the energy–momentum tensor, as can be seen by comparing Eqs. (3.105) and (3.106). This problem was pointed out by Pe’er (2012),² who corrected this error but did not address the other two issues mentioned above. A correct treatment by addressing all three issues was presented by Nava et al. (2013), which we introduce below.

The Correct Treatment

According to Eq. (3.106), the energy density of the blastwave in the observer frame is

$$T^{00} = \Gamma^2(\rho_0 c^2 + e + p) - p = \Gamma^2 \rho_0 c^2 + (\hat{\gamma} \Gamma^2 - \hat{\gamma} + 1)e, \quad (8.52)$$

where ρ_0 is the comoving mass density, e is the comoving internal energy density, and $p = (\hat{\gamma} - 1)e$ is the comoving pressure.

In the observer frame, the total energy in the shocked medium region (Region II according to the convention introduced in §4.3) is

² It is also included in the treatment of Uhm (2011) and Uhm et al. (2012) within the framework of the mechanical model (Beloborodov and Uhm, 2006).

$$E_2 = T^{00}V = T^{00}\frac{V'}{\Gamma} = \Gamma mc^2 + \Gamma_{\text{eff}}U, \quad (8.53)$$

where

$$\Gamma_{\text{eff}} = \frac{\hat{\gamma}\Gamma^2 - \hat{\gamma} + 1}{\Gamma} \simeq \hat{\gamma}\Gamma \quad (8.54)$$

(the approximation is made for $\Gamma \gg 1$), $U = eV'$ is the internal energy in the comoving frame, and $\rho_0 V' = m$ has been adopted. Notice that for $\Gamma \gg 1$ one has $\Gamma_{\text{eff}} \simeq \hat{\gamma}\Gamma \simeq (4/3)\Gamma > \Gamma$. The widely adopted Eq. (8.43) therefore underestimates the total energy in the blastwave.

Since in the self-similar deceleration phase the ejecta is “cold” (no internal energy), it is straightforward to write the energy in the ejecta, i.e.

$$E_3 = \Gamma M_0 c^2. \quad (8.55)$$

The total energy in the blastwave is therefore (Nava et al., 2013)

$$E_{\text{bw}} = E_2 + E_3 = \Gamma(M_0 + m)c^2 + \Gamma_{\text{eff}}U. \quad (8.56)$$

This equation should replace Eq. (8.43).

Considering the energy conservation equation (8.45) and also introducing a radiative loss term ($dU_{\text{rad}} < 0$) in the equation, one gets

$$d[\Gamma(M_0 + m)c^2 + \Gamma_{\text{eff}}U] = c^2 dm + \Gamma_{\text{eff}}dU_{\text{rad}}. \quad (8.57)$$

The change of internal energy includes three terms, i.e.

$$dU = dU_{\text{sh}} + dU_{\text{ad}} + dU_{\text{rad}}, \quad (8.58)$$

where

$$dU_{\text{sh}} = (\Gamma - 1)d(mc^2) \quad (8.59)$$

is the internal energy increase due to shock heating, and dU_{ad} is the adiabatic loss term. Plugging in Eq. (8.57), one finds that the radiative term dU_{rad} cancels out in the problem. The final dynamical differential equation reads (Nava et al., 2013)

$$\frac{d\Gamma}{dr} = -\frac{(\Gamma_{\text{eff}} + 1)(\Gamma - 1)c^2 \frac{dm}{dr} + \Gamma_{\text{eff}} \frac{dU_{\text{ad}}}{dr}}{(M_0 + m)c^2 + U \frac{d\Gamma_{\text{eff}}}{d\Gamma}}. \quad (8.60)$$

If one neglects adiabatic loss ($dU_{\text{ad}}/dr = 0$) and adopts $U = (\Gamma - 1)mc^2$ and $dU_{\text{sh}} = d[(\Gamma - 1)mc^2]$, the above treatment can be written as

$$\frac{d\Gamma}{dm} = -\frac{\hat{\gamma}(\Gamma^2 - 1) - (\hat{\gamma} - 1)\Gamma\beta^2}{M_0 + m[2\hat{\gamma}\Gamma - (\hat{\gamma} - 1)(1 + \Gamma^{-2})]}, \quad (8.61)$$

which is Eq. (6) of Pe’er (2012). This equation can be reduced to the solution of Huang et al. (1999) by taking $\hat{\gamma} = 1$ (i.e. neglecting the pressure term).

In any case, Eq. (8.60) is the correct differential equation. Together with Eqs. (8.49) and (8.50), one can solve for Γ as a function of r and the observer time t , if U and dU_{ad}/dr are specified. This is discussed next.

Adiabatic Cooling and Internal Energy Evolution

In order to solve Eq. (8.60), one needs to know U and dU_{ad}/dr .

Consider the first law of thermodynamics, $dU = TdS - pdV'$, in the comoving frame (the internal energy U , temperature T , and pressure p can be defined only in the comoving frame, so no prime sign added). For an adiabatic process, one has $TdS = 0$, so that

$$dU_{\text{ad}} = -pdV' = -(\hat{\gamma} - 1)\frac{U}{V'}dV' = -(\hat{\gamma} - 1)Ud(\ln V'). \quad (8.62)$$

Noticing that the comoving shell width is roughly $\Delta' \sim r/\Gamma$ in the deceleration phase (Table 7.1), the comoving volume is $V' = 4\pi\xi r^3/\Gamma$ (where ξ is a constant of order unity). One then has $d(\ln V') = 3d(\ln r) - d(\ln \Gamma)$. Equation (8.62) then becomes

$$dU_{\text{ad}} = -(\hat{\gamma} - 1)\left(\frac{3}{r}dr - \frac{1}{\Gamma}d\Gamma\right)U, \quad (8.63)$$

or

$$\frac{dU_{\text{ad}}}{dr} = -(\hat{\gamma} - 1)\left(\frac{3}{r} - \frac{1}{\Gamma}\frac{d\Gamma}{dr}\right)U. \quad (8.64)$$

Equation (8.64) also has a dependence on $d\Gamma/dr$, so it can be inserted into Eq. (8.60) to solve for $d\Gamma/dr$. Noticing the definition of Γ_{eff} (Eq. (8.54)) and

$$\frac{d\Gamma_{\text{eff}}}{d\Gamma} = \frac{\hat{\gamma}\Gamma^2 + \hat{\gamma} - 1}{\Gamma^2}, \quad (8.65)$$

after some manipulations, one finally derives

$$\frac{d\Gamma}{dr} = -\frac{4\pi r^2 \rho(r) \Gamma(\Gamma^2 - 1)(\hat{\gamma}\Gamma - \hat{\gamma} + 1) - (\hat{\gamma} - 1)\Gamma(\hat{\gamma}\Gamma^2 - \hat{\gamma} + 1)(3U/r)}{\Gamma^2(M_0 + m)c^2 + (\hat{\gamma}^2\Gamma^2 - \hat{\gamma}^2 + 3\hat{\gamma} - 2)U}, \quad (8.66)$$

which can be solved if $U(r)$ is solved.

The evolution of internal energy U in the blastwave region can be solved from Eq. (8.58). Let us define a radiative efficiency

$$\epsilon = \epsilon_{\text{rad}}\epsilon_e, \quad (8.67)$$

where ϵ_e is the fraction of the newly shock-heated blastwave energy that goes to electrons (which is the maximum fraction that can be radiated), and ϵ_{rad} is the fraction of the electron energy that is radiated ($\epsilon_{\text{rad}} \simeq 1$ for fast cooling, and $\epsilon_{\text{rad}} < 1$ for slow cooling). One then has

$$dU_{\text{rad}} = -\epsilon(dU_{\text{sh}}) = -\epsilon(\Gamma - 1)dm c^2, \quad (8.68)$$

where Eq. (8.59) has been used. Inserting Eqs. (8.59), (8.63), and (8.68) into Eq. (8.58), one finally gets the differential equation

$$\frac{dU}{dr} = (1 - \epsilon)(\Gamma - 1)c^2 \cdot 4\pi r^2 \rho(r) - (\hat{\gamma} - 1)\left(\frac{3}{r} - \frac{1}{\Gamma}\frac{d\Gamma}{dr}\right)U. \quad (8.69)$$

Together with (8.66) and an appropriate initial condition, $U(r)$ can be solved. In general, it is different from $U = (\Gamma - 1)mc^2$, the condition imposed by previous authors (e.g. Chiang and Dermer, 1999; Piran, 1999; Huang et al., 1999, 2000).

More on Adiabatic Cooling and Internal Energy Evolution

The second term in the numerator of Eq. (8.66) originates from adiabatic cooling. Noticing that U roughly scales with Γ and that $\rho \propto r^{-k}$ in general, one has the first and second terms in the numerator scale as $\Gamma^4 r^{2-k}$ and $\Gamma^4 r^{-1}$, respectively. The adiabatic term becomes important when $2 - k \leq -1$, or (see also Nava et al. 2013)

$$k \geq 3. \quad (8.70)$$

In the standard afterglow models, one has $k = 0$ (ISM) or $k = 2$ (wind), so that the adiabatic term is not important. This is why most previous afterglow models that do not include the adiabatic cooling effect still give roughly correct solutions to blastwave dynamics. However, in a more stratified medium (e.g. the blastwave enters a void), the adiabatic term is essential for reproducing the correct blastwave dynamics, in particular, the so-called “adiabatic acceleration” dynamics of the blastwave due to the pdV work (Uhm and Zhang, 2014a; Nava et al., 2013).

The internal energy U can be analyzed on the microscopic scale, which reads

$$U(r) = 4\pi c^2 \int_0^r \hat{r}^2 d\hat{r} \left\{ \rho_p(\hat{r}) [\bar{\gamma}_p(\hat{r}, r) - 1] + \rho_e(\hat{r}) [\bar{\gamma}_e(\hat{r}, r) - 1] \right\}. \quad (8.71)$$

Here protons (denoted by subscript p) and electrons (denoted by subscript e) are treated separately due to their different cooling histories (electrons are subject to both radiative and adiabatic cooling while protons are only subject to the latter), and their possible different number densities (in the case of a pair-loaded medium). Since cooling depends on history, for each blastwave radius r , one cares about all the previous radii (denoted by \hat{r}) where protons/electrons were accelerated. The blastwave is treated as many thin layers with each layer shocked at a different radius \hat{r} . The Lorentz factor $\bar{\gamma}_p(\hat{r}, r)$ ($\bar{\gamma}_e(\hat{r}, r)$) denotes the mean random Lorentz factor of protons (electrons) at the blastwave radius r for the layer shocked at the radius \hat{r} .

For individual particles (electrons or protons), one can solve for their Lorentz factor evolution as a function of comoving time t' by taking into account radiative and adiabatic cooling. Again noticing $d(\ln V') = -d(\ln n_{e,p}) = -\hat{\gamma}^{-1} d(\ln p)$ ($n_{e,p}$ is the electron/proton number density, and p is the pressure), one has (Uhm et al., 2012)

$$\begin{aligned} \frac{d\gamma_{e,p}}{dt'} = \dot{\gamma}_{e,p} &= -\frac{\sigma_{T,e/p} B'^2 (1+Y)}{6\pi m_{e,p} c} \gamma_{e,p}^2 + \frac{\hat{\gamma} - 1}{\hat{\gamma}} \frac{\dot{p}}{p} \gamma_{e,p} \\ &= -\frac{\sigma_{T,e/p} B'^2 (1+Y)}{6\pi m_{e,p} c} \gamma_{e,p}^2 - (\hat{\gamma} - 1) \frac{\dot{n}_{e,p}}{n_{e,p}} \gamma_{e,p}. \end{aligned} \quad (8.72)$$

Here the first term on the right hand side of the equation denotes the radiative cooling through synchrotron and synchrotron self-Compton, B' is the comoving magnetic field, Y is the SSC cooling parameter (see §5.2.3 for details), $\dot{p} = dp/dt'$, $\dot{n}_{e,p} = dn_{e,p}/dt$, and $\sigma_{T,e/p}$ are the electron/proton Thomson cross sections, respectively.

Numerically, it is more convenient to solve the evolution of $1/\gamma_{e,p}$ rather than $\gamma_{e,p}$. Dividing Eq. (8.72) by $\gamma_{e,p}^2$, one can write (Uhm et al., 2012; Uhm and Zhang, 2014b)

$$\begin{aligned}
\frac{d}{dt'} \left(\frac{1}{\gamma_{e,p}} \right) &= \frac{\sigma_{T,e/p} B'^2 (1+Y)}{6\pi m_{e,p} c} - \frac{\hat{\gamma} - 1}{\hat{\gamma}} \frac{\dot{p}}{p} \left(\frac{1}{\gamma_{e,p}} \right) \\
&= \frac{\sigma_{T,e/p} B'^2 (1+Y)}{6\pi m_{e,p} c} + (\hat{\gamma} - 1) \frac{\dot{n}_{e,p}}{n_{e,p}} \left(\frac{1}{\gamma_{e,p}} \right). \quad (8.73)
\end{aligned}$$

Notice that for a relativistic gas with $\hat{\gamma} = 4/3$, one has $(\hat{\gamma} - 1) = 1/3$ and $(\hat{\gamma} - 1)/\hat{\gamma} = 1/4$.

In principle, by solving the evolution of $\gamma_e(\hat{r}, r)$ and $\gamma_p(\hat{r}, r)$ of all electrons and protons accelerated at different radii \hat{r} , one can eventually solve $\tilde{\gamma}_e(\hat{r}, r)$ and $\tilde{\gamma}_p(\hat{r}, r)$ in Eq. (8.71). This would give a more accurate treatment of the internal energy U than using Eq. (8.69), where a constant radiative efficiency ϵ has been introduced.

Adiabatic cooling is also important in solving electron cooling and the synchrotron spectrum during the prompt emission phase. For example, by including adiabatic cooling in the treatment of fast cooling in a variable magnetic field (§5.1.5), the asymptotic electron energy spectral index becomes $-(6b - 4)/(6b - 1)$ rather than $-(2b - 2)/(2b - 1)$ (Uhm and Zhang, 2014b) (Exercise 8.3).

8.2 Synchrotron Spectrum Prescription

With the dynamics described in the previous section, one can calculate the time-dependent spectra of the blastwave emission and the lightcurves for different observational frequencies. The main radiation mechanism for afterglow emission is synchrotron radiation. As discussed in §5.1.8, the instantaneous synchrotron spectrum of an astrophysical system is a broken power law characterized by three break frequencies ν_m , ν_c , ν_a , and a maximum frequency ν_M . In order to delineate afterglow emission, one needs to establish a connection between these frequencies with shock dynamics.

For an electron with comoving Lorentz factor γ in the shocked region, the observed synchrotron frequency is

$$\nu \simeq \frac{3}{4\pi} \Gamma \gamma^2 \frac{eB'}{m_e c}, \quad (8.74)$$

where Γ is the bulk Lorentz factor,³ and B' is the comoving magnetic field strength. All these parameters can be derived from shock dynamics.

8.2.1 Minimum Injection Lorentz Factor γ_m

In the comoving frame of the shock, the injected electrons are assumed to have a power-law energy distribution form

$$N(\gamma) = N(\gamma_m) \left(\frac{\gamma}{\gamma_m} \right)^{-p}, \quad \text{for } \gamma_m < \gamma < \gamma_M. \quad (8.75)$$

³ In principle, Γ should be replaced by the Doppler factor \mathcal{D} , which is angle dependent. Here we have taken $\mathcal{D} = \Gamma$, which corresponds to a lab-frame observer angle $1/\Gamma$. This value can be regarded as a rough mean value of a spherical outflow.

The average Lorentz factor of the electrons can be calculated as

$$\bar{\gamma} = \frac{\int_{\gamma_m}^{\gamma_M} \gamma N(\gamma) d\gamma}{\int_{\gamma_m}^{\gamma_M} N(\gamma) d\gamma}. \quad (8.76)$$

For $p \neq 2$ and $p \neq 1$, one has

$$\bar{\gamma} = \frac{\frac{\gamma_M^{2-p}}{2-p} - \frac{\gamma_m^{2-p}}{2-p}}{\frac{\gamma_M^{1-p}}{1-p} - \frac{\gamma_m^{1-p}}{1-p}} \simeq \begin{cases} \frac{1-p}{2-p} \cdot \gamma_M, & p < 1, \\ \frac{p-1}{2-p} \left(\frac{\gamma_M}{\gamma_m} \right)^{2-p} \cdot \gamma_m, & 1 < p < 2, \\ \frac{p-1}{p-2} \cdot \gamma_m, & p > 2. \end{cases} \quad (8.77)$$

For $p = 1$, one has

$$\bar{\gamma} = \frac{\gamma_M - \gamma_m}{\ln \gamma_M - \ln \gamma_m} \simeq \gamma_M \cdot \left[\ln \left(\frac{\gamma_M}{\gamma_m} \right) \right]^{-1}, \quad (8.78)$$

and for $p = 2$, one has

$$\bar{\gamma} = \frac{\ln \gamma_M - \ln \gamma_m}{-\gamma_M^{-1} + \gamma_m^{-1}} \simeq \gamma_m \cdot \ln \left(\frac{\gamma_M}{\gamma_m} \right). \quad (8.79)$$

Shock theories usually predict $p \geq 2$ (§4.4). In this regime, $\bar{\gamma}$ mainly depends on γ_m . One can generally write

$$\gamma_m = g(p) \bar{\gamma}, \quad (8.80)$$

where

$$g(p) \simeq \begin{cases} \frac{p-2}{p-1}, & p > 2, \\ \ln^{-1}(\gamma_M/\gamma_m), & p = 2. \end{cases} \quad (8.81)$$

Defining ϵ_e as the fraction of internal energy that is given to electrons (§4.6), one can write

$$\epsilon_e(\Gamma - 1)n_p m_p c^2 = \bar{\gamma} n_e m_e c^2. \quad (8.82)$$

So

$$\bar{\gamma} = \epsilon_e(\Gamma - 1) \frac{m_p}{m_e} \frac{n_p}{n_e}, \quad (8.83)$$

and

$$\gamma_m = g(p) \epsilon_e(\Gamma - 1) \frac{m_p}{m_e} \frac{n_p}{n_e}. \quad (8.84)$$

If the shocked gas is hydrogen and not pair rich (which is usually the case), one has $n_p/n_e = 1$. Notice that n_e is the number density of the *non-thermal* electrons. If the shock somehow only accelerates a fraction ξ_e of electrons to radiate, and noticing that n_p stands for *all* the protons in the shock, for a pair-less hydrogen shock, one has

$$\gamma_m = g(p) \frac{\epsilon_e}{\xi_e} (\Gamma - 1) \frac{m_p}{m_e}. \quad (8.85)$$

Afterglow observations are generally consistent with $\xi_e = 1$, i.e. all the shocked electrons are accelerated.

For $1 < p < 2$, the minimum electron Lorentz factor depends on the maximum Lorentz factor as well, which reads (Dai and Cheng 2001, see §8.2)

$$\gamma_m \simeq \left(\frac{2-p}{p-1} \frac{m_p}{m_e} \epsilon_e \gamma \gamma_M^{p-2} \right)^{1/(p-1)}. \quad (8.86)$$

Some authors still use Eq. (8.84) to treat the $p < 2$ case (e.g. Panaitescu and Kumar, 2002).

8.2.2 Cooling Lorentz Factor γ_c

The cooling Lorentz factor, γ_c , can be defined at a comoving dynamical time scale t' . This is the epoch when electrons with this Lorentz factor lose energy significantly, i.e.

$$t' = \frac{\gamma_c m_e c^2}{\frac{4}{3} \gamma_c^2 \sigma_T c \frac{B'^2}{8\pi} (1 + \tilde{Y})} = \frac{6\pi m_e c}{\gamma_c \sigma_T B'^2 (1 + \tilde{Y})}, \quad (8.87)$$

where the parameter \tilde{Y} denotes all the IC correction terms. So the cooling Lorentz factor reads

$$\gamma_c = \frac{6\pi m_e c}{\sigma_T t' B'^2 (1 + \tilde{Y})}. \quad (8.88)$$

Connecting the comoving time t' with the observer time t (again a typical angle $1/\Gamma$ assumed),

$$t = \frac{t'}{D} \simeq \frac{t'}{\Gamma}, \quad (8.89)$$

one gets

$$\gamma_c = \frac{6\pi m_e c}{\sigma_T \Gamma t B'^2 (1 + \tilde{Y})}. \quad (8.90)$$

8.2.3 Self-Absorption Frequency ν_a

Using the blackbody method introduced in §5.1.6, one can derive the self-absorption frequency using

$$I_v^{\text{syn}}(\nu_a) = I_v^{\text{bb}}(\nu_a) \simeq 2kT \cdot \frac{\nu_a^2}{c^2}, \quad (8.91)$$

where

$$kT = \max(\gamma_m, \gamma_a) m_e c^2, \quad (8.92)$$

and γ_a is the corresponding Lorentz factor for ν_a .

8.2.4 Maximum Electron Lorentz Factor γ_M and Maximum Synchrotron Frequency ν_M

The maximum particle energy from the Fermi acceleration process can be estimated by balancing acceleration (heating) and cooling within the dynamical time scale. The condition can be written as

$$t'_{\text{acc}} \simeq \min(t'_{\text{dyn}}, t'_c). \quad (8.93)$$

For electrons, the comoving acceleration time scale can be written as

$$t'_{\text{acc}} \simeq \zeta \frac{r_B}{c} \simeq \zeta \frac{\gamma m_e c}{e B'}, \quad (8.94)$$

where

$$r_B = \frac{\gamma m_e c^2}{e B'} \quad (8.95)$$

is the gyration radius, and ζ is a parameter of order unity that describes the details of acceleration.

The comoving dynamical time scale is

$$t'_{\text{dyn}} \simeq \Gamma t \simeq \frac{R}{c \Gamma}. \quad (8.96)$$

The comoving cooling time scale is

$$t'_c = \frac{6\pi m_e c}{\gamma \sigma_T B'^2 (1 + \tilde{Y})}. \quad (8.97)$$

For electrons, one has $t'_c \ll t'_{\text{dyn}}$, so equating t'_{acc} (8.94) and t'_c (8.97), one gets

$$\gamma_M = \left[\frac{6\pi e}{\sigma_T B' \zeta (1 + \tilde{Y})} \right]^{1/2} \propto B'^{-1/2}. \quad (8.98)$$

It is interesting to note that the comoving synchrotron frequency

$$\nu'_M \sim \frac{3}{4\pi} \gamma_M^2 \frac{e B'}{m c} \simeq \frac{9e^2}{2\sigma_T \zeta m_e c (1 + \tilde{Y})} \simeq (5.7 \times 10^{22} \text{ Hz}) [\zeta (1 + \tilde{Y})]^{-1} \quad (8.99)$$

does not depend on B' , and depends on fundamental constants only. In the observer frame, the maximum synchrotron energy is boosted by a factor of Γ , i.e.

$$E_{\text{syn}, M} = \Gamma h \nu'_M \simeq 236 \text{ MeV } \Gamma [\zeta (1 + \tilde{Y})]^{-1}. \quad (8.100)$$

The emission of a 95 GeV photon was detected in the nearby GRB 130427A (Ackermann et al., 2014). Correcting for redshift ($z = 0.34$), this photon already exceeds the maximum synchrotron energy for a reasonable Γ at the time of observation (see detailed discussion in Ackermann et al. (2014)). It may demand an SSC origin (Fan et al., 2013b; Liu et al., 2013) or a novel particle acceleration mechanism for GRBs (Ackermann et al., 2014).

8.2.5 Comoving Magnetic Field Strength B'

In order to calculate synchrotron frequencies, the comoving magnetic field strength is needed. Assuming a fraction ϵ_B of the internal energy goes to magnetic fields (§4.6), one can estimate the comoving magnetic energy density as⁴

$$\frac{B'^2}{8\pi} = \epsilon_B (\Gamma - 1) n_2 m_p c^2 \simeq \epsilon_B (\Gamma - 1) (4\Gamma) n_1 m_p c^2 \simeq \epsilon_B 4\Gamma^2 n_1 m_p c^2. \quad (8.101)$$

⁴ In many papers, the relation $n_2 = (4\Gamma + 3)n_1$ has been adopted. This is because $\hat{\gamma} = 4/3$ has been adopted. Taking a more general expression $\hat{\gamma} = (4\Gamma + 1)/(3\Gamma)$, which applies to both relativistic and non-relativistic phases (§4.1.3), one has $n_2 = 4\Gamma n_1$.

So one has

$$B' = (32\pi m_p \epsilon_B n)^{1/2} \Gamma c, \quad (8.102)$$

where $n = n_1$ is the upstream (unshocked) medium density.

8.3 The Forward Shock Model

With the above preparations, one can calculate GRB afterglow lightcurves. We start with the standard forward shock afterglow model for an isotropic, relativistic blastwave during the self-similar deceleration regime (no reverse shock).

8.3.1 Constant Energy, Constant Density (ISM) Model

The simplest case is the constant energy ISM model, which describes the deceleration of an adiabatic fireball without energy injection by a constant density medium.

The shape of lightcurves can be derived simply through a scaling law analysis. For the constant energy ISM model in the relativistic regime, one has $\Gamma \propto t^{-3/8} \propto r^{-3/2}$, $\gamma_m \propto \Gamma$, $B' \propto \Gamma$, and $\gamma_c \propto \Gamma^{-1} t^{-1} B'^{-2} \propto \Gamma^{-3} t^{-1}$, so that

$$\nu_m \propto \Gamma \gamma_m^2 B' \propto \Gamma^4 \propto t^{-3/2}, \quad (8.103)$$

$$\nu_c \propto \Gamma \gamma_c^2 B' \propto \Gamma^{-1} t^{-2} B'^{-3} \propto t^{-1/2}, \quad (8.104)$$

$$F_{\nu, \max} \propto N_{\text{tot}} P_{\nu, \max} \propto r^3 B \Gamma \propto r^3 \Gamma^2 \propto t^0 \sim \text{const.} \quad (8.105)$$

The afterglow flux is a function of frequency and time. We adopt the convention⁵

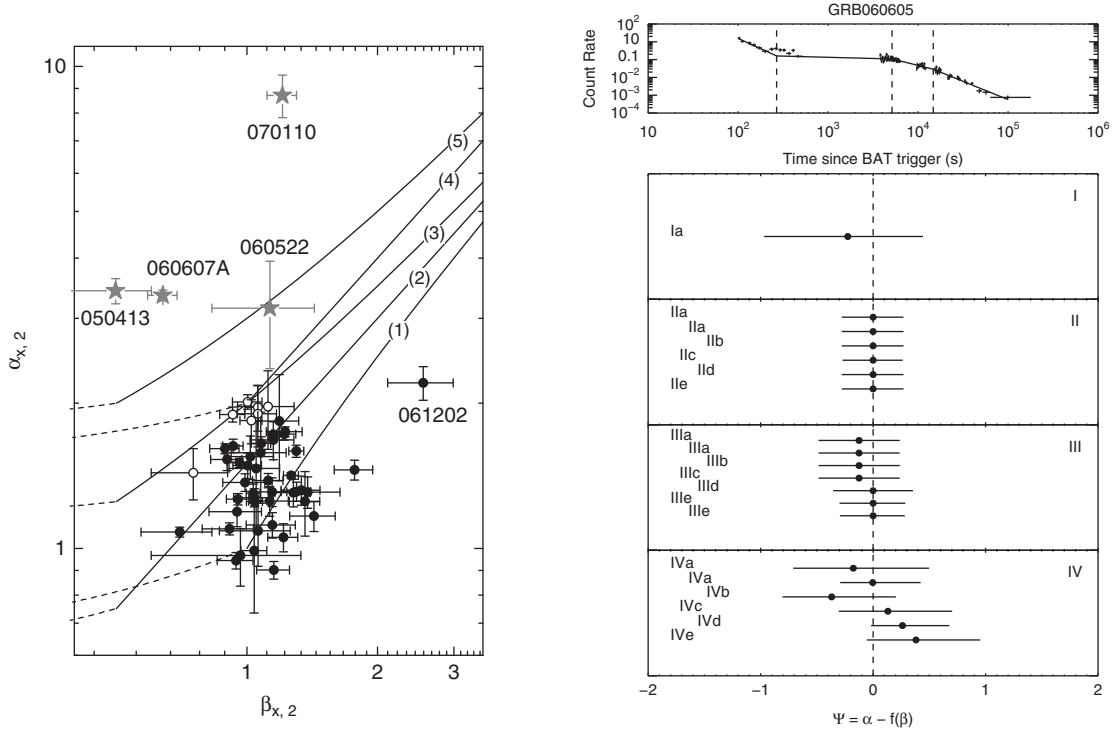
$$F_\nu \propto \nu^{-\beta} t^{-\alpha}. \quad (8.106)$$

It is interesting to investigate the α - β relations in different spectral regimes. These are called the *closure relations*, which can be used to quickly judge the effectiveness of each afterglow model. An example of confronting closure relations with observed data is presented in Fig. 8.1.

The closure relations can be derived directly by combining the above scaling relations of characteristic frequencies and $F_{\nu, \max}$ and the standard broken power-law synchrotron spectrum as discussed in §5.1.8. Below, we derive these relations for the constant energy, constant density deceleration model as an example.

- Slow cooling, $\nu < \nu_a$: $F_\nu = F_{\nu, \max} (\nu_a / \nu_m)^{1/3} (\nu / \nu_a)^2 \propto \text{const} \cdot \nu^2 \nu_a^{-5/3} \nu_m^{-1/3} \propto \nu^2 \cdot t^{(-3/2)(-1/3)} \propto \nu^2 t^{1/2}$. So $\alpha = -1/2$, $\beta = -2$.
- Slow cooling, $\nu_a < \nu < \nu_m$: $F_\nu = F_{\nu, \max} (\nu / \nu_m)^{1/3} \propto \text{const} \cdot \nu^{1/3} \nu_m^{-1/3} \propto \nu^{1/3} \cdot t^{(-3/2)(-1/3)} \propto \nu^{1/3} t^{1/2}$. So $\alpha = -1/2$, $\beta = -1/3$, and $\alpha = (3/2)\beta$.

⁵ Another convention is $F_\nu \propto \nu^\beta t^\alpha$. The closure relations for this notation can be modified from those derived from the convention (8.106) by switching the sign of α and β values.

**Figure 8.1**

Two examples of confronting X-ray afterglow α and β data (as collected by the *Swift* satellite) with various closure relations. *Left*: The predicted α - β relations in X-rays (lines) compared with the data. Four GRBs do not satisfy these conditions (internal plateaus) and therefore are likely of an internal origin. From Liang et al. (2007b). *Right*: Data compared with the closure-relation-predicted Ψ values. From Racusin et al. (2009).

- Slow cooling, $\nu_m < \nu < \nu_c$: $F_\nu = F_{\nu,\max}(\nu/\nu_m)^{-(p-1)/2} \propto \text{const} \cdot \nu^{-(p-1)/2} \nu_m^{(p-1)/2} \propto \nu^{-(p-1)/2} \cdot t^{(-3/2)((p-1)/2)} \propto \nu^{-(p-1)/2} t^{-3(p-1)/4}$. So $\alpha = 3(p-1)/4$, $\beta = (p-1)/2$. The closure relation $\alpha = (3/2)\beta$ still applies.
- Slow cooling, $\nu > \nu_c$: $F_\nu = F_{\nu,\max}(\nu_c/\nu_m)^{-(p-1)/2}(\nu/\nu_c)^{-p/2} = F_{\nu,\max} \nu_m^{(p-1)/2} \nu_c^{1/2} \nu^{-p/2} \propto \text{const} \cdot \nu^{-p/2} t^{(-3/2)((p-1)/2)} t^{(-1/2)(1/2)} \propto \nu^{-p/2} t^{(-3p+2)/4}$. So $\alpha = (3p-2)/4$, $\beta = p/2$. The closure relation is $\alpha = (3\beta - 1)/2$.
- Fast cooling, $\nu < \nu_a$: $F_\nu = F_{\nu,\max}(\nu_a/\nu_c)^{1/3}(\nu/\nu_a)^2 \propto \text{const} \cdot \nu^2 \nu_a^{-5/3} \nu_c^{-1/3} \propto \nu^2 \cdot t^{(-1/2)(-5/3)} t^{(-1/2)(-1/3)} \propto \nu^2 t$. So $\alpha = -1$, $\beta = -2$.
- Fast cooling, $\nu_a < \nu < \nu_c$: Following the same procedure, one gets $F_\nu \propto \nu^{1/3} t^{1/6}$, and $\alpha = \beta/2$.
- Fast cooling, $\nu_c < \nu < \nu_m$: $F_\nu \propto \nu^{-1/2} t^{-1/4}$, and $\alpha = \beta/2$.
- Fast cooling, $\nu > \nu_m$: Similar to the slow cooling $\nu > \nu_c$ case, $F_\nu \propto \nu^{-p/2} t^{(-3p+2)/4}$, and $\alpha = (3\beta - 1)/2$.

These closure relations are summarized in Table 8.1 (see also Zhang and Mészáros, 2004; Zhang et al., 2006). The cases of $\nu_m < \nu_a < \nu_c$ are presented in Table 8.2 (Gao et al.,

Table 8.1 The temporal decay index α and spectral index β in relativistic, isotropic, self-similar deceleration phase for $v_a < \min(v_m, v_c)$ and $p > 2$. From Zhang et al. (2006)

		No injection		Injection	
	β	α	$\alpha(\beta)$	α	$\alpha(\beta)$
ISM slow cooling					
$v < v_a$	-2	$-\frac{1}{2}$	$\alpha = \frac{\beta}{4}$	$\frac{q}{2} - 1$	—
$v_a < v < v_m$	$-\frac{1}{3}$	$-\frac{1}{2}$	$\alpha = \frac{3\beta}{2}$	$\frac{5q-8}{6}$	—
$v_m < v < v_c$	$\frac{p-1}{2}$	$\frac{3(p-1)}{4}$	$\alpha = \frac{3\beta}{2}$	$\frac{(2p-6)+(p+3)q}{4}$	$\alpha = (q-1) + \frac{(2+q)\beta}{2}$
$v > v_c$	$\frac{p}{2}$	$\frac{3p-2}{4}$	$\alpha = \frac{3\beta-1}{2}$	$\frac{(2p-4)+(p+2)q}{4}$	$\alpha = \frac{q-2}{2} + \frac{(2+q)\beta}{2}$
ISM fast cooling					
$v < v_a$	-2	-1	$\alpha = \frac{\beta}{2}$	-1	$\alpha = \frac{\beta}{2}$
$v_a < v < v_c$	$-\frac{1}{3}$	$-\frac{1}{6}$	$\alpha = \frac{\beta}{2}$	$\frac{7q-8}{6}$	—
$v_c < v < v_m$	$\frac{1}{2}$	$\frac{1}{4}$	$\alpha = \frac{\beta}{2}$	$\frac{3q-2}{4}$	—
$v > v_m$	$\frac{p}{2}$	$\frac{3p-2}{4}$	$\alpha = \frac{3\beta-1}{2}$	$\frac{(2p-4)+(p+2)q}{4}$	$\alpha = \frac{q-2}{2} + \frac{(2+q)\beta}{2}$
Wind slow cooling					
$v < v_a$	-2	-1	$\alpha = \frac{\beta}{2}$	$q - 2$	—
$v_a < v < v_m$	$-\frac{1}{3}$	0	0	—	—
$v_m < v < v_c$	$\frac{p-1}{2}$	$\frac{3p-1}{4}$	$\alpha = \frac{3\beta+1}{2}$	$\frac{(2p-2)+(p+1)q}{4}$	$\alpha = \frac{q}{2} + \frac{(2+q)\beta}{2}$
$v > v_c$	$\frac{p}{2}$	$\frac{3p-2}{4}$	$\alpha = \frac{3\beta-1}{2}$	$\frac{(2p-4)+(p+2)q}{4}$	$\alpha = \frac{q-2}{2} + \frac{(2+q)\beta}{2}$
Wind fast cooling					
$v < v_a$	-2	-2	$\alpha = \beta$	$q - 3$	—
$v_a < v < v_c$	$-\frac{1}{3}$	$\frac{2}{3}$	$\alpha = -2\beta$	$\frac{(1+q)}{3}$	—
$v_c < v < v_m$	$\frac{1}{2}$	$\frac{1}{4}$	$\alpha = \frac{\beta}{2}$	$\frac{3q-2}{4}$	—
$v > v_m$	$\frac{p}{2}$	$\frac{3p-2}{4}$	$\alpha = \frac{3\beta-1}{2}$	$\frac{(2p-4)+(p+2)q}{4}$	$\alpha = \frac{q-2}{2} + \frac{(2+q)\beta}{2}$

2013a). A full collection of all possible closure relations in the external shock models can be found in the review article of Gao et al. (2013a).

Calculating the detailed time-dependent spectra and frequency-dependent lightcurves requires precise numerical coefficients contained in the characteristic model parameters (v_m , v_c , v_a , $F_{v,\max}$). These numerical coefficients depend on the following ingredients (e.g. Granot and Sari, 2002; Uhm and Zhang, 2014c): (1) Whether or not the Blandford–McKee (BM) solution is considered. In general, the BM solution gives a smaller Lorentz factor than the analytical estimate; (2) Whether or not the equal-arrival-time surface is considered. This effect compensates the effect of the BM profile; (3) Whether or not the detailed electron cooling history (in a decreasing B field, as is the case for a decelerating blast-wave) is considered. Numerical calculations are needed to get precise coefficients. For the constant energy ISM model, numerical results give the following expressions (Granot and Sari, 2002; Yost et al., 2003):

Table 8.2 The temporal decay index α and spectral index β in relativistic, isotropic, self-similar deceleration phase for $\nu_m < \nu_a < \nu_c$ and $p > 2$. From Gao et al. (2013a)

	no injection		injection		
	β	α	$\alpha(\beta)$	α	$\alpha(\beta)$
ISM	slow cooling				
$\nu < \nu_m$	-2	$-\frac{1}{2}$	$\alpha = \frac{\beta}{4}$	$\frac{q}{2} - 1$	—
$\nu_m < \nu < \nu_a$	$-\frac{5}{2}$	$-\frac{5}{4}$	$\alpha = \frac{\beta}{2}$	$\frac{q-6}{4}$	—
$\nu_a < \nu < \nu_c$	$\frac{p-1}{2}$	$\frac{3(p-1)}{4}$	$\alpha = \frac{3\beta}{2}$	$\frac{(2p-6)+(p+3)q}{4}$	$\alpha = (q-1) + \frac{(2+q)\beta}{2}$
$\nu > \nu_c$	$\frac{p}{2}$	$\frac{3p-2}{4}$	$\alpha = \frac{3\beta-1}{2}$	$\frac{(2p-4)+(p+2)q}{4}$	$\alpha = \frac{q-2}{2} + \frac{(2+q)\beta}{2}$
Wind	slow cooling				
$\nu < \nu_m$	-2	-1	$\alpha = \frac{\beta}{2}$	$q - 2$	—
$\nu_m < \nu < \nu_a$	$-\frac{5}{2}$	$-\frac{7}{4}$	$\alpha = \frac{7\beta}{10}$	$\frac{3q-10}{4}$	—
$\nu_a < \nu < \nu_c$	$\frac{p-1}{2}$	$\frac{3p-1}{4}$	$\alpha = \frac{3\beta+1}{2}$	$\frac{(2p-2)+(p+1)q}{4}$	$\alpha = \frac{q}{2} + \frac{(2+q)\beta}{2}$
$\nu > \nu_c$	$\frac{p}{2}$	$\frac{3p-2}{4}$	$\alpha = \frac{3\beta-1}{2}$	$\frac{(2p-4)+(p+2)q}{4}$	$\alpha = \frac{q-2}{2} + \frac{(2+q)\beta}{2}$

$$\nu_m = (3.3 \times 10^{14} \text{ Hz})(1+z)^{1/2} \epsilon_{B,-2}^{1/2} [\epsilon_e g(p)]^2 E_{52}^{1/2} t_d^{-3/2}, \quad (8.107)$$

$$\nu_c = (6.3 \times 10^{15} \text{ Hz})(1+z)^{-1/2} \epsilon_{B,-2}^{-3/2} E_{52}^{-1/2} n^{-1} t_d^{-1/2} (1+\tilde{Y})^{-2}, \quad (8.108)$$

$$F_{\nu,\max} = (1.6 \text{ mJy})(1+z) \epsilon_{B,-2}^{1/2} E_{52} n^{-1} D_{L,28}^{-2}. \quad (8.109)$$

Hereafter the convention $Q_n = Q/10^n$ is adopted in c.g.s. units (e.g. $E_{52} = E/(10^{52} \text{ erg})$).

Notice that we have added the $(1+z)$ factor in the expressions. The rules of adding such a factor include that the cosmological rest-frame frequency (ν_{rest}) is $(1+z)$ times of the observed frequency (ν_{obs}) (redshift effect), and that the rest-frame time (t_{rest}) is $(1+z)^{-1}$ times the observed time t_{obs} (time dilation effect). The parameter $F_{\nu,\max}$ should have a $(1+z)$ coefficient. This is because the luminosity distance D_L is defined such that $F = L/(4\pi D_L^2)$ is satisfied, where F is the flux and L is the luminosity. The specific flux $F_\nu = dF/d\nu_{\text{obs}} = dL/(d\nu_{\text{obs}} 4\pi D_L^2) = L_\nu(1+z)/(4\pi D_L^2)$, where $L_\nu = dL/d\nu_{\text{rest}} = dL/[d\nu_{\text{obs}}(1+z)]$. Since afterglow modeling calculates L_ν , one needs to include the $(1+z)$ factor in the expression for F_ν .

The self-absorption frequency depends on the regime where ν_a sits. The expressions are (Gao et al., 2013a):

$$\nu_a = (5.7 \times 10^9 \text{ Hz}) \hat{z}^{-1} \frac{g^{\text{I}}(p)}{g^{\text{I}}(2.3)} E_{52}^{1/5} n_{0,0}^{3/5} \epsilon_{e,-1}^{-1} \epsilon_{B,-2}^{1/5} \quad (8.110)$$

for slow cooling $\nu_a < \nu_m < \nu_c$;

$$\nu_a = (1.5 \times 10^{10} \text{ Hz}) \hat{z}^{\frac{p-6}{2(p+4)}} \frac{g^{\text{II}}(p)}{g^{\text{II}}(2.3)} E_{52}^{\frac{p+2}{2(p+4)}} n_{0,0}^{\frac{2}{p+4}} \epsilon_{e,-1}^{\frac{2(p-1)}{p+4}} \epsilon_{B,-2}^{\frac{p+2}{2(p+4)}} t_5^{-\frac{3p+2}{2(p+4)}} \quad (8.111)$$

for $\nu_m < \nu_a < \nu_c$; and

$$\nu_a = (6.9 \times 10^6 \text{ Hz}) \hat{z}^{-1/2} \frac{g^{\text{III}}(p)}{g^{\text{III}}(2.3)} E_{52}^{7/10} n_{0,0}^{11/10} \epsilon_{B,-2}^{6/5} t_5^{-1/2} \quad (8.112)$$

for fast cooling $\nu_a < \nu_c < \nu_m$, where⁶

$$\hat{z} = \left(\frac{1+z}{2} \right), \quad (8.113)$$

$$g^{\text{I}}(p) = \left(\frac{p-1}{p-2} \right) (p+1)^{3/5} f(p)^{3/5}, \quad (8.114)$$

$$g^{\text{II}}(p) = e^{\frac{11}{p+4}} \left(\frac{p-2}{p-1} \right)^{\frac{2(p-1)}{p+4}} (p+1)^{\frac{2}{p+4}} f(p)^{\frac{2}{p+4}}, \quad (8.115)$$

$$g^{\text{III}}(p) = (p+1)^{3/5} f(p)^{3/5}, \quad (8.116)$$

$$f(p) = \frac{\Gamma(\frac{3p+22}{12}) \Gamma(\frac{3p+2}{12})}{\Gamma(\frac{3p+19}{12}) \Gamma(\frac{3p-1}{12})}. \quad (8.117)$$

Notice that the \hat{z} dependences in Eqs. (8.110)–(8.112) are derived such that when ν and t are expressed in terms of the rest-frame values, all the \hat{z} dependences cancel out (Exercise 8.4).

The afterglow lightcurves for two typical spectral regimes are presented in Fig. 8.2 (Sari et al., 1998).

The closure relations presented in Tables 8.1 and 8.2 are for $p > 2$ only. For $1 < p < 2$, the closure relations of all models are modified correspondingly, which can be found in Zhang and Mészáros (2004). In the rest of the chapter, we will focus on $p > 2$ only. For a complete survey of all the models in the $p < 2$ regime, see Gao et al. (2013a).

Several important remarks should be made:

- Since both α and β can be measured directly from the data, closure relations can be conveniently confronted with the afterglow data. However, one should keep in mind that the closure relations do not deliver the full information of the afterglow models, since the electron spectral index p has been cancelled out in the relation for some regimes. In some other regimes, both α and β are fixed values (e.g. $\nu < \nu_a$, $\nu_a < \nu < \nu_m$, $\nu_a < \nu < \nu_c$, $\nu_c < \nu < \nu_m$). For these regimes, satisfying the closure relations does not guarantee the correctness of a particular model. One also needs to check whether α and β satisfy certain specific values.
- Even though the dependencies on various parameters (E_{52} , n , $(\epsilon_e g(p))$, ϵ_B , and $(1+z)$) are well defined for a given model, the precise coefficients of various characteristic frequencies can only be calculated through numerical calculations (Granot and Sari, 2002; van Eerten and Wijers, 2009; Uhm and Zhang, 2014c). In order to get the correct

⁶ In this chapter, many $g(p)$ functions are defined. They are derived by absorbing all the p -dependent factors in the expressions of characteristic parameters in different models. The numerical order of the superscripts follows the convention of Gao et al. (2013a), which in this book may not be complete and sometimes may be repetitive. This is because we do not list all the regimes discussed by Gao et al. (2013a). The notations are self-evident, since the definitions immediately follow the expressions where those $g(p)$ functions are introduced. For a full description of all possible models, see Gao et al. (2013a).

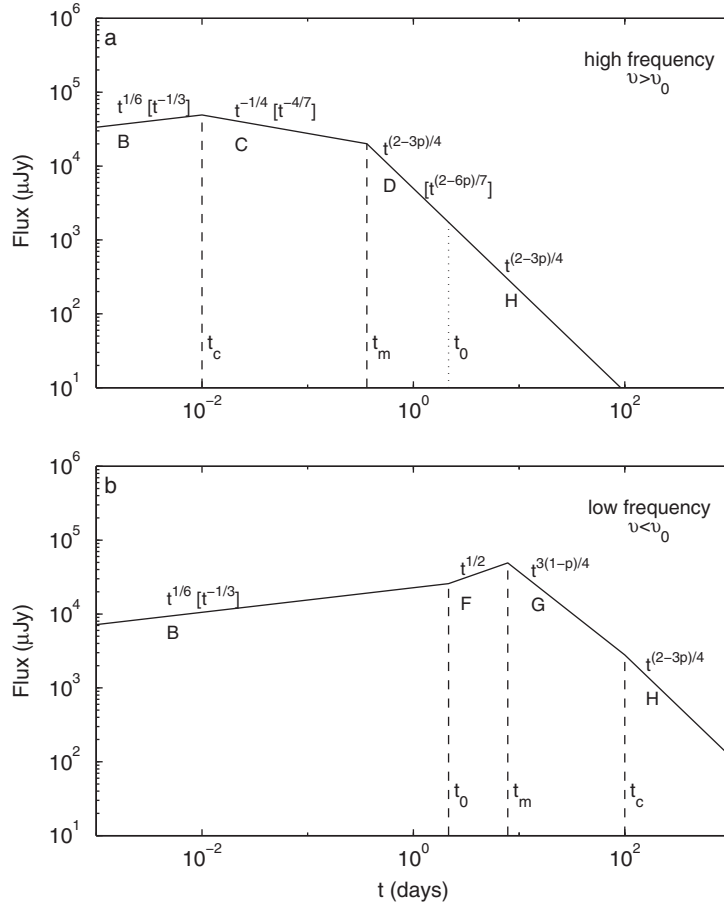


Figure 8.2

Two possible (high-frequency and low-frequency) afterglow lightcurves during the isotropic self-similar deceleration phase. Reproduced from Figure 2 in Sari et al. (1998) with permission. ©AAS.

coefficients, one needs to properly account for the following effects: the Blandford–McKee profile, the *equal-arrival-time surface* effect (or the *curvature effect*, §3.4.2), and the cooling history of electrons accelerated at different epochs. Uhm and Zhang (2014c) broke down these effects and studied how they influence the characteristic frequencies: compared with the simplest constant density assumption, the Blandford–McKee effect tends to reduce ν_m and ν_c and also lower $F_{\nu, \text{max}}$; the curvature effect, on the other hand, tends to cancel out the BM effect to make the results closer to the uniform shell case.

- Both the EATS effect and the cooling history effect tend to smooth the breaks. The cooling history effect would significantly smooth ν_c . If a sharp spectral break is observed in GRB afterglow emission, it must *not* be a cooling break (Uhm and Zhang, 2014c).
- The same cooling history effect, together with the decrease of magnetic field strength with radius as expected in the afterglow model, give a spectral index in the range $\nu_c < \nu < \nu_m$ (fast cooling below ν_m) harder than the standard value $-1/2$ (Uhm and Zhang, 2014c). As a result, the closure relations are not strict. GRBs with α and β values falling into the “grey zones” should be considered to satisfy the afterglow models (e.g. Fig. 8.3).

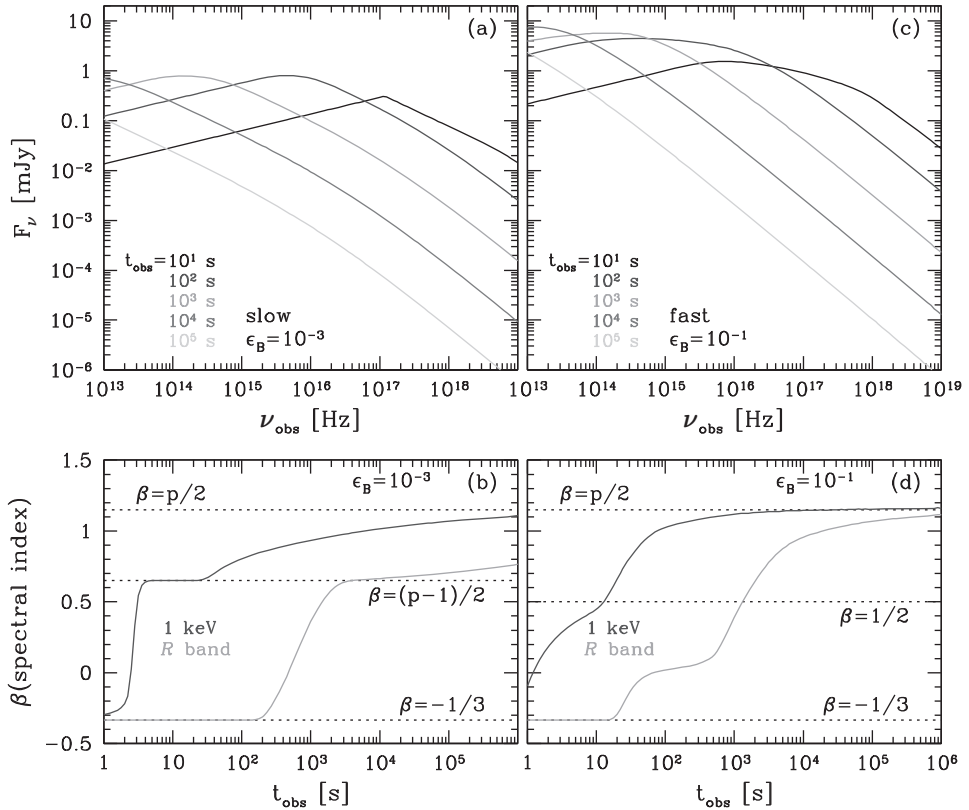


Figure 8.3

Detailed afterglow modeling that shows smooth breaks. The lower panel shows that it takes longer for the spectral indices to approach the analytical asymptotic values. From Uhm and Zhang (2014c). A black and white version of this figure will appear in some formats. For the color version, please refer to the plate section.

The EATS also has an effect on the “image” of the fireball blastwave (Waxman, 1997a; Panaitescu and Mészáros, 1998b; Sari, 1998; Granot et al., 1999). Due to the complicated interplays of characteristic frequency evolution and the EATS effect, the surface brightness distribution of the fireball image is frequency dependent (Granot et al., 1999). In the low frequencies (e.g. radio), the image is disk shaped. In high frequencies (e.g. X-rays and optical), on the other hand, the image is ring shaped (limb brightening). The reason is that at high latitudes one is looking into an earlier epoch of emission, when the shock was stronger (Lorentz factor higher). For high frequencies, earlier emission is stronger. The ring-shaped emission in high frequencies is enhanced by the caustic effect, i.e. the high-latitude emission is accumulated emission from a wider range of radii, so that emission is enhanced. The trend is opposite in the radio band. Since the lightcurve is rising initially, no enhanced ring emission is expected. Because GRBs are at cosmological distances, the images of GRB afterglows are usually not observable unless the source is close enough.

8.3.2 Constant Energy Wind Model

Similarly, one can work out the scalings for the adiabatic wind model based on Eq. (8.9). In this regime, one has $\Gamma \propto t^{-1/4} \propto r^{-1/2}$, $t \propto r^{1/2}$, and $B' \propto \Gamma n^{1/2} \propto t^{-1/4} r^{-1} \propto t^{-3/4}$, and therefore $v_m \propto \Gamma^3 B' \propto t^{-3/2}$, $v_c \propto \Gamma^{-1} t^{-2} B'^{-3} \propto t^{1/2}$, and $F_{v,\max} \propto r B' \Gamma \propto t^{-1/2}$.

Numerically taking care of the various factors affecting the coefficients, one has (Chevalier and Li, 2000; Granot and Sari, 2002; Yost et al., 2003)

$$v_m = (4.0 \times 10^{14} \text{ Hz}) (p - 0.69)(1 + z)^{1/2} \epsilon_{B,-2}^{1/2} [\epsilon_e g(p)]^2 E_{52}^{1/2} t_d^{-3/2}, \quad (8.118)$$

$$v_c = (4.4 \times 10^{13} \text{ Hz}) (3.45 - p) e^{0.45p} (1 + z)^{-3/2} \epsilon_{B,-2}^{-3/2} E_{52}^{1/2} A_*^{-2} t_d^{1/2}, \quad (8.119)$$

$$F_{v,\max} = (7.7 \text{ mJy}) (p + 0.12)(1 + z)^{3/2} \epsilon_{B,-2}^{1/2} E_{52} A_* D_{L,28}^{-2} t_d^{-1/2}, \quad (8.120)$$

and (Gao et al., 2013a)

$$v_a = (1.0 \times 10^9 \text{ Hz}) \hat{z}^{-2/5} \frac{g^{\text{VIII}}(p)}{g^{\text{VIII}}(2.3)} E_{52}^{-2/5} A_{*, -1}^{6/5} \epsilon_{e, -1}^{-1} \epsilon_{B, -2}^{1/5} t_5^{-3/5} \quad (8.121)$$

for $v_a < v_m < v_c$;

$$v_a = (4.4 \times 10^9 \text{ Hz}) \hat{z}^{\frac{p-2}{2(p+4)}} \frac{g^{\text{IX}}(p)}{g^{\text{IX}}(2.3)} E_{52}^{\frac{p-2}{2(p+4)}} A_{*, -1}^{\frac{4}{p+4}} \epsilon_{e, -1}^{\frac{2(p-1)}{p+4}} \epsilon_{B, -2}^{\frac{p+2}{2(p+4)}} t_5^{-\frac{3(p+2)}{2(p+4)}} \quad (8.122)$$

for $v_m < v_a < v_c$; and

$$v_a = (1.2 \times 10^5 \text{ Hz}) \hat{z}^{3/5} \frac{g^{\text{X}}(p)}{g^{\text{X}}(2.3)} E_{52}^{-2/5} A_{*, -1}^{11/5} \epsilon_{B, -2}^{6/5} t_5^{-8/5} \quad (8.123)$$

for $v_a < v_c < v_m$, where

$$g^{\text{VIII}}(p) = \left(\frac{p-1}{p-2} \right) (p+1)^{3/5} f(p)^{3/5}, \quad (8.124)$$

$$g^{\text{IX}}(p) = e^{\frac{273}{p+4}} \left(\frac{p-2}{p-1} \right)^{\frac{2(p-1)}{p+4}} (p+1)^{\frac{2}{p+4}} f(p)^{\frac{2}{p+4}}, \quad (8.125)$$

$$g^{\text{X}}(p) = (p+1)^{3/5} f(p)^{3/5}, \quad (8.126)$$

and \hat{z} and $f(p)$ are defined in Eqs. (8.113) and (8.117).

The closure relations can be derived (Exercise 8.5), and are collected in Tables 8.1 and 8.2. The lightcurves in different spectral regimes are presented in Fig. 8.4 (Chevalier and Li, 2000).

It is worth emphasizing two features of the wind model. First, the decay slopes are systematically steeper than those of the ISM model. Second, unlike the ISM model, the wind model has $v_c \propto t^{1/2}$, which increases with time. Such a feature, if observed, would lend support to the wind model.

8.3.3 Energy Injection Model

As shown in §8.1.1, the blastwave decelerates more slowly if it is continuously fed by energy injection. Physically there are two forms of continuous energy injection into the

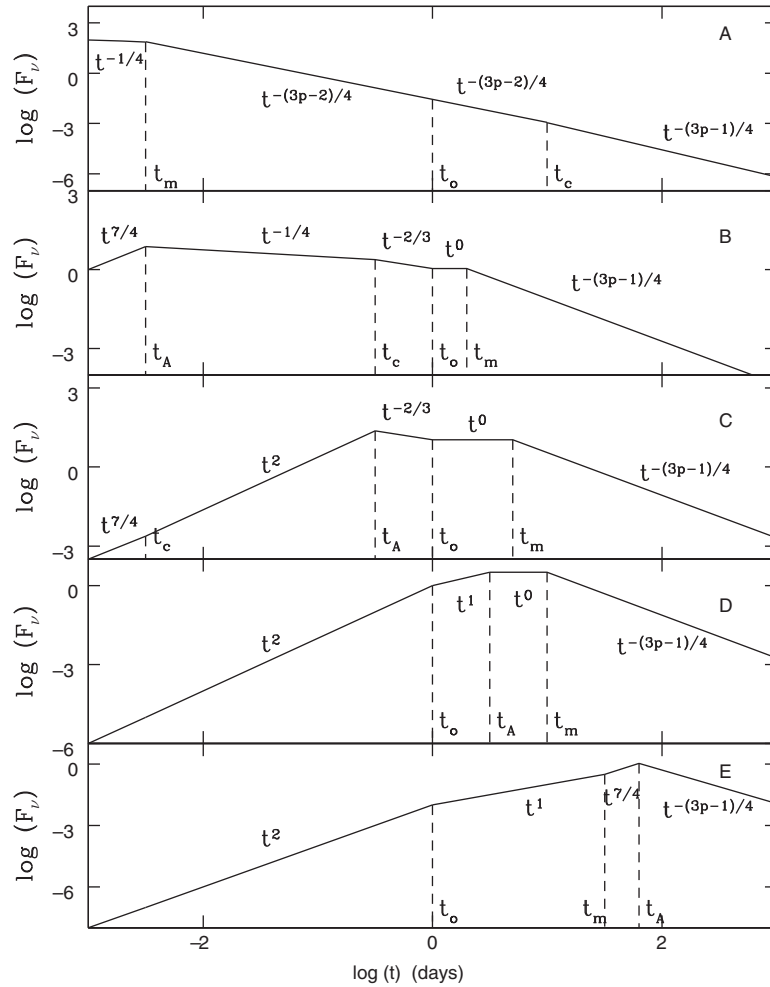


Figure 8.4 Possible afterglow lightcurves for the wind model. Reproduced from Figure 1 in Chevalier and Li (2000) with permission. ©AAS.

blastwave. The first form invokes a long-lasting central engine such as a spinning-down millisecond magnetar (Dai and Lu, 1998a; Zhang and Mészáros, 2001a), which continuously injects a Poynting flux⁷ into the blastwave, usually described as a power-law decay with time, e.g., $L(t) = L_0(t/t_0)^{-q}$. The second form does not need a long-lasting central engine. The central engine could operate briefly and inject a stratified ejecta with a distribution of bulk Lorentz factor, usually delineated as the ejecta mass above a certain Lorentz factor γ being a power-law function of the Lorentz factor, e.g. $M(> \gamma) \propto \gamma^{-s}$ (Rees and Mészáros, 1998; Sari and Mészáros, 2000; Uhm et al., 2012). Both scenarios have no or very weak reverse shock, so that the energy of any layer of ejecta is added directly to the blastwave when it piles up onto the blastwave.

⁷ The requirement of a Poynting flux removes the possibility of a reverse shock, which would change the dynamics significantly, see §8.7.

The two energy injection forms can be made equivalent through a specific relationship between the q and s parameters. In the following, we derive the formalism within the framework of energy injection in a long-lasting central engine (the q scenario). The prescription can then be generalized to the second form using the q - s relations.

For the ISM energy injection model, according to Eq. (8.19), one has

$$\nu_m \propto \Gamma^2 \gamma_e B' \propto \Gamma^4 \propto t^{-(2+q)/2}, \quad (8.127)$$

$$\nu_c \propto \Gamma^{-1} t^{-2} B'^{-3} \propto t^{(q-2)/2}, \quad (8.128)$$

$$F_{\nu, \max} \propto R^3 B' \Gamma \propto t^{1-q}. \quad (8.129)$$

For the wind energy injection model, according to Eq. (8.21), one has

$$\nu_m \propto \Gamma^3 B' \propto t^{-(2+q)/2}, \quad (8.130)$$

$$\nu_c \propto \Gamma^{-1} t^{-2} B'^{-3} \propto t^{(2-q)/2}, \quad (8.131)$$

$$F_{\nu, \max} \propto R B' \Gamma \propto t^{-q/2}. \quad (8.132)$$

The α and β values and the closure relations for various regimes can be worked out accordingly, and they are presented in Tables 8.1 and 8.2.

For the Γ -distribution energy injection form, the energy of the shell with Lorentz factor γ is added to the blastwave when the blastwave Lorentz factor Γ is decelerated to γ . One can therefore derive

$$E = E(> \gamma) \propto \gamma^{1-s} \propto \Gamma^{1-s}. \quad (8.133)$$

For the ISM model, one has

$$\Gamma \propto r^{-3/(1+s)} \propto t^{-3/(7+s)}, \quad r \propto t^{(1+s)/(7+s)}. \quad (8.134)$$

Therefore, the equivalent condition between the two forms of energy injection for the ISM model is (Zhang et al., 2006)

$$s = \frac{10-7q}{2+q}, \quad q = \frac{10-2s}{7+s}. \quad (8.135)$$

For the wind model, one has

$$\Gamma \propto r^{-1/(1+s)} \propto t^{-1/(3+s)}, \quad r \propto t^{(1+s)/(3+s)}, \quad (8.136)$$

which gives (Zhang et al., 2006)

$$s = \frac{4-3q}{q}, \quad q = \frac{4}{3+s}. \quad (8.137)$$

8.3.4 Radiative Correction

The fully radiative models demand $\epsilon_e \sim 1$. Since this is not supported by the data, we do not list the scalings of the radiative blastwaves. Studies of these models can be found, e.g., in Panaitescu and Mészáros (1998a); Dermer et al. (2000b); Ghisellini et al. (2000).

More generally, in the GRB blastwave models with radiative corrections, the blastwave dynamics include a radiative correction factor ϵ (e.g. Huang et al., 1999; Pe’er, 2012; Nava et al., 2013), which has been presented in §8.1.3. In general, numerical calculations are needed to properly take into account the radiative correction. When $\epsilon_e \ll 1$, as is usually inferred from the data modeling, the radiative correction is not significant, so that the adiabatic model scaling laws are reasonable approximations.

8.4 Jet Effect

8.4.1 Arguments for GRB Collimation

GRB ejecta are believed to be collimated. This is supported by the following independent arguments:

- Observationally, some GRBs have an isotropic γ -ray energy reaching $E_{\gamma,\text{iso}} \sim 10^{55}$ erg (e.g. GRB 990123, GRB 130427A). The rest mass energy of the Sun is $M_{\odot}c^2 \simeq 2 \times 10^{54}$ erg. In order to generate the observed isotropic energy of GRBs, one requires conversion of more than 5 solar masses of material to energy with 100% efficiency! Theoretically, it is very difficult to generate this amount of energy from a stellar-scale explosion. With a beaming correction, the total energy budget is reduced by a factor of $f_b = (1 - \cos \theta_j)$ ($\sim 1/500 = 0.002$ for long GRBs, Frail et al. 2001, and ~ 0.04 for short GRBs, Fong et al. 2015), which is much smaller: $E_{\gamma} = E_{\gamma,\text{iso}}(1 - \cos \theta_j)$.
- Observationally, the GRB luminosity is extremely “super-Eddington”. The typical observed isotropic luminosity at the peak time of a GRB is $L_{\gamma,\text{iso}} \sim 10^{52}$ erg s $^{-1}$, while the Eddington luminosity of a $10M_{\odot}$ black hole is only $L_{\text{Edd}} \sim 10^{39}$ erg s $^{-1}$. Collimation is therefore needed to continuously power the engine with gravitational energy to allow the direction of energy ejection to be different from the direction of mass feeding through accretion. Otherwise, only a very brief super-Eddington pulse can be observed, not a long-duration GRB with significant time structure.
- Finally, a steepening feature has been observed in a good fraction of GRB afterglow lightcurves. This feature is best explained by a collimated jet, and the steepening break is called a *jet break*. This is explained in more detail below.

8.4.2 Jet Break

Let us consider a conical jet with an opening angle θ_j . For simplicity, we assume an idealized *top-hat* jet with constant energy per solid angle and constant Lorentz factor within the cone, but no moving material and radiation outside the emission cone. Suppose the line of sight is well within the θ_j cone. Due to relativistic beaming, only emission inside the $1/\Gamma$ cone contributes to the observed flux. As the blastwave decelerates (Γ decreases), a steepening temporal break will appear in the lightcurve as the $1/\Gamma$ cone becomes wider than the θ_j cone, since the deficit of energy outside the cone becomes noticeable. This is a *jet break*.

The lightcurve steepening can in principle arise from two effects: the *edge effect* and the *sideways expansion effect*.

Edge Effect

This is a pure geometric effect (Fig. 8.5). Let us assume that the jet opening angle θ_j remains unchanged throughout jet evolution, or at least during the epoch when the jet break happens. Before the break time, one has $\Gamma^{-1} \ll \theta_j$. An observer has no knowledge about the collimation of the jet, since the dominant emission received is within the $1/\Gamma$ cone around the line of sight. The lightcurve calculations for the isotropic radiation (as discussed in §8.3) can describe well the observed emission properties.

Beyond the jet break, i.e. when $\Gamma^{-1} > \theta_j$ is satisfied, the observer feels the progressive deficit of energy within the Γ^{-1} cone with respect to the isotropic case, since no emission outside the jet cone is available. The lightcurve then decays faster than in the isotropic case.

During the jet break transition, the blastwave dynamics remain unchanged. The only correction factor is the ratio between the solid angle of the jet and the $(1/\Gamma)$ cone.

One can calculate the post-jet-break decay index as follows: for the ISM case, one has $\Gamma \propto t^{-3/8} \propto r^{-3/2}$, $v_m \propto t^{-3/2}$, and $v_c \propto t^{-1/2}$. The key modification is

$$F_{\nu, \max} \propto r^3 B' \Gamma \frac{\theta_j^2}{(1/\Gamma)^2} \propto r^3 B' \Gamma^3 \propto t^{-3/4}. \quad (8.138)$$

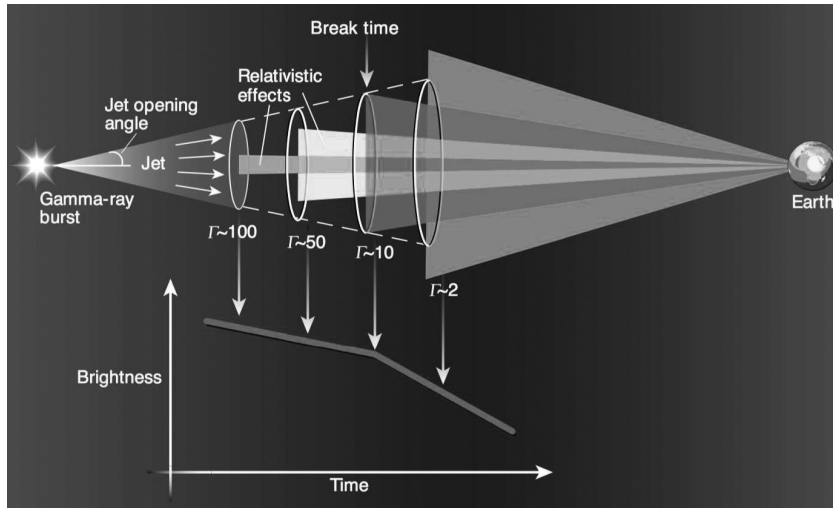


Figure 8.5

A cartoon picture for the jet break due to the edge effect. Since only those fluid elements whose Earth viewing direction is within the $(1/\Gamma)$ cone of direction of motion can give bright emission to Earth, the outer cross sections of the colored (blue, yellow, green, and orange) cones centered on Earth show the emission regions inside the jet where emission contributes to the observed flux. When the $1/\Gamma$ cone is greater than the jet opening angle θ_j (the orange cone), the observer feels a deficit of the flux, and hence the lightcurve shows a steepening break. From Woosley (2001). A black and white version of this figure will appear in some formats. For the color version, please refer to the plate section.

Table 8.3 The temporal decay index α and spectral index β after jet break for $v_a < \min(v_m, v_c)$, considering edge effect only. From Gao et al. (2013a)

		$p > 2$	
	β	α	$\alpha(\beta)$
ISM no injection			
$v < v_a$	-2	$\frac{1}{4}$	$\alpha = \frac{\beta}{8}$
$v_a < v < v_m$	$-\frac{1}{3}$	$\frac{1}{4}$	$\alpha = \frac{3\beta}{4}$
$v_m < v < v_c$	$\frac{p-1}{2}$	$\frac{3p}{4}$	$\alpha = \frac{6\beta+3}{4}$
$v > v_c$	$\frac{p}{2}$	$\frac{3p+1}{4}$	$\alpha = \frac{6\beta+1}{4}$
Wind no injection			
$v < v_a$	-2	$-\frac{1}{2}$	$\alpha = \frac{\beta}{4}$
$v_a < v < v_m$	$-\frac{5}{2}$	$\frac{1}{2}$	$\alpha = \frac{\beta}{5}$
$v_m < v < v_c$	$\frac{p-1}{2}$	$\frac{3p+1}{4}$	$\alpha = \frac{3\beta+2}{2}$
$v > v_c$	$\frac{p}{2}$	$\frac{3p}{4}$	$\alpha = \frac{3\beta}{2}$
ISM injection			
$v < v_a$	-2	$\frac{3q-2}{4}$	—
$v_a < v < v_m$	$-\frac{1}{3}$	$\frac{13q-10}{12}$	—
$v_m < v < v_c$	$\frac{p-1}{2}$	$\frac{p(q+2)-4(1-q)}{4}$	$\alpha = \frac{5q-2}{4} + \frac{(2+q)\beta}{2}$
$v > v_c$	$\frac{p}{2}$	$\frac{3q-2+p(q+2)}{4}$	$\alpha = \frac{3q-2+2\beta(q+2)}{4}$
Wind injection			
$v < v_a$	-2	$\frac{3q-4}{2}$	—
$v_a < v < v_m$	$-\frac{5}{2}$	$\frac{5q-2}{6}$	—
$v_m < v < v_c$	$\frac{p-1}{2}$	$\frac{3q-2+p(q+2)}{4}$	$\alpha = q + \frac{(2+q)\beta}{2}$
$v > v_c$	$\frac{p}{2}$	$\frac{p(q+2)-4(1-q)}{4}$	$\alpha = \frac{\beta(q+2)-2(1-q)}{2}$

This is no longer a constant (as is the case for an isotropic blastwave). The net effect is that the lightcurves of all regimes steepen by a factor of $\Gamma^2 \propto t^{-3/4}$. For example, across the jet break ($\Gamma^{-1} \sim \theta_j$), an optical lightcurve would steepen from -1 to -1.75 .

Similarly, for the wind case, one has $\Gamma \propto t^{-1/4} \propto r^{-1/2}$, $v_m \propto t^{-3/2}$, $v_c \propto t^{1/2}$, and

$$F_{v,\max} \propto rB'\Gamma \frac{\theta_j^2}{(1/\Gamma)^2} \propto rB'\Gamma^3 \propto t^{-1}, \quad (8.139)$$

which is steeper by $\Gamma^2 \propto t^{-1/2}$ than for the isotropic case.

The closure relations of the post-jet-break phase for $v_a < \min(v_m, v_c)$ due to the edge effect are presented in Table 8.3 (Gao et al., 2013a). The cases for $v_m < v_a < v_c$ and all the cases for $p < 2$ can also be found in Gao et al. (2013a).

Sideways Expansion?

Rhoads (1999) and Sari et al. (1999) considered the effect of sideways expansion of a conical jet, and suggested that it can further steepen the post-jet-break decay index. They considered a maximized sideways expansion effect and made the following arguments.

For a relativistic plasma, the sound speed is $c_s \sim c/\sqrt{3}$. For a conical jet, the opening angle would increase as (Rhoads, 1999)

$$\theta_j = \theta_{j,0} + \frac{c_s t'}{\hat{c} \hat{t}} \simeq \theta_{j,0} + \frac{1}{\sqrt{3}\Gamma}, \quad (8.140)$$

where t' and \hat{t} are the times in the comoving frame and lab frame, respectively. Sari et al. (1999) even suggested that for relativistic expansion the expansion speed may be close to speed of light, so that

$$\theta_j = \theta_{j,0} + \frac{ct'}{\hat{c} \hat{t}} \simeq \theta_{j,0} + \frac{1}{\Gamma}. \quad (8.141)$$

According to this picture, when $\Gamma^{-1} > \theta_{j,0}$, the jet opening angle increases with $1/\Gamma$, so that one may have $\theta_j \sim \Gamma^{-1}$ during the post-jet-break phase. If one defines

$$l_{\text{jet}} \equiv \left[\frac{E_{\text{jet}}}{(4\pi/3)nm_p c^2} \right]^{1/3}, \quad (8.142)$$

which is the effective ‘‘Sedov’’ radius with E_{iso} replaced by E_{jet} , one finds that the bulk Lorentz factor drops exponentially around this radius.

For the ISM model, one has (noticing that r is essentially constant after jet break)

$$\Gamma \propto \exp(-r/l_{\text{jet}}) \propto t^{-1/2}, \quad r \propto t^0, \quad (8.143)$$

$$v_m \propto \Gamma^4 \propto t^{-2}, \quad (8.144)$$

$$v_c \propto \Gamma^{-1} t^{-2} B'^{-3} \propto t^0, \quad (8.145)$$

$$F_{v,\text{max}} \propto r^3 B' \Gamma \propto r^3 \Gamma^2 \propto t^{-1}, \quad (8.146)$$

so that the post-jet-break afterglow behavior (in the slow cooling phase which is usually relevant at the jet break time) reads (Sari et al., 1999)

$$F_\nu \propto \begin{cases} \nu^{1/3} t^{-1/3}, & \nu_a < \nu < \nu_m, \\ \nu^{-(p-1)/2} t^{-p}, & \nu_m < \nu < \nu_c, \\ \nu^{-p/2} t^{-p}, & \nu > \nu_c. \end{cases} \quad (8.147)$$

One can see that the decay slope is essentially defined by the electron spectral index $\propto t^{-p}$ for the optical and X-ray bands. This is steeper than the edge effect prediction. For example, for $p = 2.2$, the edge effect only makes a transition from $\alpha = 3(p-1)/4 = 0.9$ to $0.9 + 0.75 = 1.65$, while the sideways expansion effect would make the post-break index as steep as 2.2.

Numerical simulations, on the other hand, suggest that sideways expansion is *not* significant before Γ drops below ~ 2 (e.g. Zhang and MacFadyen, 2009; Cannizzo et al., 2004;

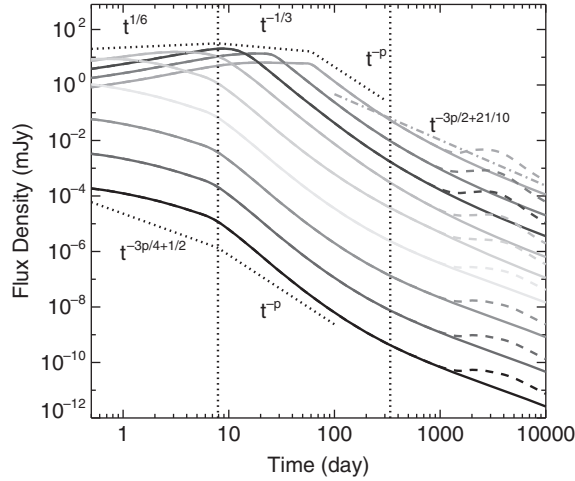


Figure 8.6

Afterglow lightcurves at different frequencies from a hydrodynamic numerical simulation. From top to bottom at late times the curves are from 10^9 to 10^{17} Hz, each with one decade increase in frequency. The two dotted vertical lines mark the jet break time (left) and the time for non-relativistic transition (right). The analytical broken power-law lightcurve (lower dotted line) is plotted for comparison. The late-time bump in each lightcurve corresponds to the emission from the counterjet as it also decelerated to non-relativistic speed. Reproduced from Figure 7 in Zhang and MacFadyen (2009) with permission. ©AAS.

van Eerten and MacFadyen, 2012). This has been confirmed by refined analytical models (e.g. Granot and Piran, 2012). On the other hand, the post-break lightcurves obtained from numerical simulations show a steeper decay slope than the simple analytical result derived from the edge effect only (Zhang and MacFadyen, 2009) (Fig. 8.6). It seems that the $\propto t^{-p}$ post-jet-break decay may still be a reasonable rough approximation. More detailed numerical simulations (van Eerten and MacFadyen, 2011) suggest that the lightcurves depend on the observer's viewing angle, even if the $1/\Gamma$ cone is inside the θ_j cone.

Inferring Jet Opening Angle from the Jet Break Time

The jet opening angle can be inferred from the afterglow break time within the framework of the above-described uniform jet model. The condition is

$$\theta_j \simeq \frac{1}{\Gamma(t_j)}. \quad (8.148)$$

For the constant energy ISM model, one may derive a simple relation

$$\begin{aligned} E_{K,\text{iso}} &\simeq \frac{4\pi}{3} r^3 n m_p c^2 \hat{\gamma} \Gamma^2 \\ &\simeq \frac{4\pi}{3} \left(4c\Gamma^2 \frac{t}{1+z} \right)^3 n m_p c^2 \hat{\gamma} \Gamma^2 \\ &= \frac{256\pi}{3} \hat{\gamma} \Gamma^8 \left(\frac{t}{1+z} \right)^3 n m_p c^5, \end{aligned} \quad (8.149)$$

so that

$$\begin{aligned}\Gamma &\simeq \left(\frac{3E_{K,\text{iso}}}{256\pi\hat{\gamma}nm_p c^5} \right)^{1/8} t^{-3/8} (1+z)^{3/8} \\ &\simeq 402(E_{52}/n)^{1/8} t^{-3/8} (1+z)^{3/8}.\end{aligned}\quad (8.150)$$

Notice that the pressure is included in deriving Eq. (8.149), so that the internal energy is boosted by a factor of $\Gamma_{\text{eff}} \simeq \hat{\gamma}$ (Eq. (8.54)) rather than Γ in most earlier works. This result is generally consistent with the derivation from the Blandford–McKee solution in Eq. (8.41) (noticing that Γ here is Γ_{bw} in that expression). Both expressions have the parameter $a = 4$ adopted (see the full discussion of the a parameter in §8.1.2), and the $(1+z)$ dependence is explicitly included here.

The jet opening angle is given by

$$\theta_j \simeq \frac{1}{\Gamma} \simeq \left(\frac{256\pi\hat{\gamma}nm_p c^5}{3E_{K,\text{iso}}} \right)^{1/8} t_j^{3/8} (1+z)^{-3/8}.\quad (8.151)$$

Since $E_{K,\text{iso}}$ is difficult to measure (see §8.10.2), usually one simply uses the observed isotropic γ -ray energy as a proxy, with an efficiency conversion factor introduced⁸

$$\tilde{\eta}_\gamma \equiv \frac{E_{\gamma,\text{iso}}}{E_{K,\text{iso}}},\quad (8.152)$$

with a typical value $\tilde{\eta}_\gamma \sim 0.2$. Putting in typical parameters, one gets

$$\begin{aligned}\theta_j &\simeq (0.063 \text{ rad}) \left(\frac{t_j}{1 \text{ day}} \right)^{3/8} \left(\frac{1+z}{2} \right)^{-3/8} \left(\frac{E_{\gamma,\text{iso}}}{10^{53} \text{ erg}} \right)^{-1/8} \\ &\quad \times \left(\frac{\tilde{\eta}_\gamma}{0.2} \right)^{1/8} \left(\frac{n}{0.1 \text{ cm}^{-3}} \right)^{1/8}.\end{aligned}\quad (8.153)$$

The coefficient 0.063 is slightly larger than the 0.057 introduced by Frail et al. (2001). The latter can be derived by adopting the Blandford–McKee solution (Eq. (8.41)).

For a wind medium, similar jet break physics applies. It has been analytically suggested that the jet break in a wind medium should be smoother than the jet break in an ISM (Kumar and Panaitescu, 2000b). Numerical simulations, however, showed that the jet break in the wind medium is also reasonably sharp (e.g. De Colle et al., 2012).

The jet opening angle for a wind medium can also be derived similarly in terms of the observed jet break time t_j (Exercise 8.6).

8.4.3 Off-Beam Emission and Orphan Afterglow

Off-Beam Emission

For an observer viewing a uniform jet outside the jet cone, the received emission differs from that of an on-beam observer due to the larger viewing angles, and hence the smaller Doppler factors of the fluid elements in the emission region.

⁸ This efficiency conversion factor $\tilde{\eta}_\gamma$ should be differentiated from the efficiency parameter η_γ defined in Eq. (2.52). The relation between the two parameters is $\eta_\gamma = \tilde{\eta}_\gamma / (1 + \tilde{\eta}_\gamma)$.

If the jet can be approximated as a point source (which means that the viewing angle $\theta_v \gg \theta_j$), one can describe jet emission with one single Doppler factor, so that one can have a simple treatment by introducing the ratio between on-beam and off-beam Doppler factors.

For an on-beam observer, one essentially has $\theta_v \sim 0$, so that

$$\mathcal{D}_{\text{on}} = \frac{1}{\Gamma(1 - \beta \cos \theta_v)} \simeq \frac{1}{\Gamma(1 - \beta)} = \Gamma(1 + \beta). \quad (8.154)$$

For an off-beam observer, one has

$$\mathcal{D}_{\text{off}} = \frac{1}{\Gamma(1 - \beta \cos \theta_v)}. \quad (8.155)$$

The ratio

$$\begin{aligned} a &\equiv \frac{\mathcal{D}_{\text{off}}}{\mathcal{D}_{\text{on}}} = \frac{\Gamma(1 - \beta)}{\Gamma(1 - \beta \cos \theta_v)} \\ &\simeq \frac{1 - \beta}{1 - \beta + \beta \theta_v^2/2} = \frac{1}{1 + \frac{\beta}{1-\beta} \frac{\theta_v^2}{2}} \simeq \frac{1}{1 + \Gamma^2 \theta_v^2} \end{aligned} \quad (8.156)$$

is a factor less than unity.

The afterglow lightcurve can then be calculated using the relation (e.g. Granot et al., 2002)

$$F_v(\theta_v, t) = a^3 F_{v/a}(0, at). \quad (8.157)$$

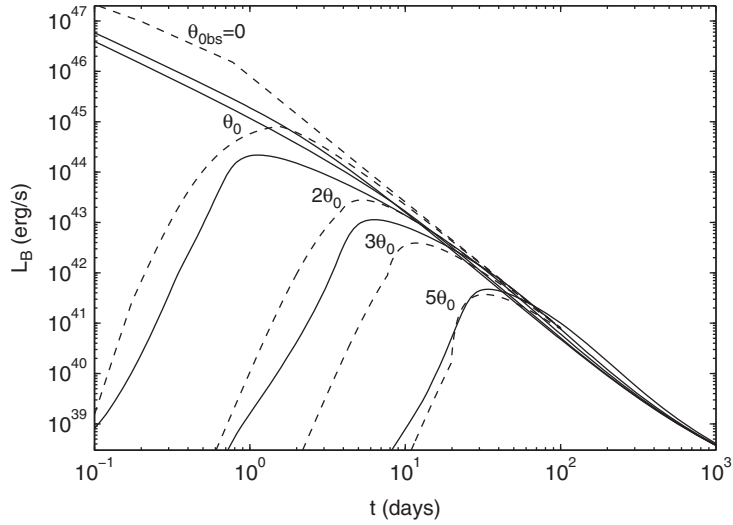
This is based on the relation $I_v(t) = \mathcal{D}^3 I'_{v'}(t')$ with the assumption of a point source (§3.4). Given the same comoving-frame intensity $I'_{v'}(t')$, one can derive (8.157) after cancelling out $I'_{v'}(t')$.

If the condition $\theta_v \gg \theta_j$ is not satisfied (which is the case with observational interest), different emission fluids in the emitting region have slightly different Doppler factors, and a careful integration along the equal-arrival-time surface (EATS) is needed.

Orphan Afterglow

The so-called “orphan” afterglow is an afterglow without a GRB (e.g. Rhoads, 1997; Granot et al., 2002; Totani and Panaitescu, 2002; Zou et al., 2007). It is hypothesized as a phenomenon of a GRB jet viewed from outside the jet cone. The predicted lightcurve of an orphan afterglow has an initial rising phase. This is because the Doppler factor \mathcal{D} gradually increases (due to reduction of Γ). The lightcurve reaches a peak when the $1/\Gamma$ cone of the ejecta starts to cover the observer’s line of sight. After this time, it behaves like that of a normal (post-jet-break) afterglow. Some example model lightcurves of orphan afterglows are presented in Fig. 8.7.

No detection has been claimed for orphan afterglows. The non-detections may be due to one or more of the following reasons: (1) they may be too faint to be detected by the current wide-field optical/radio telescopes; (2) they are difficult to identify from many other kinds of transients; (3) the GRB jets may be “structured” (§8.4.4 below), so that

**Figure 8.7**

Examples of orphan afterglow model lightcurves. Two different models (solid and dashed curves) are adopted with the viewing angle at 0, 1, 2, 3, and 5 times the jet opening angle θ_0 . Reproduced from Figure 1 in Granot et al. (2002) with permission. ©AAS.

the jets do not have a sharp edge and the predicted lightcurves are different (Rossi et al., 2008).

There could be other types of orphan afterglows. One possibility is simply that there was a GRB, but no GRB monitor was watching the sky region when it occurred, yet its afterglow could be detected. Alternatively, it has been suggested that “dirty fireballs”, whose Lorentz factors are too low to produce bright prompt emission, may produce an orphan afterglow when decelerated by an ambient medium (Huang et al., 2002).

Rapidly fading optical transients without γ -ray triggers have been discovered, e.g. PTF11agg (Cenko et al., 2013) and iPTF14yb (Cenko et al., 2015). Since they have rapid decay early on, these transients might be the afterglows of normal GRBs whose prompt γ -ray emission was not caught by γ -ray detectors.

8.4.4 Uniform and Structured Jets

Definitions

So far we have only discussed *uniform* jets, which are defined as conical jets with a uniform distribution of energy and Lorentz factor within a jet cone with a sharp edge. They can be mathematically defined by

$$\frac{dE}{d\Omega} = \begin{cases} \epsilon_0, & \theta < \theta_j, \\ 0, & \theta > \theta_j, \end{cases} \quad (8.158)$$

and

$$\Gamma(\theta) = \begin{cases} \Gamma_0, & \theta < \theta_j, \\ 1, & \theta > \theta_j. \end{cases} \quad (8.159)$$

A *structured* jet is defined to have an angular distribution in energy and Lorentz factor, i.e.

$$\frac{dE}{d\Omega} = \epsilon(\theta), \text{ and } \Gamma = \Gamma(\theta). \quad (8.160)$$

Two examples of energy distribution that are usually discussed in the literature include a power-law jet (e.g. Mészáros et al., 1998; Dai and Gou, 2001; Rossi et al., 2002; Zhang and Mészáros, 2002b; Granot and Kumar, 2003):

$$\frac{dE}{d\Omega} = \begin{cases} \epsilon_0, & \theta < \theta_m, \\ \epsilon_0 \left(\frac{\theta}{\theta_m}\right)^{-k_\theta}, & \theta > \theta_m, \end{cases} \quad (8.161)$$

where θ_m is a small angle of a narrow cone to avoid divergence at $\theta = 0$; and a Gaussian jet (e.g. Zhang and Mészáros, 2002b; Kumar and Granot, 2003; Zhang et al., 2004a):

$$\frac{dE}{d\Omega} = \epsilon_0 \cdot \exp\left(-\frac{1}{2} \frac{\theta^2}{\theta_0^2}\right). \quad (8.162)$$

The Lorentz factor structure profile can be defined accordingly, which can be (and is usually supposed to be) different from the energy structure. In view of the $\Gamma - E_{\gamma, \text{iso}}$ (Liang et al., 2010) and $\Gamma - L_{\gamma, p, \text{iso}}$ (Lü et al., 2012) relations (§2.6), the Γ profile should have a shallower dependence on θ than the energy profile.

A cartoon picture comparing the energy distribution (not geometric shape) of a (quasi-)universal structured jet and a uniform jet is shown in Fig. 8.8.

Lightcurves

The afterglow lightcurves of a structured jet are somewhat different from those of a uniform jet. Since $dE/d\Omega$ is a function of angle from the jet axis, the lightcurve depends on the observer's viewing angle θ_v from the jet axis.

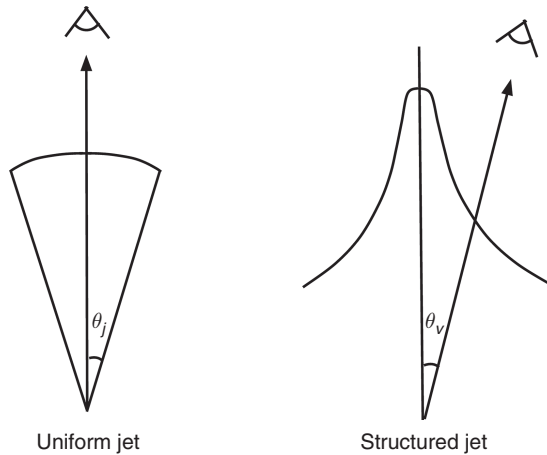


Figure 8.8

A cartoon picture of the energy distribution (not geometric shape) of a (quasi-)universal structured jet (right) for which the viewing angle θ_v plays a crucial role, in comparison with that of a uniform jet (left) for which the jet opening angle θ_j is more crucial.

We first consider a *power-law* jet.

For an on-axis configuration, since the observer would receive a progressively smaller addition of energy into the $1/\Gamma$ cone during the deceleration phase, the lightcurves are expected to be steeper than the isotropic cases (Mészáros et al., 1998; Dai and Gou, 2001; Panaitescu, 2005). The decay index may be expressed as (Panaitescu, 2005) (Exercise 8.7)

$$\alpha = \frac{1}{4 - \frac{1}{2}k_\theta} \begin{cases} 3p - 3 + \frac{3}{2}k_\theta, & \nu_m < \nu < \nu_c, \\ 3p - 2 + k_\theta, & \nu > \nu_c, \end{cases} \quad (8.163)$$

for the ISM model, and

$$\alpha = \frac{1}{4 - k_\theta} \begin{cases} 3p - 1 - \frac{1}{2}k_\theta(p - 1), & \nu_m < \nu < \nu_c, \\ 3p - 2 - \frac{1}{2}k_\theta(p - 2), & \nu > \nu_c, \end{cases} \quad (8.164)$$

for the wind model.

For an off-axis configuration, what is relevant is the evolution of the effective energy per solid angle along the line of sight (θ_v, ϕ_v) , i.e.

$$\bar{\epsilon}(\theta_v, \phi_v, t) = \bar{\epsilon}(\theta_v, t) = \frac{\int_{\theta_v - 1/\Gamma}^{\theta_v + 1/\Gamma} \epsilon(\theta, t) \sin \theta d\theta}{\int_{\theta_v - 1/\Gamma}^{\theta_v + 1/\Gamma} \sin \theta d\theta}. \quad (8.165)$$

When $\Gamma \gg 1/\theta_v$ (or $\theta_v \gg 1/\Gamma$) and for small angle θ , it is easy to prove (Zhang and Mészáros, 2002b)

$$\bar{\epsilon}(\theta_v, t) = \frac{\int_{\theta_v - 1/\Gamma}^{\theta_v + 1/\Gamma} \epsilon_0 \theta_m^{k_\theta} \theta^{1-k_\theta} d\theta}{\int_{\theta_v - 1/\Gamma}^{\theta_v + 1/\Gamma} \theta d\theta} \simeq \epsilon_0 \left(\frac{\theta_v}{\theta_m} \right)^{-k_\theta} = \epsilon(\theta_v). \quad (8.166)$$

In other words, the energy per solid angle within the observer's (distorted) $1/\Gamma$ cone remains essentially constant, so that the observer would think that it is an isotropic fireball. The energy gain from the near-side of the cone with respect to the jet axis is essentially cancelled by the energy deficit from the far-side of the cone. As the $1/\Gamma$ cone starts to cover the jet axis, the observer will feel the energy deficit and a jet break appears. So, within this picture, the lightcurve should be similar to that of a uniform jet, except that the jet opening angle θ_j is replaced by the view angle θ_v (Zhang and Mészáros, 2002b; Rossi et al., 2002). Detailed numerical calculations confirmed such a speculation (Fig. 8.9 left, Granot and Kumar 2003).

For a *Gaussian* jet, since the energy distribution is essentially uniform for $\theta < \theta_0$, the on-axis lightcurve is similar to the case of a uniform jet. When the line of sight is outside the Gaussian angle θ_0 , a similar effect to the power-law jet applies, so that θ_v defines the jet break time. Overall, one may apply $\max(\theta_0, \theta_v)$ to define the jet break time. Detailed numerical calculations (Kumar and Granot, 2003) confirmed this general picture, but for $\theta_v > \theta_0$ a “hump” feature shows up around the jet break time, and the feature becomes progressively significant as θ_v increases (Fig. 8.9 right).

Standard Energy Reservoir and Universal Jet

One important motivation for introducing structured jets was to interpret the observed anti-correlation between $E_{\gamma, \text{iso}}$ and θ_j , or effectively a rough “standard energy reservoir” of

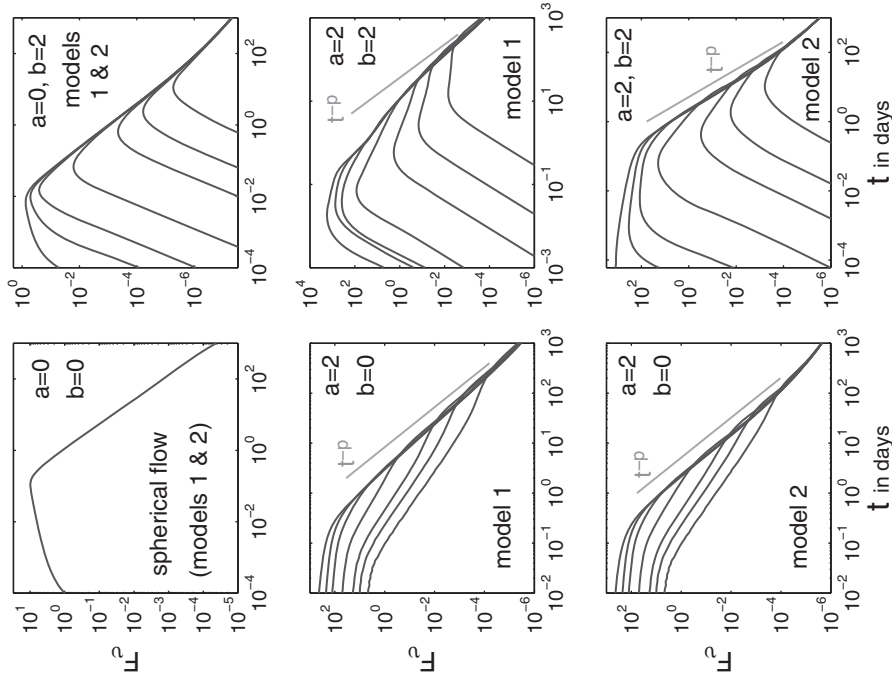


Figure 8.9

Model lightcurves for structured jets. *Left:* Power-law jets. *Right:* Gaussian jets compared with power-law jets. Reproduced from Figures 4 and 5 in Kumar and Granot (2003) with permission. ©AAS.

GRBs (Frail et al., 2001; Bloom et al., 2003; Berger et al., 2003b). The observed trend, $E_\gamma \simeq E_{\gamma,\text{iso}} \cdot \theta_j^2/2 \sim \text{const}$, can be translated to

$$\frac{dE}{d\Omega} \propto E_{\gamma,\text{iso}} \propto \theta_v^{-2}. \quad (8.167)$$

So the observational fact may be understood as the GRBs having not only a standard energy reservoir, but also a universal structure with a power-law index of $k_\theta \sim -2$ (Rossi et al., 2002; Zhang and Mészáros, 2002b). Within this picture, the measured jet opening angle is essentially the observer's viewing angle from the jet axis of the universal jets. This is a unified paradigm similar to the unified model of AGNs, which interprets different observed AGN species as an observer's viewing angle effect (Urry and Padovani, 1995).

Observationally, the energy reservoir of GRBs is not fully standard (Frail et al., 2001), especially in view of the new observations in the post-*Swift* era (Liang et al., 2008a; Racusin et al., 2009), see §2.6. So the GRB jet structure does not have to be universal. Zhang and Mészáros (2002b) suggested that the jets can be *quasi-universal*, with different GRBs having somewhat different structures, with the power-law index distributed in a range around -2 . The structure can even be Gaussian. Introducing a distribution of structured jet parameters, the observed GRB properties can be reproduced (e.g. Lloyd-Ronning et al., 2004; Zhang et al., 2004a; Dai and Zhang, 2005). For example, GRBs with Gaussian jets with $\theta_0 \sim 5.7^{+3.4}_{-2.1}$ degrees and $\log(E_j/\text{erg}) \sim 51.1 \pm 0.3$ can reproduce the GRB observations well (Zhang et al., 2004a).

Luminosity Functions

Within the quasi-universal structured jet scenario, the distribution of GRB luminosity is closely related to the distribution of the observer's viewing angle, which is geometrically defined. One therefore has a prediction of the GRB luminosity function.

The viewing angle distribution follows

$$N(\theta)d\theta \propto \sin\theta d\theta \propto \theta d\theta. \quad (8.168)$$

The GRB luminosity function for a structured jet can be predicted once the jet structure is specified (Zhang and Mészáros, 2002b; Rossi et al., 2002), i.e.

$$N(L)dL = N(\epsilon)d\epsilon = N(\theta)d\theta = \sin\theta d\theta. \quad (8.169)$$

For a power-law jet, one has

$$N(L)dL \propto L^{-1-2/k_\theta} dL \propto L^{-2} dL \quad (k_\theta = 2); \quad (8.170)$$

and for a Gaussian jet, one has

$$N(L)dL \propto L^{-1} dL. \quad (8.171)$$

The derived GRB luminosity functions (e.g. Wanderman and Piran, 2010, 2015; Sun et al., 2015) have slopes within this predicted range, suggesting that the data are not inconsistent with the structured jet model predictions.

More Complicated Jet Structures

Besides these two forms of structured jets, more complicated structured jets have been discussed in the literature.

Several authors have discussed the two-component jet model. According to this model, the GRB outflow is composed of a narrow jet, usually with a higher $L_{\gamma, \text{iso}}$ and a larger Γ , and a wider jet surrounding it, usually with a lower $L_{\gamma, \text{iso}}$ and a smaller Γ . Depending on the viewing angle, the two-component jet can account for a variety of lightcurve features, such as an early jet break and late-time re-brightening (Huang et al., 2004; Peng et al., 2005; Wu et al., 2005b). The model was used to interpret the afterglow data for several GRBs, such as GRB 030329 (Berger et al., 2003a) and GRB 080319B (Racusin et al., 2008). The collapsar model offers a natural mechanism for generating a two-component jet: a narrow, highly relativistic jet emerging from a star is surrounded by a wider, less relativistic “cocoon” (Ramirez-Ruiz et al., 2002; Zhang et al., 2004b). Alternatively, within the magnetized jet scenario with a neutron-rich jet composition, a narrow jet may form with a magnetically confined proton component, while a wide jet may form with a neutron component that is not subject to magnetic confinement (Peng et al., 2005).

Another possibility is that the GRB jets are “patchy”, i.e. the emission comes from many bright patches or “mini-jets” within a broad jet cone (Kumar and Piran, 2000a; Yamazaki et al., 2004). These mini-jets may be local Lorentz-boosted emission regions within the bulk jet, which may be related to magnetic reconnections, or turbulence in a magnetically dominated jet (Lyutikov and Blandford, 2003; Narayan and Kumar, 2009; Zhang and Yan, 2011; Zhang and Zhang, 2014). Numerical simulations (Deng et al., 2015) indeed show the existence of such mini-jets in magnetic dissipation regions, and observationally these mini-jets may be responsible for the so-called fast variability component observed in GRBs (Gao et al., 2012).

8.5 Relativistic to Non-Relativistic Transition

The initially relativistic blastwave will eventually be decelerated to reach the non-relativistic/Newtonian phase, when the 4-speed $\Gamma\beta = \sqrt{\Gamma^2 - 1}$ drops below 1, or $\Gamma < \sqrt{2}$.

8.5.1 Newtonian Dynamics

In the deep Newtonian phase, the blastwave dynamics can be derived from the following simple scaling relations (e.g. Wijers et al., 1997; Dai and Lu, 1999; Huang and Cheng, 2003).

The kinetic energy remains a constant, i.e.

$$\frac{1}{2}mv^2 = \frac{1}{2} \left(\frac{4}{3}\pi r^3 n m_p c^2 \right) v^2 = \text{const.} \quad (8.172)$$

This gives $v \propto r^{-3/2} \propto (vt)^{-3/2}$, so that $v^{5/2} \propto t^{-3/2}$, i.e.

$$v \propto r^{-3/2} \propto t^{-3/5}, \quad r \propto t^{2/5}. \quad (8.173)$$

Again considering a fixed fraction of the shock energy going to magnetic fields, one has

$$\frac{B^2}{8\pi} \propto \frac{1}{2} \rho v^2, \quad (8.174)$$

$$B \propto v \propto t^{-3/5}. \quad (8.175)$$

One can then derive the scaling relations for the characteristic quantities:

$$\gamma_m \propto v^2 \propto t^{-6/5}, \quad (8.176)$$

$$v_m \propto \gamma_m^2 B \propto t^{-12/5} \cdot t^{-3/5} \propto t^{-3}, \quad (8.177)$$

$$v_c \propto t^{-2} B^{-3} \propto t^{-2} \cdot t^{9/5} \propto t^{-1/5}, \quad (8.178)$$

$$F_{v,\max} \propto r^3 B \propto t^{6/5} \cdot t^{-3/5} \propto t^{3/5}. \quad (8.179)$$

In the non-relativistic regime, electrons should be in the slow cooling ($v_m < v_c$) regime. The afterglow temporal indices for different spectral regimes can then be derived as (Exercise 8.8)

$$F_\nu \propto \begin{cases} \nu^2 t^{-2/5}, & \nu < \nu_a, \\ \nu^{1/3} t^{8/5}, & \nu_a < \nu < \nu_m, \\ \nu^{-(p-1)/2} t^{(21-15p)/10}, & \nu_m < \nu < \nu_c, \\ \nu^{-p/2} t^{(4-3p)/2}, & \nu > \nu_c. \end{cases} \quad (8.180)$$

For $p = 2.3$, the decay slopes are -1.35 and -1.45 for $\nu_m < \nu < \nu_c$ and $\nu > \nu_c$, respectively. This is steeper than the isotropic relativistic case.

The characteristic parameters with appropriate coefficients can be derived (Gao et al., 2013a). For the ISM case,⁹ one has

$$v_m = (2.0 \times 10^{14} \text{ Hz}) (1+z)^2 \frac{G(p)}{G(2.3)} E_{52} n_{0,0}^{-1/2} \epsilon_{e,-1}^2 \epsilon_{B,-2}^{1/2} t_5^{-3}, \quad (8.181)$$

$$v_c = (7.0 \times 10^{15} \text{ Hz}) (1+z)^{-4/5} E_{52}^{-3/5} n_{0,0}^{-9/10} \epsilon_{B,-2}^{-3/2} t_5^{-1/5}, \quad (8.182)$$

$$F_{v,\max} = (2.3 \times 10^2 \text{ } \mu\text{Jy}) (1+z)^{2/5} E_{52}^{4/5} n_{0,0}^{7/10} \epsilon_{B,-2}^{1/2} D_{28}^{-2} t_5^{3/5}, \quad (8.183)$$

$$\nu_a = (1.4 \times 10^7 \text{ Hz}) \hat{z}^{-11/5} \frac{g^I(p)}{g^I(2.3)} E_{52}^{-1/5} n_{0,0} \epsilon_{e,-1}^{-1} \epsilon_{B,-2}^{1/5} t_5^{6/5} \quad (8.184)$$

for $\nu_a < \nu_m < \nu_c$, and

$$\nu_a = (3.3 \times 10^{10} \text{ Hz}) \hat{z}^{\frac{2p-6}{p+4}} \frac{g^{II}(p)}{g^{II}(2.3)} E_{52}^{\frac{p}{p+4}} n_{0,0}^{\frac{6-p}{2(p+4)}} \epsilon_{e,-1}^{\frac{2(p-1)}{p+4}} \epsilon_{B,-2}^{\frac{p+2}{2(p+4)}} t_5^{-\frac{3p-2}{p+4}} \quad (8.185)$$

for $\nu_m < \nu_a < \nu_c$, where

⁹ This is usually the case at the late stage of blastwave evolution, since a stellar wind ends at a termination shock beyond which the medium is an ISM. For a discussion of such a transition, see §7.3.4.

$$G(p) = \left(\frac{p-2}{p-1} \right)^2, \quad (8.186)$$

$$g^I(p) = \left(\frac{p-1}{p-2} \right) (p+1)^{3/5} f(p)^{3/5}, \quad (8.187)$$

$$g^{II}(p) = e^{\frac{219}{p+4}} \left(\frac{p-2}{p-1} \right)^{\frac{2(p-1)}{p+4}} (p+1)^{\frac{2}{p+4}} f(p)^{\frac{2}{p+4}}, \quad (8.188)$$

and \hat{z} and $f(p)$ are defined in Eqs. (8.113) and (8.117), respectively.

8.5.2 Transition

The lightcurves in the Newtonian phase are steeper than those in the relativistic phase, but are shallower than the post-jet-break phase in the relativistic regime. So one may consider two types of relativistic-to-non-relativistic (R–NR) transitions.

If the transition happens before the jet break, one would see a steepening break. This model was discussed as an alternative interpretation of afterglow steepenings around the day time scale in the early years, e.g. the case for GRB 990123 by Dai and Lu (1999). This model demands an extremely high circumburst medium density, $n \sim 10^6 \text{ cm}^{-3}$.

More likely, the ambient density is low, and the R–NR transition occurs after the jet break. The lightcurve will first display a steepening due to the jet break, and then transit to a shallower decay to enter the Newtonian regime in the time scale of years (e.g. Livio and Waxman, 2000; Zhang and MacFadyen, 2009), see Fig. 8.6.

Observationally, it is very difficult to see the NR phase in the optical band, since the afterglow lightcurve often flattens due to the contamination from the host galaxy light before reaching the non-relativistic phase. The transition may be more easily observed in the radio band, especially if the source is nearby. For example, a R–NR transition was observed in the radio band for the nearby high-luminosity GRB 030329 (e.g. van der Horst et al., 2008).

Since it is envisaged that GRBs launch a bipolar jet, models also predict that emission from the counterjet would emerge in the late radio afterglow lightcurve when both jets enter the Newtonian regime (Zhang and MacFadyen 2009, see Fig. 8.6). The late radio data of GRB 030329 are consistent with such a model (van der Horst et al., 2008).

8.6 Synchrotron Self-Compton Contribution

Synchrotron self-Compton (SSC) may play an important role in shaping the GRB afterglow lightcurves. The effect of SSC on GRB afterglows has been discussed in many papers (e.g. Mészáros et al., 1994; Wei and Lu, 1998; Dermer et al., 2000a; Panaitescu and Kumar, 2000; Zhang and Mészáros, 2001b; Sari and Esin, 2001). A treatment of the SSC process in different spectral regimes is detailed in §5.2, see also Gao et al. (2013c).

The time-dependent synchrotron + SSC spectra and the frequency-dependent synchrotron + SSC lightcurves can be readily calculated by combining the SSC treatment in §5.2, the synchrotron prescription introduced in §8.2, as well as blastwave dynamics discussed in §8.1. Here we summarize only the effects of SSC.

In general, there are two effects. First, SSC contributes to the cooling of the electron Lorentz factor through the Y parameter (§5.2.3). This would effectively lower the flux above the cooling frequency compared with the case without the consideration of SSC.

Second, relative to synchrotron, SSC becomes important in the regime with low ϵ_B and high ϵ_e . In a certain parameter space in the ϵ_e – ϵ_B plane (Fig. 8.10 left, Zhang and Mészáros 2001b), the SSC process forms a distinct spectral component, which would give a dominant contribution to the GeV energies (Dermer et al. 2000a; Zhang and Mészáros 2001b, see Fig. 8.10 right). This condition is derived by demanding that the SSC flux at the νF_ν peak exceeds the synchrotron flux at the same frequency (Zhang and Mészáros, 2001b). If the ambient density is high enough, the SSC component may also emerge in the X-ray band at a late enough time (Panaitescu and Kumar, 2000; Zhang and Mészáros, 2001b; Sari and Esin, 2001).

Observationally, most Fermi-LAT-detected GeV afterglows are consistent with having a synchrotron origin (Gao et al., 2009; Kumar and Barniol Duran, 2009, 2010; Ghisellini et al., 2010). The GeV afterglow of GRB 130427A has photons above the maximum synchrotron frequency (Ackermann et al., 2014), and likely has a significant contribution from the SSC component (Fan et al., 2013b; Tam et al., 2013; Liu et al., 2013), cf. Kouveliotou et al. (2013).

8.7 Early Deceleration Phase and Reverse Shock Emission

So far we have considered a blastwave system with forward shock only. In the early deceleration phase, as the forward shock plows into the circumburst medium, a reverse

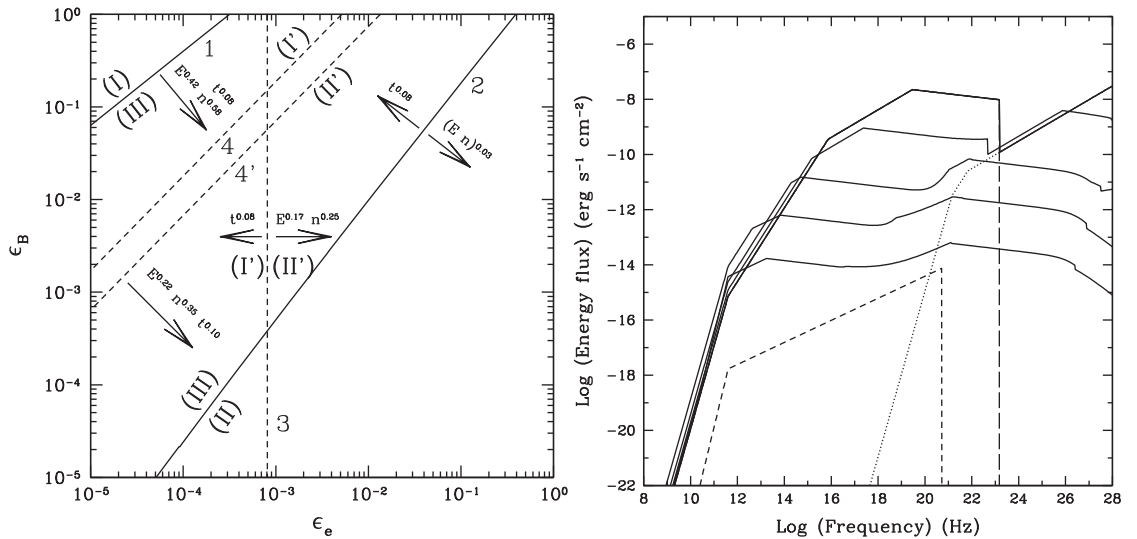


Figure 8.10

Left: The ϵ_e – ϵ_B parameter space that shows the SSC-dominated regime. Region II is the SSC-dominated regime. *Right:* The predicted time-dependent afterglow spectra as a function of time in the SSC-dominated regime. From Zhang and Mészáros (2001b).

shock propagates into the ejecta itself. The dynamics of this system are more complicated. In this section, we study this phase in detail. We dedicate the most space to the constant density (ISM) model (§8.7.1 to §8.7.3). The case of the high- σ regime is discussed in §8.7.4. The wind model is introduced in §8.7.5.

8.7.1 Reverse Shock Crossing Dynamics

Reverse Shock Crossing

We consider a matter-dominated conical jet¹⁰ with energy E , width Δ , Lorentz factor Γ_0 running into a constant density medium with density n . Upon interaction between the jet and the medium, a pair of shocks develop: the FS propagates into the medium, and the RS propagates into the ejecta shell itself. It takes some time before the RS crosses the ejecta shell. The RS is initially Newtonian. The RS shock speed (with respect to the ejecta) increases with time due to the deceleration of the blastwave, and transitions from non-relativistic to relativistic at a characteristic radius R_N .

The shock crossing dynamics can be delineated as follows. Let us consider a segment $\overline{AB} = dx$ of the unshocked shell, where A and B are the rear and front ends of the segment, respectively. In the beginning (at the lab-frame time \hat{t}_0) the RS is at the front point B . After a lab-frame time $d\hat{t}$, the RS shocks through the shell segment and compresses the shell to a width dx' . Since the upstream, downstream, and the RS all stream forward, at $\hat{t} + d\hat{t}$, the compressed shell segment is at $\overline{A'B'} = dx'$, with A' leading B . One can easily write $\overline{AA'} = \beta_4 c d\hat{t}$, $\overline{BB'} = \beta_3 c d\hat{t}$ (since the point B entered the blastwave starting from \hat{t}_0), and $\overline{BA'} = \beta_{RS} c d\hat{t}$. Simple geometry gives $\beta_4 c d\hat{t} - dx = \beta_3 c d\hat{t} - dx' = \beta_{RS} c d\hat{t}$, or (Sari and Piran, 1995)

$$(\beta_4 - \beta_3) c d\hat{t} = dx - dx' = dx \left(1 - \frac{\gamma_4 n_4}{\gamma_3 n_3} \right). \quad (8.189)$$

When deriving the last equation, particle conservation in the shell segment before and after the RS crossing, i.e. $dx \gamma_4 n_4 = dx' \gamma_3 n_3$, has been applied. Noticing $d\hat{t} = dr / \beta_3 c$, one gets

$$\frac{dx}{c} \left(1 - \frac{\gamma_4 n_4}{\gamma_3 n_3} \right) = \frac{\beta_4 - \beta_3}{\beta_3} \frac{dr}{c}. \quad (8.190)$$

For a blastwave system with four regions (§4.3 and Fig. 4.2), one has (noticing $\hat{\gamma} = (4\gamma + 1)/3\gamma$, see Eq. (4.138))

$$\frac{n_4}{n_1} = \frac{\gamma_{21}^2 - 1}{\gamma_{34}^2 - 1} = \frac{\gamma_3^2 - 1}{\gamma_{34}^2 - 1} = \frac{\beta_3^2}{(\beta_4 - \beta_3)^2} \frac{1}{\gamma_4^2}, \quad (8.191)$$

where $\gamma_{34}^2 = 1/(1 - \beta_{34}^2)$, and $\beta_{34} = (\beta_4 - \beta_3)/(1 - \beta_3 \beta_4)$ have been applied. Plugging this into Eq. (8.190), one gets¹¹

¹⁰ In the early phase, the $1/\Gamma$ cone is much smaller than the jet opening angle θ_j . One can therefore treat the jet as an isotropic fireball.

¹¹ This is essentially Eq. (1) of Kobayashi (2000), which we derive rigorously here (with special acknowledgment to Shiho Kobayashi).

$$\frac{dr}{c} = \gamma_4 \left(\frac{n_4}{n_1} \right)^{1/2} \frac{dx}{c} \left(1 - \frac{\gamma_4 n_4}{\gamma_3 n_3} \right). \quad (8.192)$$

One may integrate Eq. (8.192) to obtain the lab-frame shock crossing time

$$\hat{t}_\Delta = \gamma_4 \left(\frac{n_4}{n_1} \right)^{1/2} \frac{\Delta}{c} \left(1 - \frac{\gamma_4 n_4}{\gamma_3 n_3} \right). \quad (8.193)$$

Noticing $n_4/n_3 = 1/4\gamma_{34}$, one has $(1 - \gamma_4 n_4/\gamma_3 n_3) \simeq 3/4$ for a non-relativistic RS, and $\sim 1/2$ for a relativistic RS. Equation (8.193) therefore reproduces Eqs. (6) and (8) of Sari and Piran (1995), who made more approximations than the derivation here.

Characteristic Radii and Thin vs. Thick Shells

In the GRB deceleration problem, there are two characteristic length scales: the lab-frame shell width Δ ($\sim cT$, where T is the duration of the burst) and the Sedov length l (Eq. (7.94)). For an order-of-magnitude estimate, one may drop out the coefficients and define $l \sim (E/nm_p c^2)^{1/3}$. Together with the initial Lorentz factor $\Gamma_0 = \gamma_4$, one can define four more relevant length scales or characteristic radii (Sari and Piran, 1995):

- the radius at which the blastwave collects a factor $1/\Gamma_0$ of the initial mass in the fireball:

$$R_\Gamma \sim \frac{l}{\Gamma_0^{2/3}} \quad (8.194)$$

(this is the deceleration radius for a thin shell);

- the radius at which the reverse shock transitions from Newtonian to relativistic:

$$R_N \sim \frac{l^{3/2}}{\Delta^{1/2} \Gamma_0^2}; \quad (8.195)$$

- the radius at which the reverse shock crosses the shell:

$$R_\Delta \sim l^{3/4} \Delta^{1/4}; \quad (8.196)$$

- and the shell spreading radius:

$$R_s \sim \Gamma_0^2 \Delta. \quad (8.197)$$

While the derivations of R_Γ and R_s are straightforward, one needs to make use of Eq. (8.193) in order to derive R_N and R_Δ . The key is to write

$$\frac{n_4}{n_1} = \frac{E}{\Gamma_0 m_p c^2 4\pi r^2 (\Gamma_0 \Delta) n_1} \sim \frac{l^3}{\Gamma_0^2 \Delta r^2} \propto r^{-2} \Delta^{-1}, \quad (8.198)$$

where the proportionality $\propto r^{-2}$ applies if the shell has not entered the spreading regime ($\Delta = \Delta_0 = \text{const}$). The shock crossing radius R_Δ (Eq. (8.196)) can be solved by combining Eqs. (8.193) and (8.198) by demanding $r = R_\Delta$. To solve R_N , one should require

$$\left(\frac{n_4}{n_1} \right)^{1/2} \frac{1}{\gamma_4} \sim 1 \quad (8.199)$$

in Eq. (8.193). This is because from Eq. (8.198) one can see $(n_4/n_1)^{1/2}/\gamma_4 \gg 1$ in the non-relativistic regime ($\gamma_3 \sim \gamma_4$, γ_{34} is slightly larger than 1), but is $(n_4/n_1)^{1/2}/\gamma_4 \ll 1$ in the relativistic regime ($\sim 2\gamma_3^2/\gamma_4^2$). Combining Eqs. (8.199) and (8.193), one can derive the expression for R_N (Eq. (8.195)).

If one defines a parameter

$$\xi \equiv \left(\frac{l}{\Delta}\right)^{1/2} \Gamma_0^{-4/3} = \left(\frac{t_\gamma}{T}\right)^{1/2}, \quad (8.200)$$

one has the relation (Sari and Piran, 1995)

$$\frac{R_N}{\xi} = R_\Gamma = \sqrt{\xi} R_\Delta = \xi^2 R_s. \quad (8.201)$$

Notice that the second part of Eq. (8.200) expresses ξ in terms of the ratio between two characteristic time scales (Zhang and Kobayashi, 2005), where t_γ is essentially the thin shell deceleration time t_{dec} presented in Eq. (7.80) but with the coefficient of order unity dropped out.

There are two regimes:

- $\xi > 1$ ($t_\gamma > T$): This is the thin shell, or the Newtonian RS regime (see also §7.3.4). In this regime, one has $R_s < R_\Delta < R_\Gamma < R_N$. With shell spreading considered ($\Delta \sim r/\Gamma^2$), one reaches $R_\Delta \sim R_\Gamma \sim R_N$ when $\xi \sim 1$. This suggests that, at the deceleration radius, the RS crosses the shell and in the meantime reaches trans-relativistic speed.
- $\xi < 1$ ($t_\gamma < T$): This is the thick shell, or the relativistic RS regime. In this regime, one has $R_N < R_\Gamma < R_\Delta < R_s$. The RS first enters the relativistic phase at R_N ; R_Γ is no longer a relevant radius, and the shell reaches full deceleration at the shock crossing radius R_Δ .

Dynamics

During the reverse shock crossing phase, the dynamics of the blastwave can be solved by considering the shock jump conditions at both FS and RS, as well as the balancing conditions at the contact discontinuity (§4.3). After the RS shock crossing, the shocked ejecta undergoes a self-adjustment phase before transiting to the Blandford–McKee profile. The dynamics during this phase have been studied numerically (Kobayashi and Sari, 2000).

A simple treatment assumes constant pressure and constant Lorentz factor in both Regions II and III (shocked medium and shocked ejecta, see §4.3). Even though such a treatment does not fully conserve energy, the approximation is reasonably accurate if the RS-crossing time is short enough (i.e. for the case that Δ is defined by the duration of GRBs, without considering a long-lasting RS due to either a long-lasting central engine or a distribution of Lorentz factors in the ejecta). The following treatment is based on this assumption following Kobayashi (2000). The input parameters in the problem include: total energy E , initial Lorentz factor Γ_0 , initial shell width Δ_0 , duration $T = \Delta_0/c$, medium density n_1 , and the shell density n_4 (which is a function of r). One can then derive the blast-wave Lorentz factor $\gamma_2 = \gamma_3$. This settles the parameters in Regions II and III, so that the synchrotron spectra in both the FS and RS can be calculated.

One important task is to quantify the number of electrons in Region III, $N_{e,3}$, as a function of time. This can be estimated as $N_{e,3} \sim n_3 4\pi r^2 \gamma_3 \int_0^{x'} dx' \propto n_3 r^2 \gamma_3 \int_0^r \gamma_4^{-1} (n_4/n_1)^{-1/2} dr \propto n_3 r^3 \gamma_3 n_4^{-1/2}$ (since $\gamma_4 = \text{const}$, $n_1 = \text{const}$).

For the thin shell case, during the shock crossing phase, shell spreading is important, so that $n_4 \propto r^{-3}$. Since the RS is essentially non-relativistic, one has $\gamma_3 \sim \gamma_4 = \Gamma_0 \sim \text{const}$, $n_3 \sim 4n_4 \propto r^{-3}$. The pressure in Region III is $p_3 \sim p_2 \propto e_2 \sim \text{const}$. The total number of electrons in Region III is $N_{e,3} \propto n_4^{1/2} r^3 \propto r^{3/2} \propto t^{3/2}$. It is convenient to express the evolution of various parameters as a function of the observer-frame time t normalized to the deceleration epoch t_γ . Denoting $t_\gamma = l/2c\Gamma_2^{8/3}$, one has (Kobayashi, 2000)

$$\gamma_3 \sim \Gamma_0 \propto t^0, \quad (8.202)$$

$$n_3 \sim 4n_1 \Gamma_0^2 \left(\frac{t}{t_\gamma} \right)^{-3} \propto t^{-3}, \quad (8.203)$$

$$p_3 \sim p_2 \sim \hat{\gamma} \Gamma_0^2 n_1 m_p c^2 \propto t^0, \quad (8.204)$$

$$N_{e,3} \sim N_{0,4} \left(\frac{t}{t_\gamma} \right)^{3/2} \propto t^{3/2}, \quad (8.205)$$

where

$$N_{0,4} = \frac{E}{\Gamma_0 m_p c^2} \quad (8.206)$$

is the total number of electrons in the shell.

For the thick shell case, the reverse shock becomes relativistic quickly at $R_N \ll R_\Delta$. During the RS-crossing phase, one has $n_4/n_1 = (\gamma_{21}^2 - 1)/(\gamma_{34}^2 - 1)$ (Eq. (4.138)). For a relativistic RS, $\gamma_{21} = \gamma_2 \gg 1$ and $\gamma_{34} \sim (1/2)\gamma_4/\gamma_3 \gg 1$ are satisfied. Noticing $\gamma_4 = \text{const}$, and $\gamma_3 = \gamma_2$, one has $n_4/n_1 \propto \gamma_3^4$. Since for a thick shell spreading is not important, one has $n_4/n_1 \propto n_4 \propto r^{-2}$. One therefore gets $\gamma_3 \propto r^{-1/2} \propto t^{-1/4}$, and consequently $n_3 \propto n_4(\gamma_4/\gamma_3) \propto r^{-3/2} \propto t^{-3/4}$ and $p_3 \sim p_2 \propto \gamma_3^2 \propto t^{-1/2}$. The total number of electrons increases as $N_{e,3} \propto n_3 r^3 \gamma_3 n_4^{-1/2} \propto r^2 \propto t^1$. In more detail, denoting $t = r/2c\gamma_3^2$ and T as the duration of the GRB, one has (Kobayashi, 2000)

$$\gamma_3 \sim \left(\frac{l}{\Delta_0} \right)^{3/8} \left(\frac{4t}{T} \right)^{-1/4}, \quad (8.207)$$

$$n_3 \sim \frac{8\gamma_3^3 n_1}{\Gamma_0} \propto t^{-3/4}, \quad (8.208)$$

$$p_3 \sim \frac{4\gamma_3^2 n_1 m_p c^2}{3} \propto t^{-1/2}, \quad (8.209)$$

$$N_{e,3} \sim N_{0,4} \frac{t}{T}. \quad (8.210)$$

After the reverse shock crossing, the shocked ejecta takes time to adjust to the BM profile. The scaling laws shortly after RS crossing cannot be straightforwardly derived analytically. One needs to apply numerical simulations to derive the scaling laws. In general, one may introduce a parameterized power-law decay behavior $\gamma_3 \propto r^{-g}$ (Mészáros

and Rees, 1999; Kobayashi and Sari, 2000). The dynamical behavior in Region III may then be delineated with the scaling laws:

$$\gamma_3 \propto t^{-g/(1+2g)}, \quad (8.211)$$

$$n_3 \propto t^{-6(3+g)/7(1+2g)}, \quad (8.212)$$

$$e_3 \propto t^{-8(3+g)/7(1+2g)}, \quad (8.213)$$

$$r \propto t^{1/(1+2g)}, N_{e,3} \propto t^0. \quad (8.214)$$

The synchrotron emission from Region III can then be calculated using the same method discussed above.

Kobayashi and Sari (2000) performed numerical simulations for the post RS-crossing dynamics in Region III. For thin shells in the ISM model, they found that $g \sim 2$ adequately describes the dynamical evolution, so that

$$\gamma_3 \propto t^{-2/5}, \quad (8.215)$$

$$n_3 \propto t^{-6/7}, \quad (8.216)$$

$$p_3 \propto t^{-8/7}, \quad (8.217)$$

$$N_{e,3} = \text{const.} \quad (8.218)$$

For thick shells, Kobayashi and Sari (2000) numerically found that post shock crossing, a BM profile can adequately describe the dynamical evolution in Region III. This gives (Kobayashi, 2000)

$$\gamma_3 \propto t^{-7/16}, \quad (8.219)$$

$$n_3 \propto t^{-13/16}, \quad (8.220)$$

$$p_3 \propto t^{-13/12}, \quad (8.221)$$

$$N_{e,3} = \text{const.} \quad (8.222)$$

8.7.2 Lightcurves

Thin Shell Forward Shock Emission

For the thin shell case, the bulk Lorentz factor remains constant during the RS shock crossing phase. One has the following scaling relations.

The bulk Lorentz factor $\Gamma \propto t^0 \propto r^0$. For the FS emission, since $\gamma_{m,f} \propto \Gamma$, $B' \propto \gamma_{m,f} \propto \Gamma$, and $\gamma_{c,f} \propto \Gamma^{-1} t^{-1} B'^{-2} \propto \Gamma^{-3} t^{-1}$, one has

$$v_{m,f} \propto \Gamma \gamma_{m,f}^2 B' \propto \Gamma^4 \propto t^0, \quad (8.223)$$

$$v_{c,f} \propto \Gamma \gamma_{c,f}^2 B' \propto \Gamma^{-4} t^{-2} \propto t^{-2}, \quad (8.224)$$

$$F_{\nu, \max, f} \propto r^3 B' \Gamma \propto r^3 \propto t^3. \quad (8.225)$$

One therefore gets the following scaling laws (the subscript f is dropped for simplicity).

Table 8.4 The temporal decay index α and spectral index β for FS emission in the thin shell RS-crossing phase; $p > 2$ and $\nu_a < \min(\nu_m, \nu_c)$ are adopted. From Gao et al. (2013a)

	β	α	$\alpha(\beta)$
ISM			
slow cooling			
$\nu < \nu_a$	-2	-2	$\alpha = \beta$
$\nu_a < \nu < \nu_m$	$-\frac{1}{3}$	-3	$\alpha = 3\beta$
$\nu_m < \nu < \nu_c$	$\frac{p-1}{2}$	-3	—
$\nu > \nu_c$	$\frac{p}{2}$	-2	—
ISM			
fast cooling			
$\nu < \nu_a$	-2	-1	$\alpha = \frac{\beta}{2}$
$\nu_a < \nu < \nu_c$	$-\frac{1}{3}$	$-\frac{11}{3}$	$\alpha = 11\beta$
$\nu_c < \nu < \nu_m$	$\frac{1}{2}$	-2	$\alpha = -4\beta$
$\nu > \nu_m$	$\frac{p}{2}$	-2	—
Wind			
slow cooling			
$\nu < \nu_a$	-2	-2	$\alpha = \beta$
$\nu_a < \nu < \nu_m$	$-\frac{1}{3}$	$-\frac{1}{3}$	$\alpha = \beta$
$\nu_m < \nu < \nu_c$	$\frac{p-1}{2}$	$\frac{p-1}{2}$	$\alpha = \beta$
$\nu > \nu_c$	$\frac{p}{2}$	$\frac{p-2}{2}$	$\alpha = \beta - 1$
Wind			
fast cooling			
$\nu < \nu_a$	-2	-3	$\alpha = \frac{3\beta}{2}$
$\nu_a < \nu < \nu_c$	$-\frac{1}{3}$	$\frac{1}{3}$	$\alpha = -\beta$
$\nu_c < \nu < \nu_m$	$\frac{1}{2}$	$-\frac{1}{2}$	$\alpha = -\beta$
$\nu > \nu_m$	$\frac{p}{2}$	$\frac{p-2}{2}$	$\alpha = \beta - 1$

For slow cooling:

- $\nu_a < \nu < \nu_m$: $F_\nu = F_{\nu, \max}(\nu/\nu_m)^{1/3} \propto t^3 \nu^{1/3}$;
- $\nu_m < \nu < \nu_c$: $F_\nu = F_{\nu, \max}(\nu/\nu_m)^{-(p-1)/2} \propto t^3 \nu^{-(p-1)/2}$;
- $\nu > \nu_c$: $F_\nu = F_{\nu, \max} \nu_m^{(p-1)/2} \nu_c^{1/2} \nu^{-p/2} \propto t^2 \nu^{-p/2}$.

For fast cooling:

- $\nu_a < \nu < \nu_c$: $F_\nu = F_{\nu, \max}(\nu/\nu_c)^{1/3} \propto t^3 \nu^{1/3} t^{(-2)(-1/3)} \propto t^{11/3} \nu^{1/3}$;
- $\nu_c < \nu < \nu_m$: $F_\nu = F_{\nu, \max}(\nu/\nu_c)^{-1/2} \propto t^3 \nu^{-1/2} t^{(-2)(1/2)} \propto t^2 \nu^{-1/2}$;
- $\nu > \nu_m$: $F_\nu = F_{\nu, \max} \nu_m^{(p-1)/2} \nu_c^{1/2} \nu^{-p/2} \propto t^3 t^{(-2)(1/2)} \nu^{-p/2} \propto t^2 \nu^{-p/2}$.

The resulting α and β values ($p > 2$) for all spectral regimes (including below ν_a) for the FS emission in the thin-shell RS-crossing phase are presented in Table 8.4.

The detailed expressions of the characteristic parameters are (Gao et al., 2013a)

$$\nu_{mf} = (3.1 \times 10^{16} \text{ Hz}) \hat{z}^{-1} \frac{G(p)}{G(2.3)} \Gamma_{0,2}^4 n_{0,0}^{1/2} \epsilon_{e,-1}^2 \epsilon_{B,-2}^{1/2}, \quad (8.226)$$

$$\nu_{cf} = (4.1 \times 10^{16} \text{ Hz}) \hat{z} \Gamma_{0,2}^{-4} n_{0,0}^{-3/2} \epsilon_{B,-2}^{-3/2} t_2^{-2}, \quad (8.227)$$

$$F_{v,\max f} = (1.1 \times 10^4 \text{ } \mu\text{Jy}) \hat{z}^{-2} \Gamma_{0,2}^8 n_{0,0}^{3/2} \epsilon_{B,-2}^{1/2} D_{28}^{-2} t_2^3, \quad (8.228)$$

$$\nu_{af} = (5.7 \times 10^9 \text{ Hz}) \hat{z}^{-8/5} \frac{g^I(p)}{g^I(2.3)} \Gamma_{0,2}^{8/5} n_{0,0}^{4/5} \epsilon_{e,-1}^{-1} \epsilon_{B,-2}^{1/5} t_2^{3/5}, \quad (8.229)$$

$$\nu_{af} < \nu_{mf} < \nu_{cf}, \quad (8.229)$$

$$\nu_{af} = (8.3 \times 10^{12} \text{ Hz}) \hat{z}^{-\frac{p+6}{p+4}} \frac{g^{II}(p)}{g^{II}(2.3)} \Gamma_{0,2}^{\frac{4(p+2)}{p+4}} n_{0,0}^{\frac{p+6}{2(p+4)}} \epsilon_{e,-1}^{\frac{2(p-1)}{p+4}} \epsilon_{B,-2}^{\frac{p+2}{2(p+4)}} t_2^{\frac{2}{p+4}}, \quad (8.230)$$

$$\nu_{mf} < \nu_{af} < \nu_{cf}, \quad (8.230)$$

$$\nu_{af} = (4.9 \times 10^9 \text{ Hz}) \hat{z}^{-13/5} \frac{g^{III}(p)}{g^{III}(2.3)} \Gamma_{0,2}^{28/5} n_{0,0}^{9/5} \epsilon_{B,-2}^{6/5} t_2^{8/5}, \quad (8.231)$$

$$\nu_{af} < \nu_{cf} < \nu_{mf}, \quad (8.231)$$

where

$$g^I(p) = \left(\frac{p-1}{p-2} \right) (p+1)^{3/5} f(p)^{3/5}, \quad (8.232)$$

$$g^{II}(p) = 1.5 \times 10^{-\frac{30}{p+4}} \left(\frac{p-2}{p-1} \right)^{\frac{2(p-1)}{p+4}} (p+1)^{\frac{2}{p+4}} f(p)^{\frac{2}{p+4}}, \quad (8.233)$$

$$g^{III}(p) = (p+1)^{3/5} f(p)^{3/5}, \quad (8.234)$$

and \hat{z} , $f(p)$, and $G(p)$ are defined in Eqs. (8.113), (8.117), and (8.186), respectively.

Thin Shell Reverse Shock Emission

The RS emission includes two phases, pre shock crossing and post shock crossing.

Pre shock crossing, based on the derived physical conditions in Region III (§8.7.1), one can derive the following scaling laws: the bulk Lorentz factor $\Gamma \propto t^0 \propto r^0$. For the RS emission, $\gamma_{m,r} \propto p/n \propto t^3$, $B' \propto p_3 \propto t^0$, and $\gamma_{c,r} \propto \Gamma^{-1} t^{-1} B'^{-2} \propto \Gamma^{-3} t^{-1}$, so that

$$\nu_{m,r} \propto \Gamma \gamma_{m,r}^2 B' \propto t^6, \quad (8.235)$$

$$\nu_{c,r} \propto \Gamma \gamma_{c,r}^2 B' \propto t^{-2}, \quad (8.236)$$

$$F_{v,\max,r} \propto N_e B' \Gamma \propto t^{3/2}. \quad (8.237)$$

One therefore gets the following scaling laws (the subscript r is dropped for simplicity).

For slow cooling:

- $\nu_a < \nu < \nu_m$: $F_\nu = F_{v,\max} (\nu/\nu_m)^{1/3} \propto t^{3/2} \nu^{1/3} t^{-2} \propto t^{-1/2} \nu^{1/3}$;
- $\nu_m < \nu < \nu_c$: $F_\nu = F_{v,\max} (\nu/\nu_m)^{-(p-1)/2} \propto t^{3/2} \nu^{-(p-1)/2} t^{3p-3} \propto t^{(6p-3)/2} \nu^{-(p-1)/2}$;
- $\nu > \nu_c$: $F_\nu = F_{v,\max} \nu_m^{(p-1)/2} \nu_c^{1/2} \nu^{-p/2} \propto t^{3/2} t^{3p-3} t^{-1} \nu^{-p/2} \propto t^{(6p-5)/2} \nu^{-p/2}$.

Table 8.5 Temporal decay index α and spectral index β of RS emission in the thin shell RS-crossing phase; $p > 2$ and $v_a < \min(v_m, v_c)$ are adopted. From Gao et al. (2013a)

	β	α	$\alpha(\beta)$
ISM			
slow cooling			
$v < v_a$	-2	-5	$\alpha = \frac{5\beta}{2}$
$v_a < v < v_m$	$-\frac{1}{3}$	$\frac{1}{2}$	$\alpha = \frac{3\beta}{2}$
$v_m < v < v_c$	$\frac{p-1}{2}$	$-\frac{6p-3}{2}$	$\alpha = -\frac{3(4\beta+1)}{2}$
$v > v_c$	$\frac{p}{2}$	$-\frac{6p-5}{2}$	$-\frac{11\beta+1}{2}$
ISM			
fast cooling			
$v < v_a$	-2	-1	$\alpha = \frac{\beta}{2}$
$v_a < v < v_c$	$-\frac{1}{3}$	$-\frac{13}{6}$	$\alpha = \frac{13\beta}{2}$
$v_c < v < v_m$	$\frac{1}{2}$	$-\frac{1}{2}$	$\alpha = -\beta$
$v > v_m$	$\frac{p}{2}$	$-\frac{6p-5}{2}$	$-\frac{12\beta-5}{2}$
Wind			
slow cooling			
$v < v_a$	-2	-3	$\alpha = \frac{3\beta}{2}$
$v_a < v < v_m$	$-\frac{1}{3}$	$\frac{5}{6}$	$\alpha = \frac{5\beta}{2}$
$v_m < v < v_c$	$\frac{p-1}{2}$	$-\frac{p-2}{2}$	$\alpha = \frac{1-2\beta}{2}$
$v > v_c$	$\frac{p}{2}$	$-\frac{p-1}{2}$	$\alpha = \frac{1-2\beta}{2}$
Wind			
fast cooling			
$v < v_a$	-2	-3	$\alpha = \frac{3\beta}{2}$
$v_a < v < v_c$	$-\frac{1}{3}$	$\frac{5}{6}$	$\alpha = -\frac{5\beta}{2}$
$v_c < v < v_m$	$\frac{1}{2}$	0	$--$
$v > v_m$	$\frac{p}{2}$	$-\frac{p-1}{2}$	$\alpha = \frac{1-2\beta}{2}$

For fast cooling:

- $v_a < v < v_c$: $F_\nu = F_{\nu, \max} (v/v_c)^{1/3} \propto t^{3/2} v^{1/3} t^{-2} \propto t^{-1/2} v^{1/3}$;
- $v_c < v < v_m$: $F_\nu = F_{\nu, \max} (v/v_c)^{-1/2} \propto t^{3/2} v^{-1/2} t^{-1} \propto t^{1/2} v^{-1/2}$;
- $v > v_m$: $F_\nu = F_{\nu, \max} v_m^{(p-1)/2} v_c^{1/2} v^{-p/2} \propto t^{(6p-5)/2} v^{-p/2}$.

The results of α and β values ($p > 2$) for all spectral regimes (including below v_a) for the RS emission in the thin shell RS-crossing phase are presented in Table 8.5 (Exercise 8.9).

The characteristic parameters for RS emission before shock crossing are (Gao et al., 2013a)

$$\nu_{m,r} = (1.9 \times 10^{12} \text{ Hz}) \hat{z}^{-7} \frac{G(p)}{G(2.3)} E_{52}^{-2} \Gamma_{0,2}^{18} n_{0,0}^{5/2} \epsilon_{e,-1}^2 \epsilon_{B,-2}^{1/2} t_2^6, \quad (8.238)$$

$$\nu_{c,r} = (4.1 \times 10^{16} \text{ Hz}) \hat{z} \Gamma_{0,2}^{-4} n_{0,0}^{-3/2} \epsilon_{B,-2}^{-3/2} t_2^{-2}, \quad (8.239)$$

$$F_{\nu, \max, r} = (9.1 \times 10^5 \mu\text{Jy}) \hat{z}^{-1/2} E_{52}^{1/2} \Gamma_{0,2}^5 n_{0,0}^{1/2} \epsilon_{B,-2}^{-2} D_{28}^{-2} t_2^{3/2}, \quad (8.240)$$

$$\nu_{a,r} = (1.0 \times 10^{13} \text{ Hz}) \hat{z}^{23/10} \frac{g^{\text{I}}(p)}{g^{\text{I}}(2.3)} E_{52}^{13/10} \Gamma_{0,2}^{-36/5} n_{0,0}^{-1/2} \epsilon_{e,-1}^{-1} \epsilon_{B,-2}^{1/5} t_2^{-33/10},$$

$$\nu_{a,r} < \nu_{m,r} < \nu_{c,r}, \quad (8.241)$$

$$\nu_{a,r} = (4.7 \times 10^{12} \text{ Hz}) \hat{z}^{\frac{3-7p}{p+4}} \frac{g^{\text{II}}(p)}{g^{\text{II}}(2.3)} E_{52}^{\frac{3-2p}{p+4}} \Gamma_0^{\frac{18p-12}{p+4}} n_{0,0}^{\frac{5p}{2(p+4)}} \epsilon_{e,-1}^{\frac{2(p-1)}{p+4}} \epsilon_{B,-2}^{\frac{p+2}{2(p+4)}} t_2^{\frac{6p-7}{p+4}},$$

$$\nu_{m,r} < \nu_{a,r} < \nu_{c,r}, \quad (8.242)$$

$$\nu_{a,r} = (7.0 \times 10^{10} \text{ Hz}) \hat{z}^{-17/10} \frac{g^{\text{III}}(p)}{g^{\text{III}}(2.3)} E_{52}^{3/10} \Gamma_{0,2}^{19/5} n_{0,0}^{3/2} \epsilon_{B,-2}^{6/5} t_2^{7/10},$$

$$\nu_{a,r} < \nu_{c,r} < \nu_{m,r}, \quad (8.243)$$

where

$$g^{\text{I}}(p) = \left(\frac{p-1}{p-2} \right) (p+1)^{3/5} f(p)^{3/5}, \quad (8.244)$$

$$g^{\text{II}}(p) = 4.1 \times 10^{-\frac{360}{p+4}} \left(\frac{p-2}{p-1} \right)^{\frac{2(p-1)}{p+4}} (p+1)^{\frac{2}{p+4}} f(p)^{\frac{2}{p+4}}, \quad (8.245)$$

$$g^{\text{III}}(p) = (p+1)^{3/5} f(p)^{3/5}, \quad (8.246)$$

and \hat{z} , $f(p)$, and $G(p)$ are defined in Eqs. (8.113), (8.117), and (8.186), respectively.

It is worth mentioning that when $\nu_{a,f} < \nu_{a,r}$, one should use $\nu_{a,f}$ instead of $\nu_{a,r}$ to calculate synchrotron self-absorption in the RS region. This is because the FS is ahead of the RS. In order to have emission from the RS escape, it has to overcome absorption in both the FS and the RS regions (Resmi and Zhang, 2016).

After RS crossing, we use the dynamical evolution characterized as $g \sim 2$ (Kobayashi, 2000; Zou et al., 2005) to calculate the RS lightcurve. One important difference in this phase is that the cooling frequency $\nu_{c,r}$ should be replaced by the so-called cutoff frequency ν_{cut} . This is because, after shock crossing, no new electrons are accelerated. All the electrons in the emission region undergo synchrotron and adiabatic cooling. The maximum electron energy corresponds to ν_{cut} , which is calculated by evolving ν_c by the end of shock crossing through adiabatic expansion (Kobayashi, 2000). Slow cooling is the only option, so that there are only two regimes, i.e. $\nu_a < \nu_m < \nu_{\text{cut}}$ and $\nu_m < \nu_a < \nu_{\text{cut}}$.

The derived α and β values of the RS emission after RS crossing are presented in Table 8.6 (for $p > 2$). The related characteristic parameters are (Gao et al., 2013a)

$$\nu_{m,r} = (8.5 \times 10^{11} \text{ Hz}) \hat{z}^{19/35} \frac{G(p)}{G(2.3)} E_{52}^{18/35} \Gamma_{0,2}^{-74/35} n_{0,0}^{-1/70} \epsilon_{e,-1}^2 \epsilon_{B,-2}^{1/2} t_2^{-54/35}, \quad (8.247)$$

$$\nu_{\text{cut}} = (4.3 \times 10^{16} \text{ Hz}) \hat{z}^{19/35} E_{52}^{-16/105} \Gamma_{0,2}^{-292/105} n_{0,0}^{-283/210} \epsilon_{B,-2}^{-3/2} t_2^{-54/35}, \quad (8.248)$$

$$F_{\nu, \max, r} = (7.0 \times 10^5 \mu\text{Jy}) \hat{z}^{69/35} E_{52}^{139/105} \Gamma_{0,2}^{-167/105} n_{0,0}^{37/210} \epsilon_{B,-2}^{1/2} D_{28}^{-2} t_2^{-34/35}, \quad (8.249)$$

Table 8.6 Temporal decay index α and spectral index β of RS emission in the thin shell regime after RS crossing; $p > 2$ and $\nu_a < \min(\nu_m, \nu_{\text{cut}})$ are adopted. From Gao et al. (2013a)

	β	α	$\alpha(\beta)$
ISM	slow cooling		
$\nu < \nu_a$	-2	$-\frac{18}{35}$	$\alpha = \frac{9\beta}{35}$
$\nu_a < \nu < \nu_m$	$-\frac{1}{3}$	$\frac{16}{35}$	$\alpha = -\frac{16\beta}{105}$
$\nu_m < \nu < \nu_{\text{cut}}$	$\frac{p-1}{2}$	$\frac{27p+7}{35}$	$\alpha = \frac{54\beta+34}{35}$
Wind	slow cooling		
$\nu < \nu_a$	-2	$-\frac{13}{21}$	$\alpha = \frac{13\beta}{42}$
$\nu_a < \nu < \nu_m$	$-\frac{1}{3}$	$\frac{10}{21}$	$\alpha = \frac{10\beta}{7}$
$\nu_m < \nu < \nu_{\text{cut}}$	$\frac{p-1}{2}$	$\frac{39p+7}{42}$	$\alpha = \frac{78\beta+46}{2}$

$$\nu_{a,r} = (1.4 \times 10^{13} \text{ Hz}) \hat{z}^{-73/175} \frac{g^{\text{XV}}(p)}{g^{\text{XV}}(2.3)} E_{52}^{69/175} \Gamma_{0,2}^{8/175} n_{0,0}^{71/175} \times \epsilon_{e,-1}^{-1} \epsilon_{B,-2}^{1/5} t_2^{-102/175}, \quad \nu_{a,r} < \nu_{m,r} < \nu_{c,r}, \quad (8.250)$$

$$\nu_{a,r} = (3.7 \times 10^{12} \text{ Hz}) \hat{z}^{\frac{19p-36}{35(p+4)}} \frac{g^{\text{XVI}}(p)}{g^{\text{XVI}}(2.3)} E_{52}^{\frac{2(9p+29)}{35(p+4)}} \Gamma_{0,2}^{\frac{-74p-44}{35(p+4)}} n_{0,0}^{\frac{94-p}{70(p+4)}} \times \epsilon_{e,-1}^{\frac{2(p-1)}{p+4}} \epsilon_{B,-2}^{\frac{p+2}{2(p+4)} - \frac{54p+104}{35(p+4)}} t_2, \quad \nu_{m,r} < \nu_{a,r} < \nu_{c,r}, \quad (8.251)$$

where

$$g^{\text{XV}}(p) = \left(\frac{p-1}{p-2} \right) (p+1)^{3/5} f(p)^{3/5}, \quad (8.252)$$

$$g^{\text{XVI}}(p) = 8.3 \times 10^{-\frac{22}{p+4}} \left(\frac{p-2}{p-1} \right)^{\frac{2(p-1)}{p+4}} (p+1)^{\frac{2}{p+4}} f(p)^{\frac{2}{p+4}}, \quad (8.253)$$

and \hat{z} and $f(p)$ are defined in Eqs. (8.113) and (8.117), respectively.

Thick Shell Forward Shock Emission

The thick shell can be studied similarly. In contrast to the thin shell case, the RS becomes relativistic early on during shock crossing. During the shock crossing phase, the blastwave Lorentz factor drops with radius as $\Gamma \propto r^{-1/2} \propto t^{-1/4}$, and $r \propto t^{1/2}$.

For the FS, one has $\gamma_{m,f} \propto B' \propto \Gamma \propto t^{-1/4}$, $\gamma_{c,f} \propto \Gamma^{-1} t^{-1} B'^{-2} \propto \Gamma^{-3} t^{-1} \propto t^{-1/4}$, so that

$$\nu_{m,f} \propto \Gamma \gamma_{m,f}^2 B' \propto t^{-1}, \quad (8.254)$$

$$\nu_{c,f} \propto \Gamma \gamma_{c,f}^2 B' \propto t^{-1}, \quad (8.255)$$

$$F_{\nu,\text{max},f} \propto r^3 B' \Gamma \propto t^1. \quad (8.256)$$

Table 8.7 The temporal decay index α and spectral index β of the thick shell forward shock model; $p > 2$ and $v_a < \min(v_m, v_c)$ are adopted. From Gao et al. (2013a)

	β	α	$\alpha(\beta)$
ISM slow cooling			
$v < v_a$	-2	-1	$\alpha = \frac{\beta}{2}$
$v_a < v < v_m$	$-\frac{1}{3}$	$-\frac{4}{3}$	$\alpha = 4\beta$
$v_m < v < v_c$	$\frac{p-1}{2}$	$\frac{p-3}{2}$	$\alpha = \beta - 1$
$v > v_c$	$\frac{p}{2}$	$\frac{p-2}{2}$	$\alpha = \beta - 1$
ISM fast cooling			
$v < v_a$	-2	-1	$\alpha = \frac{\beta}{2}$
$v_a < v < v_c$	$-\frac{1}{3}$	$-\frac{4}{3}$	$\alpha = 4\beta$
$v_c < v < v_m$	$\frac{1}{2}$	$-\frac{1}{2}$	$\alpha = -\beta$
$v > v_m$	$\frac{p}{2}$	$\frac{p-2}{2}$	$\alpha = \beta - 1$
Wind slow cooling			
$v < v_a$	-2	-2	$\alpha = \beta$
$v_a < v < v_m$	$-\frac{1}{3}$	$-\frac{1}{3}$	$\alpha = \beta$
$v_m < v < v_c$	$\frac{p-1}{2}$	$\frac{p-1}{2}$	$\alpha = \beta$
$v > v_c$	$\frac{p}{2}$	$\frac{p-2}{2}$	$\alpha = \beta - 1$
Wind fast cooling			
$v < v_a$	-2	-3	$\alpha = \frac{3\beta}{2}$
$v_a < v < v_c$	$-\frac{1}{3}$	$\frac{1}{3}$	$\alpha = -\beta$
$v_c < v < v_m$	$\frac{1}{2}$	$-\frac{1}{2}$	$\alpha = -\beta$
$v > v_m$	$\frac{p}{2}$	$\frac{p-2}{2}$	$\alpha = \beta - 1$

One can then derive the following scaling laws.

For slow cooling:

- $v_{a,f} < v < v_{m,f}$: $F_v = F_{v,\max}(v/v_m)^{1/3} \propto t^{4/3}v^{1/3}$;
- $v_{m,f} < v < v_{c,f}$: $F_v = F_{v,\max}(v/v_m)^{-(p-1)/2} \propto t^{(3-p)/2}v^{-(p-1)/2}$;
- $v > v_{c,f}$: $F_v = F_{v,\max}v_m^{(p-1)/2}v_c^{1/2}v^{-p/2} \propto t^{(2-p)/2}v^{-p/2}$.

For fast cooling:

- $v_{a,f} < v < v_{c,f}$: $F_v = F_{v,\max}(v/v_c)^{1/3} \propto t^{4/3}v^{1/3}$;
- $v_{c,f} < v < v_{m,f}$: $F_v = F_{v,\max}(v/v_c)^{-1/2} \propto t^{1/2}v^{-1/2}$;
- $v > v_{m,f}$: $F_v = F_{v,\max}v_m^{(p-1)/2}v_c^{1/2}v^{-p/2} \propto t^{(2-p)/2}v^{-p/2}$.

The α and β values and closure relations ($p > 2$) of the FS emission in the thick shell RS-crossing phase are presented in Table 8.7. The detailed characteristic parameters are (Gao et al., 2013a)

$$\nu_{m,f} = (1.0 \times 10^{16} \text{ Hz}) \frac{G(p)}{G(2.3)} E_{52}^{1/2} \Delta_{0,13}^{-1/2} \epsilon_{e,-1}^2 \epsilon_{B,-2}^{1/2} t_2^{-1}, \quad (8.257)$$

$$\nu_{c,f} = (1.2 \times 10^{17} \text{ Hz}) E_{52}^{-1/2} \Delta_{0,13}^{1/2} n_{0,0}^{-1} \epsilon_{B,-2}^{-3/2} t_2^{-1}, \quad (8.258)$$

$$F_{\nu,\max,f} = (1.2 \times 10^3 \text{ } \mu\text{Jy}) \hat{z} E_{52} \Delta_{0,13}^{-1} n_{0,0}^{1/2} \epsilon_{B,-2}^{1/2} D_{28}^{-2}, \quad (8.259)$$

$$\nu_{a,f} = (3.6 \times 10^9 \text{ Hz}) \hat{z}^{-6/5} \frac{g^{\text{I}}(p)}{g^{\text{I}}(2.3)} E_{52}^{1/5} \Delta_{0,13}^{-1/5} n_{0,0}^{3/5} \epsilon_{e,-1}^{-1} \epsilon_{B,-2}^{1/5} t_2^{1/5}, \quad (8.260)$$

$$\nu_{m,f} < \nu_{a,f} < \nu_{c,f},$$

$$\nu_{a,f} = (3.9 \times 10^{12} \text{ Hz}) \hat{z}^{-\frac{4}{p+4}} \frac{g^{\text{II}}(p)}{g^{\text{II}}(2.3)} E_{52}^{\frac{p+2}{2(p+4)}} \Delta_{0,13}^{-\frac{p+2}{2(p+4)}} n_{0,0}^{\frac{2}{p+4}} \epsilon_{e,-1}^{\frac{2(p-1)}{p+4}} \epsilon_{B,-2}^{\frac{p+2}{2(p+4)}} t_2^{-\frac{p}{p+4}}, \quad (8.261)$$

$$\nu_{m,f} < \nu_{a,f} < \nu_{c,f},$$

$$\nu_{a,f} = (1.0 \times 10^9 \text{ Hz}) \hat{z}^{-6/5} \frac{g^{\text{III}}(p)}{g^{\text{III}}(2.3)} E_{52}^{7/10} \Delta_{0,13}^{-7/10} n_{0,0}^{11/10} \epsilon_{B,-2}^{6/5} t_2^{1/5}, \quad (8.262)$$

$$\nu_{a,f} < \nu_{c,f} < \nu_{m,f},$$

where

$$g^{\text{I}}(p) = \left(\frac{p-1}{p-2} \right) (p+1)^{3/5} f(p)^{3/5}, \quad (8.263)$$

$$g^{\text{II}}(p) = 1.4 \times 10^{-\frac{10}{p+4}} \left(\frac{p-1}{p-2} \right)^{\frac{2(1-p)}{p+4}} (p+1)^{\frac{2}{p+4}} f(p)^{\frac{2}{p+4}}, \quad (8.264)$$

$$g^{\text{III}}(p) = (p+1)^{3/5} f(p)^{3/5}, \quad (8.265)$$

and \hat{z} , $f(p)$, and $G(p)$ are defined in Eqs. (8.113), (8.117), and (8.186), respectively.

Thick shell reverse shock emission

Using the thick shell dynamics derived in §8.7.1, i.e. $\gamma_3 = \Gamma \propto t^{-1/4}$, $n_3 \propto \gamma_3^3 \propto t^{-3/4}$, $p_3 \propto t^{-1/2}$, and $N_{e,3} \propto t$, one can derive $\gamma_{m,r} \propto p_3/n_3 \propto t^{1/4}$, $\gamma_{c,r} \propto \Gamma^{-1} t^{-1} B'^{-2} \propto t^{-1/4}$, so that

$$\nu_{m,r} \propto \Gamma \gamma_{m,r}^2 B' \propto t^0 = \text{const}, \quad (8.266)$$

$$\nu_{c,r} \propto \Gamma \gamma_{c,r}^2 B' \propto t^{-1}, \quad (8.267)$$

$$F_{\nu,\max,r} \propto N_{e,3} B' \Gamma \propto t^{1/2}. \quad (8.268)$$

One can then derive the following scaling laws.

For slow cooling:

- $\nu_{a,r} < \nu < \nu_{m,r}$: $F_\nu = F_{\nu,\max}(\nu/\nu_m)^{1/3} \propto t^{1/2} \nu^{1/3}$;

Table 8.8 The temporal decay index α and spectral index β of the thick shell reverse shock model during the shock crossing phase; $p > 2$ and $v_a < \min(v_m, v_c)$ are adopted

	β	α	$\alpha(\beta)$
ISM	slow cooling		
$v < v_a$	-2	$-\frac{3}{2}$	$\alpha = \frac{3\beta}{4}$
$v_a < v < v_m$	$-\frac{1}{3}$	$-\frac{1}{2}$	$\alpha = \frac{3\beta}{2}$
$v_m < v < v_c$	$\frac{p-1}{2}$	$-\frac{1}{2}$	—
$v > v_c$	$\frac{p}{2}$	0	—
ISM	fast cooling		
$v < v_a$	-2	-1	$\alpha = \frac{\beta}{2}$
$v_a < v < v_c$	$-\frac{1}{3}$	$-\frac{5}{6}$	$\alpha = \frac{5\beta}{2}$
$v_c < v < v_m$	$\frac{1}{2}$	0	—
$v > v_m$	$\frac{p}{2}$	0	—
Wind	slow cooling		
$v < v_a$	-2	-2	$\alpha = \beta$
$v_a < v < v_m$	$-\frac{1}{3}$	$-\frac{1}{3}$	$\alpha = \beta$
$v_m < v < v_c$	$\frac{p-1}{2}$	$\frac{p-1}{2}$	$\alpha = \beta$
$v > v_c$	$\frac{p}{2}$	$\frac{p-2}{2}$	$\alpha = \beta - 1$
Wind	fast cooling		
$v < v_a$	-2	-3	$\alpha = \frac{3\beta}{2}$
$v_a < v < v_c$	$-\frac{1}{3}$	$\frac{1}{3}$	$\alpha = -\beta$
$v_c < v < v_m$	$\frac{1}{2}$	$-\frac{1}{2}$	$\alpha = -\beta$
$v > v_m$	$\frac{p}{2}$	$\frac{p-2}{2}$	$\alpha = \beta - 1$

- $v_{m,r} < v < v_{c,r}$: $F_v = F_{v,\max}(v/v_m)^{-(p-1)/2} \propto t^{1/2}v^{-(p-1)/2}$;
- $v > v_{c,r}$: $F_v = F_{v,\max}v_m^{(p-1)/2}v_c^{1/2}v^{-p/2} \propto t^0v^{-p/2}$.

For fast cooling:

- $v_{a,r} < v < v_{c,r}$: $F_v = F_{v,\max}(v/v_c)^{1/3} \propto t^{5/6}v^{1/3}$;
- $v_{c,r} < v < v_{m,r}$: $F_v = F_{v,\max}(v/v_c)^{-1/2} \propto t^0v^{-1/2}$;
- $v > v_{m,r}$: $F_v = F_{v,\max}v_m^{(p-1)/2}v_c^{1/2}v^{-p/2} \propto t^0v^{-p/2}$.

The α and β values and the closure relations ($p > 2$) of the RS emission in the thick shell RS-crossing phase are presented in Table 8.8. The detailed characteristic parameters are (Gao et al., 2013a)

$$v_{m,r} = (7.6 \times 10^{11} \text{ Hz}) \hat{z}^{-1} \frac{G(p)}{G(2.3)} \Gamma_{0,2}^2 n_{0,0}^{1/2} \epsilon_{e,-1}^2 \epsilon_{B,-2}^{1/2}, \quad (8.269)$$

Table 8.9 Temporal decay index α and spectral index β in thin shell reverse shock model after reverse shock crossing in the $\nu_m < \nu_a < \nu_{\text{cut}}$ spectral regime

	β	α	$\alpha(\beta)$
ISM			
slow cooling			
$\nu < \nu_m$	-2	$-\frac{18}{35}$	$\alpha = \frac{9\beta}{35}$
$\nu_m < \nu < \nu_a$	$-\frac{5}{2}$	$-\frac{9}{7}$	$\alpha = \frac{18\beta}{35}$
$\nu_a < \nu < \nu_{\text{cut}}$	$\frac{p-1}{2}$	$\frac{27p+7}{35}$	$\alpha = \frac{54\beta+34}{35}$
Wind			
slow cooling			
$\nu < \nu_m$	-2	$-\frac{13}{21}$	$\alpha = \frac{13\beta}{42}$
$\nu_m < \nu < \nu_a$	$-\frac{5}{2}$	$-\frac{65}{42}$	$\alpha = \frac{13\beta}{24}$
$\nu_a < \nu < \nu_{\text{cut}}$	$\frac{p-1}{2}$	$\frac{39p+7}{42}$	$\alpha = \frac{78\beta+46}{2}$

$$\nu_{c,r} = (1.2 \times 10^{17} \text{ Hz}) E_{52}^{-1/2} \Delta_{0,13}^{1/2} n_{0,0}^{-1} \epsilon_{B,-2}^{-3/2} t_2^{-1}, \quad (8.270)$$

$$F_{\nu,\text{max},r} = (1.3 \times 10^5 \text{ } \mu\text{Jy}) \hat{z}^{1/2} E_{52}^{5/4} \Delta_{0,13}^{-5/4} \Gamma_{0,2}^{-1} n_{0,0}^{1/4} \epsilon_{B,-2}^{1/2} D_{28}^{-2} t_2^{1/2}, \quad (8.271)$$

$$\nu_{a,r} = (7.2 \times 10^{12} \text{ Hz}) \hat{z}^{-2/5} \frac{g^{\text{I}}(p)}{g^{\text{I}}(2.3)} E_{52}^{3/5} \Gamma_{0,2}^{-8/5} \Delta_{0,13}^{-3/5} n_{0,0}^{1/5} \epsilon_{e,-1}^{-1} \epsilon_{B,-2}^{1/5} t_2^{-3/5},$$

$$\nu_{a,r} < \nu_{m,r} < \nu_{c,r}, \quad (8.272)$$

$$\nu_{a,r} = (2.5 \times 10^{12} \text{ Hz}) \hat{z}^{-\frac{p+2}{p+4}} \frac{g^{\text{II}}(p)}{g^{\text{II}}(2.3)} E_{52}^{\frac{2}{p+4}} \Gamma_{0,2}^{\frac{2(p-2)}{p+4}} \Delta_{0,13}^{-\frac{2}{p+4}} n_{0,0}^{\frac{p+2}{2(p+4)}} \\ \times \epsilon_{e,-1}^{\frac{2(p-1)}{p+4}} \epsilon_{B,-2}^{\frac{p+2}{2(p+4)}} t_2^{-\frac{2}{p+4}}, \quad \nu_{m,r} < \nu_{a,r} < \nu_{c,r}, \quad (8.273)$$

$$\nu_{a,r} = (1.8 \times 10^{10} \text{ Hz}) \hat{z}^{-9/10} \frac{g^{\text{III}}(p)}{g^{\text{III}}(2.3)} E_{52}^{17/20} \Gamma_{0,2}^{-3/5} \Delta_{0,13}^{-17/20} n_{0,0}^{19/20} \epsilon_{B,-2}^{6/5} t_2^{-1/10},$$

$$\nu_{a,r} < \nu_{c,r} < \nu_{m,r}, \quad (8.274)$$

where

$$g^{\text{I}}(p) = \left(\frac{p-1}{p-2} \right) (p+1)^{3/5} f(p)^{3/5}, \quad (8.275)$$

$$g^{\text{II}}(p) = 1.0 \times 10^{12} e^{-\frac{66}{p+4}} \left(\frac{p-2}{p-1} \right)^{\frac{2(p-1)}{p+4}} (p+1)^{\frac{2}{p+4}} f(p)^{\frac{2}{p+4}}, \quad (8.276)$$

$$g^{\text{III}}(p) = (p+1)^{3/5} f(p)^{3/5}, \quad (8.277)$$

and \hat{z} , $f(p)$, and $G(p)$ are defined in Eqs. (8.113), (8.117), and (8.186), respectively.

For thick shells, after shock crossing the dynamics are consistent with the BM solution (Kobayashi and Sari, 2000). Using Eqs. (8.219)–(8.222), one can similarly derive α and β values in different spectral regimes (Table 8.9).

The characteristic parameters are (Gao et al., 2013a)

$$\nu_{m,r} = (4.8 \times 10^{12} \text{ Hz}) \hat{z}^{25/48} \frac{G(p)}{G(2.3)} \Gamma_{0,2}^2 \Delta_{0,13}^{73/48} n_{0,0}^{1/2} \epsilon_{e,-1}^{1/2} \epsilon_{B,-2}^{1/2} t_2^{-73/48}, \quad (8.278)$$

$$\nu_{\text{cut}} = (2.3 \times 10^{17} \text{ Hz}) \hat{z}^{25/48} E_{52}^{-1/2} \Delta_{0,13}^{49/48} n_{0,0}^{-1} \epsilon_{B,-2}^{-3/2} t_2^{-73/48}, \quad (8.279)$$

$$F_{\nu,\text{max},r} = (7.9 \times 10^5 \text{ } \mu\text{Jy}) \hat{z}^{95/48} E_{52}^{5/4} \Gamma_{0,2}^{-1} \Delta_{0,13}^{11/48} n_{0,0}^{1/4} \epsilon_{B,-2}^{1/2} D_{28}^{-2} t_2^{-47/48}, \quad (8.280)$$

$$\nu_{a,r} = (6.6 \times 10^{12} \text{ Hz}) \hat{z}^{-7/15} \frac{g^{\text{XV}}(p)}{g^{\text{XV}}(2.3)} E_{52}^{3/5} \Gamma_{0,2}^{-8/5} \Delta_{0,13}^{-2/3} n_{0,0}^{1/5} \epsilon_{e,-1}^{-1} \epsilon_{B,-2}^{1/5} t_2^{-8/15},$$

$$\nu_{a,r} < \nu_{m,r} < \nu_{\text{cut}}, \quad (8.281)$$

$$\nu_{a,r} = (5.7 \times 10^{12} \text{ Hz}) \hat{z}^{\frac{25p-58}{48(p+4)}} \frac{g^{\text{XVI}}(p)}{g^{\text{XVI}}(2.3)} E_{52}^{\frac{2}{p+4}} \Gamma_{0,2}^{\frac{2(p-2)}{p+4}} \Delta_{0,13}^{\frac{73p-58}{48(p+4)}} n_{0,0}^{\frac{p+2}{2(p+4)}} \\ \times \epsilon_{e,-1}^{\frac{2(p-1)}{p+4}} \epsilon_{B,-2}^{\frac{p+2}{2(p+4)}} t_2^{-\frac{73p+134}{48(p+4)}}, \quad \nu_{m,r} < \nu_{a,r} < \nu_{\text{cut}}, \quad (8.282)$$

where

$$g^{\text{XV}}(p) = 4.29 \times 10^{21} \left(\frac{p-1}{p-2} \right) (p+1)^{3/5} f(p)^{3/5}, \quad (8.283)$$

$$g^{\text{XVI}}(p) = 5.2 \times 10^{-12} e^{\frac{253}{p+4}} \left(\frac{p-2}{p-1} \right)^{\frac{2(p-1)}{p+4}} (p+1)^{\frac{2}{p+4}} f(p)^{\frac{2}{p+4}}, \quad (8.284)$$

and \hat{z} , $f(p)$, and $G(p)$ are defined in Eqs. (8.113), (8.117), and (8.186), respectively.

Reverse shock lightcurve summary

There are more variations in the RS lightcurves than in the FS lightcurves, owing to more variations in the shock crossing dynamics (thin vs. thick shells, pre and post shock crossing). Considering the variations of the spectral regimes and whether $p > 2$ or $1 < p < 2$, depending on the observing frequency, there are many possible lightcurves. A detailed discussion has been presented in Gao et al. (2013a). These are for synchrotron radiation only. Considering SSC in the RS and the cross Compton scattering between photons and electrons in the RS and FS, there are a lot more variations (Wang et al., 2001a,b; Dai, 2004; Kobayashi et al., 2007; Wang et al., 2016b).

Nonetheless, for typical parameters and considering typical observational bands, the dynamical and spectral regimes of the RS emission are narrowed down, so that a simplified discussion may be presented.

A starting point of discussion is to notice the end of the RS-crossing phase. Since the internal energy and pressure in Regions II and III are essentially the same, and since the density in Region III (n_3) is of the order γ_3 times that in Region II (n_2), electrons in the RS region carry a much smaller energy (by a factor of $1/\gamma_3$) than those in the FS region. As a result, the typical synchrotron frequency of the RS is systematically lower than that of the FS. Whereas during the early deceleration phase the FS emission peaks in X-rays or even soft γ -rays, the RS emission actually peaks in IR/optical/UV. The relevant observational

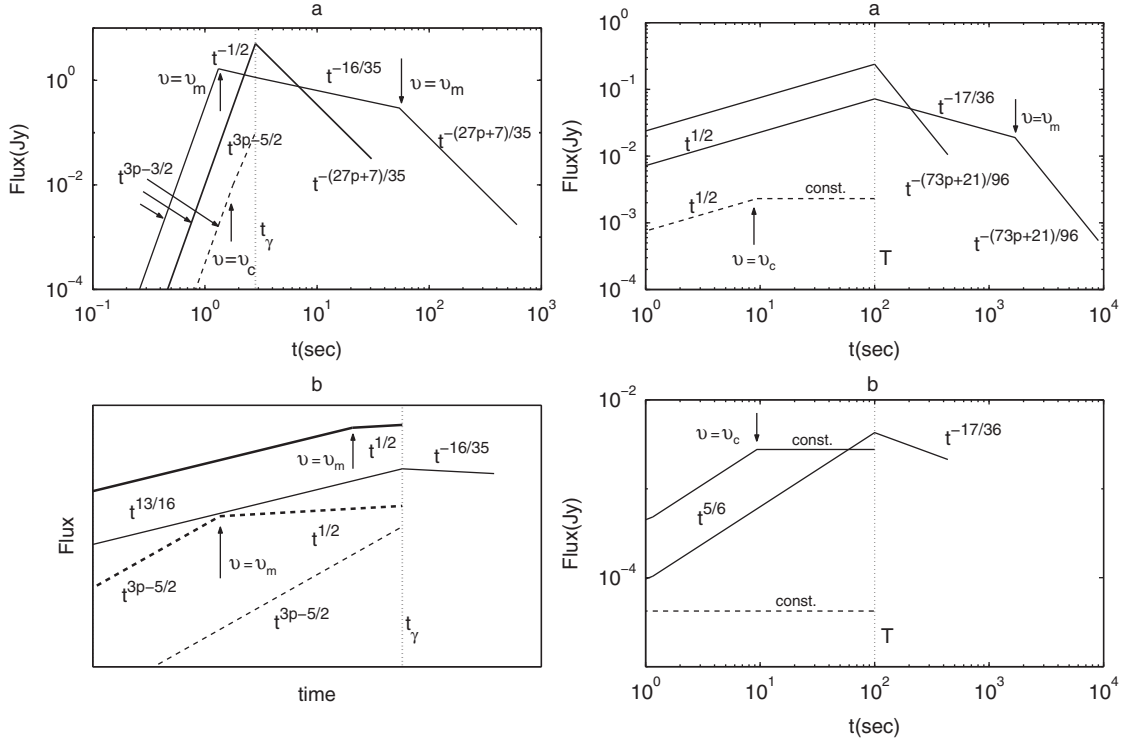


Figure 8.11

Reverse shock model lightcurves. *Left*: thin shell case; *Right*: thick shell case. Reproduced from Figures 2 & 3 in Kobayashi (2000) with permission. ©AAS.

bands for RS emission are therefore IR/optical or even lower frequencies in millimeter and radio.

In the IR/optical/UV bands, synchrotron self-absorption is not important. Various RS lightcurves have been studied in detail by Kobayashi (2000). The key results can be summarized as follows (see Fig. 8.11).

For thick shells, the afterglow initially rises as $F_\nu \propto t^{1/2}$ until $\min(t_c, T)$, where t_c is the time when v_c crosses the observing band. If $t_c < T$ (fast cooling), one has $F_\nu \propto t^0$ when $t_c < t < T$. After the RS crossing, the lightcurve decays as $F_\nu \propto t^{-17/36}$ initially. For slow cooling, it breaks to $F_\nu \propto t^{-(73p+21)/96} \sim t^{-1.9}$ when v_m crosses the band (slow cooling), and breaks to $F_\nu \propto t^{-p-2} \sim t^{-3.2}$ when v_c crosses the band (curvature effect).

For thin shells (and slow cooling), one important parameter

$$\mathcal{R}_\nu \equiv \frac{v_{\text{obs}}}{v_{m,r}(t_\times)} \quad (8.285)$$

defines the shape of the lightcurves, where t_\times is the shock crossing time.

- $\mathcal{R}_\nu > 1$:

The RS afterglow lightcurve has a very steep rise early on, i.e. $\propto t^{3p-5/2}$. The rising slope is 4.1 for $p = 2.2$, and 5 for $p = 2.5$, since v_{obs} is already above $v_{m,r}$ at shock

crossing time t_\times . After the peak time, the afterglow decays as $\sim t^{-(3p+1)/4}$, which is -1.9 for $p = 2.2$, and -2.1 for $p = 2.5$.

- $\mathcal{R}_v < 1$:

The afterglow rises as $t^{3p-3/2}$, and breaks to $t^{-1/2}$ at t_m and extends to t_\times . The early rising slope is 5.1 for $p = 2.2$, and 6 for $p = 2.5$, again a very steep rise.

At the shock crossing, v_{obs} is below $v_{m,r}$ at t_\times . The decay behavior is initially $t^{-16/35}$, and then breaks to $t^{-(3p+1)/4}$ after v_m crosses the band. In this case, the RS peak is not at t_\times , but at t_m during the shock crossing phase (v_m increases with time).

It is worth emphasizing that a characteristic signature of RS emission in the optical band is a $\sim t^{-2}$ decay. This can be roughly derived as follows.

For both the thin and thick shell cases, after RS crossing, one can approximately write (Zhang et al., 2003a)

$$v_{m,r} \propto t^{-3/2}, \quad F_{v,\text{max},r} \propto t^{-1}. \quad (8.286)$$

In the optical band, after shock crossing, usually one has $v_{m,r} < \nu < \nu_{\text{cut}}$, so that

$$F_\nu = F_{v,\text{max},r} \left(\frac{\nu}{v_{m,r}} \right)^{-(p-1)/2} \propto \nu^{-(p-1)/2} t^{-(3p+1)/4}. \quad (8.287)$$

The decay slope $-(3p+1)/4$ is -1.8 to -2.1 for p in the range 2–2.5.

In the radio band, self-absorption becomes important. The lightcurve shapes depend on the relative orderings among $v_{a,r}$, $v_{m,r}$, and $\nu_{c,r}$ (Gao et al., 2013a). A detailed study on the self-absorbed RS radio emission is presented in Resmi and Zhang (2016).

8.7.3 FS vs. RS Lightcurves

The FS and RS emissions are not independent. At the shock crossing time

$$t_\times = \max(t_\gamma, T), \quad (8.288)$$

there are some simple relations between FS and RS characteristic emission properties. Through these relations, the FS and RS emission can be studied coherently.

FS vs. RS Relations at t_\times

The following rough relations between the characteristic parameters exist for the FS and RS emissions at the shock crossing time t_\times (Kobayashi and Zhang, 2003b; Zhang et al., 2003a):

$$\gamma_2 = \gamma_3 = \gamma_\times, \quad (8.289)$$

$$e_2 \simeq e_3, \quad (8.290)$$

$$p_2 \simeq p_3, \quad (8.291)$$

$$M_3 \simeq \gamma_\times M_2 \quad \text{or} \quad N_3 \simeq \gamma_\times N_2. \quad (8.292)$$

From

$$\gamma_{m,f}(t_\times) = \gamma_{m,2} = (\gamma_2 - 1)g(p_f)\epsilon_{ef} \frac{m_p}{m_e}, \quad (8.293)$$

$$\gamma_{m,r}(t_\times) = \gamma_{m,3} = (\gamma_{34} - 1)g(p_r)\epsilon_{e,r} \frac{m_p}{m_e}, \quad (8.294)$$

one has

$$\frac{\gamma_{m,r}(t_\times)}{\gamma_{m,f}(t_\times)} = \frac{\gamma_{34} - 1}{\gamma_\times - 1} \mathcal{R}_e \mathcal{R}_p \simeq \frac{\gamma_{34} - 1}{\gamma_\times} \mathcal{R}_e \mathcal{R}_p, \quad (8.295)$$

where

$$\mathcal{R}_e \equiv \frac{\epsilon_{e,r}}{\epsilon_{ef}}, \quad (8.296)$$

$$\mathcal{R}_p \equiv \frac{g(p_r)}{g(p_f)}. \quad (8.297)$$

From

$$\frac{B'_2{}^2}{8\pi} = \epsilon_{B,f} e_2, \quad (8.298)$$

$$\frac{B'_3{}^2}{8\pi} = \epsilon_{B,r} e_3, \quad (8.299)$$

one can define

$$\mathcal{R}_B \equiv \frac{B'_r}{B'_f} = \left(\frac{\epsilon_{B,r}}{\epsilon_{B,f}} \right)^{1/2}. \quad (8.300)$$

With these preparations, one can write down the following relations (Zhang et al., 2003a):

$$\frac{F_{v,\max,r}(t_\times)}{F_{v,\max,f}(t_\times)} = \frac{N_2 B'_2 \gamma_2}{N_3 B'_3 \gamma_3} \simeq \gamma_\times \mathcal{R}_B, \quad (8.301)$$

$$\frac{v_{m,r}(t_\times)}{v_{m,f}(t_\times)} = \frac{\gamma_2 \gamma_{m,f}^2 B'_2}{\gamma_3 \gamma_{m,r}^2 B'_3} \simeq \left(\frac{\gamma_{34} - 1}{\gamma_\times} \right)^2 \mathcal{R}_B \mathcal{R}_e^2 \mathcal{R}_p^2, \quad (8.302)$$

$$\frac{v_{c,r}(t_\times)}{v_{c,f}(t_\times)} = \frac{\gamma_2^{-1} t_\times^{-2} B'_2{}^{-3}}{\gamma_3^{-1} t_\times^{-2} B'_3{}^{-3}} = \mathcal{R}_B^{-3}. \quad (8.303)$$

Equations (8.301)–(8.303) are useful relations to calculate the RS lightcurves based on the FS lightcurves (which are easy to calculate). As long as the spectral regime of the FS emission is settled at the shock crossing time, that of the RS emission is also settled. One can then calculate the RS lightcurve before t_\times based on the flux value at t_\times and the RS scaling laws.

Owing to the lack of first-principle understanding of relativistic shocks, in principle \mathcal{R}_e , \mathcal{R}_p , and \mathcal{R}_B can differ from unity. This is particularly relevant for \mathcal{R}_B , since the central engine wind is very likely more magnetized than the circumburst medium, so that the RS should have a larger ϵ_B value than the FS, and hence \mathcal{R}_B should be greater than

unity. Indeed, analyzing early optical data of a good fraction of GRBs showed evidence of $\mathcal{R}_B > 1$ (Fan et al., 2002; Zhang et al., 2003a; Kumar and Panaitescu, 2003; Gomboc et al., 2008; Harrison and Kobayashi, 2013; Gao et al., 2015a).

Four Types of Lightcurves in the Optical Band

In the optical band, under certain conditions, the RS emission can outshine the FS emission and give an observable signature. In the case that both RS and FS are observable, Zhang et al. (2003a) suggested that there are two types of lightcurves, the re-brightening type (Type I) and the flattening type (Type II). Later observations (e.g. Molinari et al., 2007) showed that, besides these types, some GRBs do not show the existence of the RS. For FS-only GRBs, there are two additional types (Jin and Fan, 2007; Gao et al., 2015a). Figure 8.12 shows the example model lightcurves of the four types, which we describe below.

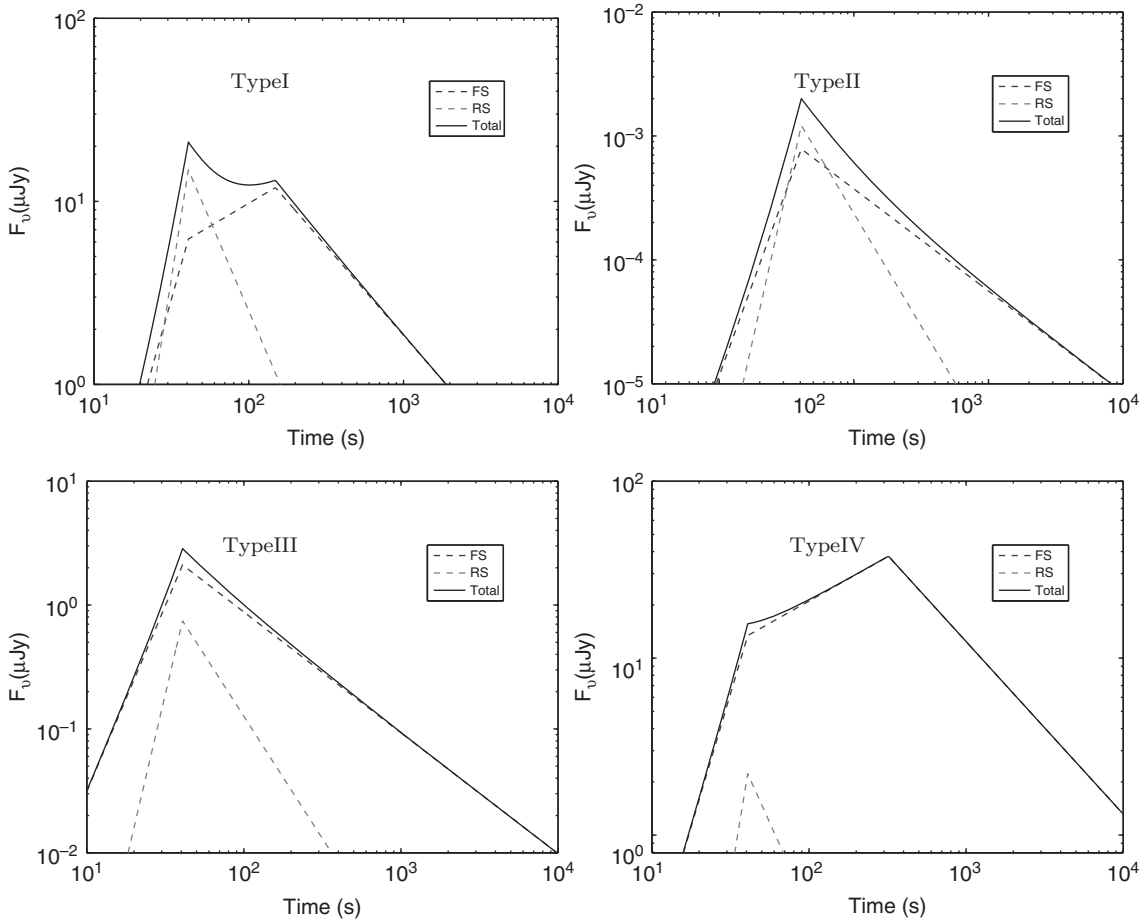


Figure 8.12 Four types of early optical lightcurves. The dashed broad and narrow components are the emission from the FS and RS, respectively. The solid curves are the total emission lightcurves. Type I and II: RS and FS co-exist (Zhang et al., 2003a); Type III and IV: only the FS emission is observable. From Gao et al. (2015a).

- Type I: the re-brightening case. Initially the lightcurve is dominated by the RS emission characterized by an initial rise and a rapid decay. The FS takes over during its rising phase ($\nu < \nu_{m,f}$), and later enters a decay phase after $\nu_{m,f}$ crosses the optical band. The lightcurve therefore shows a double-peak signature. For typical shock microphysics parameters and for the simplest assumption of $\mathcal{R}_\nu \geq 1$, $\mathcal{R}_e \sim 1$, $\mathcal{R}_p \sim 1$, and most importantly $\mathcal{R}_B \sim 1$ (i.e. the RS and FS have similar microphysics parameters), the optical lightcurves should be of this type.
- Type II: the flattening case. The lightcurve initially is also dominated by the RS emission and later transitions to the FS emission. However, $\nu_{m,f}$ is already below ν when the FS takes over. The lightcurve therefore shows a characteristic $\sim t^{-2}$ to $\sim t^{-1}$ transition, as seen in GRB 990123 (Akerlof et al., 1999) and many other GRBs. In order to produce this type of lightcurves, one usually requires $\mathcal{R}_B \gg 1$ (Zhang et al., 2003a). This suggests a magnetized central engine and ejecta outflow. The ejecta carries a stronger magnetic field than the FS so that the RS synchrotron emission is greatly enhanced. However, the magnetic field in the RS region is dynamically unimportant ($\sigma < 1$), so that the RS is not suppressed. A more general discussion on magnetized RS is presented below in §8.7.4.
- Types III and IV: no RS component observed. This may suggest that $\nu_{m,r} \ll \nu$ at the shock crossing time (so that the RS peaks at lower frequencies), or that the RS is suppressed since $\sigma \gg 1$ ($\gamma_{34} - 1 \ll 1$ or $= 0$ for a Poynting-flux-dominated flow). Type III has the optical peak time at the deceleration time (i.e. $\nu > \nu_{m,f}$ at t_\times), while Type IV has $\nu < \nu_{m,f}$ satisfied at $t = t_\times$, so that the optical peak time is delayed to the epoch when $\nu_{m,f}$ crosses the optical band.

8.7.4 Arbitrarily Magnetized Reverse Shock

The RS emission of an arbitrarily magnetized RS has been studied in detail (Zhang and Kobayashi, 2005). The general picture is the following: When σ increases from below, the RS emission initially strengthens due to the increased synchrotron radiation in a progressively stronger magnetic field, and then weakens as σ exceeds unity until completely suppressed as the FS pressure does not exceed the magnetic pressure in the ejecta. The most optimistic case for RS emission is $\sigma \sim 0.1$ – 1 , at which synchrotron emission is greatly strengthened yet the RS is not weakened by the field.

The general shock jump condition for an arbitrarily magnetized shock has been presented in §4.3.2. In the system of an ejecta (Region IV) with magnetization parameter σ decelerated by a constant density medium (Region I), the general relation $n_4/n_1 = (\gamma_{21}^2 - 1)/(\gamma_{34}^2 - 1)$ is modified as

$$F \frac{n_4}{n_1} = \frac{\gamma_{21}^2 - 1}{\gamma_{34}^2 - 1}, \quad (8.304)$$

where $F = f_a f_b f_c$, and f_a , f_b , and f_c are defined in Eqs. (4.143), (4.144), and (4.146), respectively. The introduction of this correction is to modify the characteristic radii R_γ , R_N , and R_Δ in the non-magnetized case, so that (Zhang and Kobayashi, 2005)

$$\frac{R_N}{\xi} = Q^{1/2} R_\gamma = \xi^{1/2} Q^{3/4} R_\Delta = \xi_0^2 R_s, \quad (8.305)$$

where

$$\xi_0 \equiv \frac{(l/\Delta_0)^{1/2}}{\gamma_4^{4/3}} = \left(\frac{t_\gamma}{T} \right)^{1/2}, \quad (8.306)$$

$$\xi \equiv \frac{(l/\Delta)^{1/2}}{\gamma_4^{4/3}}, \quad (8.307)$$

$$Q(\sigma) = (1 + \sigma)^{2/3}. \quad (8.308)$$

An important consequence is that the RS crosses a magnetized shell more rapidly (R_γ smaller by a factor $(1 + \sigma)^{-1/3}$ since only a fraction $(1 + \sigma)$ of the energy is in the baryonic form). This rapid RS-crossing phase was also revealed numerically by Mimica et al. (2009) and Mizuno et al. (2009). Beyond this radius the magnetized ejecta starts to decelerate (but not with full capacity since most of the energy is still in the ejecta). The question is, when would the full ejecta energy be transferred to the medium after which the outflow decelerates as a constant energy fireball? Zhang and Kobayashi (2005) did not address this and left the full deceleration time as unspecified. Later calculations (e.g. Granot, 2012) suggested that the dynamical law of deceleration is $\Gamma \propto r^{-1/2} \propto t^{-1/4}$, which is similar to a “thick shell”. This phase ends as the full energy is converted to the medium, and the blastwave then enters the BM regime with a constant energy. Notice that this phase of transferring the Poynting flux energy to the ambient medium effectively serves as a mechanism of continuous energy injection into the blastwave, which was suggested by Zhang et al. (2006) as the third energy injection mechanism (besides the long-lasting central engine and the stratified ejecta Lorentz factor) for interpreting the shallow decay phase of the early X-ray afterglows of many GRBs.

As σ increases, $\gamma_{34} - 1$ progressively drops and approaches 0, making the RS progressively weaker. The disappearance of RS occurs at (Zhang and Kobayashi, 2005)

$$\sigma > \sigma_c \equiv \frac{8}{3} \gamma_4^2 \frac{n_1}{n_4}, \quad (8.309)$$

when the FS pressure becomes smaller than the magnetic pressure in Region IV. Usually this is at $\sigma > 1$. In contrast to some claims, $\sigma > 1$ is not the condition to suppress a RS.

Considering RS emission, there is another important factor in deciding whether significant RS emission is possible. As shown by Sironi and Spitkovsky (2009a), particle acceleration starts to be suppressed for relativistic shocks when σ becomes higher than 10^{-3} . Since the RS is trans-relativistic, the characteristic σ above which particle acceleration is suppressed would be higher. Nonetheless, this effect serves as an additional mechanism against strong RS emission when $\sigma > 1$. According to the RS observations, it seems that the most efficient RS emission is achieved at $\sigma \sim (0.1-1)$.

8.7.5 Wind Model

The RS model in a wind environment has been extensively studied by Wu et al. (2003), Kobayashi and Zhang (2003a), Kobayashi et al. (2004), Zou et al. (2005), and Gao et al. (2013a).

Dynamics

A similar analysis of characteristic radii in the wind model can be made similarly to the ISM case (Kobayashi and Zhang, 2003a). One important difference from the ISM model is that both n_4 and n_1 have the same scaling $\propto r^{-2}$, so that n_4/n_1 is constant (instead of an r -dependent parameter in the ISM case). As a result, the RS is either relativistic or non-relativistic throughout the shock crossing process (except that it would turn to trans-relativistic when spreading is considered in the thin shell case). One therefore only has three relevant radii (R_N is not relevant):

$$R_\Gamma = \frac{E}{4\pi A c^2 \Gamma_0^2}, \quad (8.310)$$

$$R_s = \Delta_0 \Gamma_0^2, \quad (8.311)$$

$$R_\times = R_\Delta \simeq \max((R_s R_\Gamma)^{1/2}, R_\Gamma), \quad (8.312)$$

where the former expression in R_\times is relevant for the thick shell $R_\Gamma < R_s$ for which $\Delta \simeq \Delta_0$, and the latter is relevant for $R_\Gamma > R_s$ for which $\Delta \simeq r/\Gamma_0^2$.

A critical parameter for defining whether the RS is relativistic is $\gamma_4^2/(n_4/n_1)$, which in the wind model is $\max(R_s/R_\Gamma, r/R_\Gamma)$. Letting it be unity, one can define a critical initial Lorentz factor

$$\Gamma_{0,c} \equiv \left(\frac{E}{4\pi A c^2 \Delta_0} \right)^{1/4}. \quad (8.313)$$

The thick shell case corresponds to $\Gamma_0 > \Gamma_{0,c}$, and the thin shell case corresponds to $\Gamma_0 < \Gamma_{0,c}$. Putting both regimes together, the Lorentz factor of the blastwave at shock crossing time t_\times is

$$\Gamma_\times = \min(\Gamma_0, \Gamma_{0,c}), \quad (8.314)$$

where the shock crossing time (in the observer frame) is

$$t_\times \simeq (1+z) \frac{R_\times}{c\gamma_\times^2}. \quad (8.315)$$

Similar to the ISM case, one can derive the scaling laws of the characteristic parameters (Exercise 8.10): $e_3 \propto t^{-2}$, $n_3 \propto t^{-2}$, $N_{e,3} \propto t$ for thick shell, and $e_3 \propto t^{-2}$, $n_3 \propto t^{-2}$, $N_{e,3} \propto t^{1/2}$ for thin shell. Before shock crossing, $t < t_\times$, one has $v_{m,r} \propto t^{-1}$, $v_{c,r} \propto t$, and $F_{\nu,\max,r} \propto t^0$ for thick shell, and $v_{m,r} \propto t$, $v_{c,r} \propto t$, and $F_{\nu,\max,r} \propto t^{-1/2}$ for thin shell. Due to the high density of a wind medium, the thick shell case is more common for the wind model.

After shock crossing, the ejecta again takes time to adjust to the BM profile. Similar to the ISM model, the general description invokes a parameter g , which is defined as $\gamma_3 \propto r^{-g}$ (Mészáros and Rees, 1999; Kobayashi and Sari, 2000). For thick shell, after shock crossing, a BM solution adequately describes the profile. However, for thin shell, g has to be solved numerically. An unpublished result by Shiho Kobayashi suggests that $g \sim 0.7$ best describes the result. Zou et al. (2005) presented the expressions with an arbitrary g parameter, and suggested $g \sim 1$ as the approximate value for the post-shock-crossing thin shell model.

The pre- and post-shock-crossing lightcurves can be derived similarly for the wind model. Details have been presented in Zou et al. (2005) and Gao et al. (2013a). The α and β values of all the relevant models for pre- and post-shock-crossing phases for $p > 2$ have been presented in Tables 8.4–8.9. The cases of $1 < p < 2$ are also presented in Gao et al. (2013a).

There is one important spectral regime that is worth mentioning. For a thick wind, in certain parameter regimes, the RS emission enters the “strong self-absorption” regime, i.e. $\nu_{a,r} > \nu_{c,r}$ (§5.1.7). In this regime, strong synchrotron heating would lead to a pile-up of electrons near the self-absorption frequency, leading to a bump feature in the spectrum. Such a feature has been studied by Kobayashi et al. (2004) and Gao et al. (2013c).

For completeness, we present the detailed characteristic parameters of the RS wind model ($p > 2$) following Gao et al. (2013a).

Characteristic Parameters: Thin Shells

For thin shells, during the shock crossing phase ($t < t_\times$), one has for FS emission

$$\nu_{mf} = (8.7 \times 10^{16} \text{ Hz}) \frac{G(p)}{G(2.3)} A_{*, -1}^{1/2} \Gamma_{0,2}^2 \epsilon_{e,-1}^2 \epsilon_{B,-2}^{1/2} t_2^{-1}, \quad (8.316)$$

$$\nu_{cf} = (1.8 \times 10^{15} \text{ Hz}) \hat{z}^{-2} \Gamma_{0,2}^2 A_{*, -1}^{-3/2} \epsilon_{B,-2}^{-3/2} t_2, \quad (8.317)$$

$$F_{\nu, \max f} = (7.5 \times 10^5 \text{ } \mu\text{Jy}) \hat{z} A_{*, -1}^{3/2} \Gamma_{0,2}^2 \epsilon_{B,-2}^{1/2} D_{28}^{-2}, \quad (8.318)$$

$$\nu_{af} = (5.9 \times 10^{10} \text{ Hz}) \frac{g^{\text{VIII}}(p)}{g^{\text{VIII}}(2.3)} \Gamma_{0,2}^{-8/5} A_{*, -1}^{4/5} \epsilon_{e,-1}^{-1} \epsilon_{B,-2}^{1/5} t_2^{-1},$$

$$\nu_{af} < \nu_{mf} < \nu_{cf}, \quad (8.319)$$

$$\nu_{af} = (4.7 \times 10^{13} \text{ Hz}) \frac{g^{\text{IX}}(p)}{g^{\text{IX}}(2.3)} \Gamma_{0,2}^{2(p-2)/(p+4)} A_{*, -1}^{p+6/(p+4)} \epsilon_{e,-1}^{2(p-1)/(p+4)} \epsilon_{B,-2}^{p+2/(p+4)} t_2^{-1},$$

$$\nu_{af} < \nu_{mf} < \nu_{cf}, \quad (8.320)$$

$$\nu_{af} = (4.1 \times 10^{11} \text{ Hz}) \hat{z} \frac{g^{\text{X}}(p)}{g^{\text{X}}(2.3)} \Gamma_{0,2}^{-8/5} A_{*, -1}^{9/5} \epsilon_{B,-2}^{6/5} t_2^{-2},$$

$$\nu_{af} < \nu_{cf} < \nu_{mf}, \quad (8.321)$$

where

$$g^{\text{VIII}}(p) = \left(\frac{p-1}{p-2} \right) (p+1)^{3/5} f(p)^{3/5}, \quad (8.322)$$

$$g^{\text{IX}}(p) = 4.0 \times 10^{-16/p+4} \left(\frac{p-2}{p-1} \right)^{2(p-1)/(p+4)} (p+1)^{2/p+4} f(p)^{2/p+4}, \quad (8.323)$$

$$g^{\text{X}}(p) = (p+1)^{3/5} f(p)^{3/5}, \quad (8.324)$$

and $\hat{z}, f(p)$, and $G(p)$ are defined in Eqs. (8.113), (8.117), and (8.186), respectively.

For RS emission, one has

$$\nu_{m,r} = (3.3 \times 10^{15} \text{ Hz}) \hat{z}^{-2} \frac{G(p)}{G(2.3)} E_{52}^{-2} A_{*, -1}^{5/2} \Gamma_{0,2}^8 \epsilon_{e,-1}^2 \epsilon_{B,-2}^{1/2} t_2, \quad (8.325)$$

$$\nu_{c,r} = (1.8 \times 10^{15} \text{ Hz}) \hat{z}^{-2} \Gamma_{0,2}^2 A_{*, -1}^{-3/2} \epsilon_{B,-2}^{-3/2} t_2, \quad (8.326)$$

$$F_{\nu, \max, r} = (1.3 \times 10^7 \text{ } \mu\text{Jy}) \hat{z}^{3/2} E_{52}^{1/2} A_{*, -1} \Gamma_{0,2}^{1/2} \epsilon_{B,-2}^{-2} D_{28}^{-2} t_2^{-1/2}, \quad (8.327)$$

$$\nu_{a,r} = (1.7 \times 10^{12} \text{ Hz}) \hat{z}^{13/10} \frac{g^{\text{VIII}}(p)}{g^{\text{VIII}}(2.3)} E_{52}^{13/10} \Gamma_{0,2}^{-26/5} A_{*, -1}^{-1/2} \epsilon_{e,-1}^{-1} \epsilon_{B,-2}^{1/5} t_2^{-23/10},$$

$$\nu_{a,r} < \nu_{m,r} < \nu_{c,r}, \quad (8.328)$$

$$\nu_{a,r} = (5.9 \times 10^{13} \text{ Hz}) \hat{z}^{\frac{3-2p}{p+4}} \frac{g^{\text{IX}}(p)}{g^{\text{IX}}(2.3)} E_{52}^{\frac{3-2p}{p+4}} \Gamma_{0,2}^{\frac{8p-12}{p+4}} A_{*, -1}^{\frac{5p}{2(p+4)}} \epsilon_{e,-1}^{\frac{2(p-1)}{p+4}} \epsilon_{B,-2}^{\frac{p+2}{2(p+4)}} t_2^{\frac{p-7}{p+4}},$$

$$\nu_{m,r} < \nu_{a,r} < \nu_{c,r}, \quad (8.329)$$

$$\nu_{a,r} = (2.3 \times 10^{12} \text{ Hz}) \hat{z}^{13/10} \frac{g^{\text{X}}(p)}{g^{\text{X}}(2.3)} E_{52}^{3/10} \Gamma_{0,2}^{-11/5} A_{*, -1}^{3/2} \epsilon_{B,-2}^{6/5} t_2^{-23/10},$$

$$\nu_{a,r} < \nu_{c,r} < \nu_{m,r}, \quad (8.330)$$

where

$$g^{\text{VIII}}(p) = \left(\frac{p-1}{p-2} \right) (p+1)^{3/5} f(p)^{3/5}, \quad (8.331)$$

$$g^{\text{IX}}(p) = 1.3 \times 10^{-\frac{486}{p+4}} 3^{-\frac{25}{p+4}} \pi^{-\frac{9}{p+4}} \left(\frac{p-2}{p-1} \right)^{\frac{2(p-1)}{p+4}} (p+1)^{\frac{2}{p+4}} f(p)^{\frac{2}{p+4}}, \quad (8.332)$$

$$g^{\text{X}}(p) = (p+1)^{3/5} f(p)^{3/5}, \quad (8.333)$$

and \hat{z} , $f(p)$, and $G(p)$ are defined in Eqs. (8.113), (8.117), and (8.186), respectively.

After shock crossing ($t > t_\times$), for the RS emission (taking $g = 1$), one has

$$\nu_{m,r} = (1.4 \times 10^{11} \text{ Hz}) \hat{z}^{6/7} \frac{G(p)}{G(2.3)} E_{52}^{6/7} A_{*, -1}^{-5/14} \Gamma_{0,2}^{-24/7} \epsilon_{e,-1}^2 \epsilon_{B,-2}^{1/2} t_2^{-13/7}, \quad (8.334)$$

$$\nu_{\text{cut}} = (7.4 \times 10^{10} \text{ Hz}) \hat{z}^{6/7} E_{52}^{20/7} \Gamma_{0,2}^{-66/7} A_{*, -1}^{-61/14} \epsilon_{B,-2}^{-3/2} t_2^{-13/7}, \quad (8.335)$$

$$F_{\nu, \max, r} = (1.6 \times 10^6 \text{ } \mu\text{Jy}) \hat{z}^{44/21} E_{52}^{23/21} A_{*, -1}^{17/42} \Gamma_{0,2}^{-29/21} \epsilon_{B,-2}^{1/2} D_{28}^{-2} t_2^{-23/21}, \quad (8.336)$$

$$\nu_{a,r} = (5.5 \times 10^{14} \text{ Hz}) \hat{z}^{-8/35} \frac{g^{\text{XX}}(p)}{g^{\text{XX}}(2.3)} E_{52}^{-12/35} \Gamma_{0,2}^{48/35} A_{*, -1}^{8/7} \epsilon_{e,-1}^{-1} \epsilon_{B,-2}^{1/5} t_2^{-23/35},$$

$$\nu_{a,r} < \nu_{m,r} < \nu_{\text{cut}}, \quad (8.337)$$

$$\nu_{a,r} = (5.5 \times 10^{14} \text{ Hz}) \hat{z}^{\frac{6p-4}{7(p+4)}} \frac{g^{\text{XXI}}(p)}{g^{\text{XXI}}(2.3)} E_{52}^{\frac{6p-4}{7(p+4)}} \Gamma_{0,2}^{\frac{16-24p}{7(p+4)}} A_{*, -1}^{\frac{50-5p}{14(p+4)}} \epsilon_{e,-1}^{\frac{2(p-1)}{p+4}} \epsilon_{B,-2}^{\frac{p+2}{2(p+4)}} t_2^{-\frac{13p+24}{7(p+4)}},$$

$$\nu_{m,r} < \nu_{a,r} < \nu_{\text{cut}}, \quad (8.338)$$

where

$$g^{\text{XX}}(p) = \left(\frac{p-1}{p-2} \right) (p+1)^{3/5} f(p)^{3/5}, \quad (8.339)$$

$$g^{\text{XXI}}(p) = 1.8 \times 10^{-\frac{26}{p+4}} \pi^{\frac{6}{p+4}} \left(\frac{p-2}{p-1} \right)^{\frac{2(p-1)}{p+4}} (p+1)^{\frac{2}{p+4}} f(p)^{\frac{2}{p+4}}, \quad (8.340)$$

and \hat{z} , $f(p)$, and $G(p)$ are defined in Eqs. (8.113), (8.117), and (8.186), respectively.

Characteristic Parameters: Thick Shells

For thick shells, before shock crossing ($t < t_{\times}$), for FS emission one has

$$\nu_{m,f} = (5.8 \times 10^{15} \text{ Hz}) \frac{G(p)}{G(2.3)} E_{52}^{1/2} \Delta_{0,13}^{-1/2} \epsilon_{e,-1}^2 \epsilon_{B,-2}^{1/2} t_2^{-1}, \quad (8.341)$$

$$\nu_{c,f} = (1.2 \times 10^{14} \text{ Hz}) \hat{z}^{-2} E_{52}^{1/2} \Delta_{0,13}^{-1/2} A_{*, -1}^{-2} \epsilon_{B,-2}^{-3/2} t_2, \quad (8.342)$$

$$F_{\nu, \max, f} = (5.0 \times 10^4 \text{ } \mu\text{Jy}) \hat{z} E_{52}^{1/2} \Delta_{0,13}^{-1/2} A_{*, -1}^{1/2} \epsilon_{B,-2}^{-2} D_{28}^{-2}, \quad (8.343)$$

$$\nu_{a,f} = (5.1 \times 10^{11} \text{ Hz}) \frac{g^{\text{VIII}}(p)}{g^{\text{VIII}}(2.3)} E_{52}^{-2/5} \Delta_{0,13}^{2/5} A_{*, -1}^{6/5} \epsilon_{e,-1}^{-1} \epsilon_{B,-2}^{1/5} t_2^{-1},$$

$$\nu_{a,f} < \nu_{m,f} < \nu_{c,f}, \quad (8.344)$$

$$\nu_{a,f} = (4.2 \times 10^{13} \text{ Hz}) \frac{g^{\text{IX}}(p)}{g^{\text{IX}}(2.3)} E_{52}^{\frac{p-2}{2(p+4)}} \Delta_{0,13}^{\frac{2-p}{2(p+4)}} A_{*, -1}^{\frac{4}{p+4}} \epsilon_{e,-1}^{\frac{2(p-1)}{p+4}} \epsilon_{B,-2}^{\frac{p+2}{2(p+4)}} t_2^{-1},$$

$$\nu_{m,f} < \nu_{a,f} < \nu_{c,f}, \quad (8.345)$$

$$\nu_{a,f} = (3.6 \times 10^{12} \text{ Hz}) \hat{z} \frac{g^{\text{X}}(p)}{g^{\text{X}}(2.3)} E_{52}^{-2/5} \Delta_{0,13}^{2/5} A_{*, -1}^{11/5} \epsilon_{B,-2}^{6/5} t_2^{-2},$$

$$\nu_{a,f} < \nu_{c,f} < \nu_{m,f}, \quad (8.346)$$

where

$$g^{\text{VIII}}(p) = \left(\frac{p-1}{p-2} \right) (p+1)^{3/5} f(p)^{3/5}, \quad (8.347)$$

$$g^{\text{IX}}(p) = 2^{\frac{105}{p+4}} e^{\frac{127}{p+4}} \pi^{\frac{3}{p+4}} \left(\frac{p-1}{p-2} \right)^{\frac{2(1-p)}{p+4}} (p+1)^{\frac{2}{p+4}} f(p)^{\frac{2}{p+4}}, \quad (8.348)$$

$$g^{\text{X}}(p) = (p+1)^{3/5} f(p)^{3/5}, \quad (8.349)$$

and \hat{z} , $f(p)$, and $G(p)$ are defined in Eqs. (8.113), (8.117), and (8.186), respectively.

For RS emission, one has

$$\nu_{m,r} = (3.3 \times 10^{13} \text{ Hz}) \frac{G(p)}{G(2.3)} E_{52}^{-1/2} A_{*, -1} \Gamma_{0,2}^2 \Delta_{0,13}^{1/2} \epsilon_{e,-1}^2 \epsilon_{B,-2}^{1/2} t_2^{-1}, \quad (8.350)$$

$$\nu_{c,r} = (1.2 \times 10^{14} \text{ Hz}) \hat{z}^{-2} E_{52}^{1/2} \Delta_{0,13}^{-1/2} A_{*, -1}^{-2} \epsilon_{B,-2}^{-3/2} t_2, \quad (8.351)$$

$$F_{\nu, \max, r} = (6.7 \times 10^5 \text{ } \mu\text{Jy}) \hat{z} E_{52}^{1/2} A_{*, -1} \Gamma_{0,2}^{-1} \Delta_{0,13}^{-1} \epsilon_{B,-2}^{1/2} D_{28}^{-2}, \quad (8.352)$$

$$\nu_{a,r} = (3.2 \times 10^{13} \text{ Hz}) \frac{g^{\text{VIII}}(p)}{g^{\text{VIII}}(2.3)} E_{52}^{2/5} \Gamma_{0,2}^{-8/5} A_{*, -1}^{2/5} \Delta_{0,13}^{-2/5} \epsilon_{e, -1}^{1/5} \epsilon_{B, -2}^{-1} t_2^{-1},$$

$$\nu_{a,r} < \nu_{m,r} < \nu_{c,r}, \quad (8.353)$$

$$\nu_{a,r} = (3.3 \times 10^{13} \text{ Hz}) \frac{g^{\text{IX}}(p)}{g^{\text{IX}}(2.3)} E_{52}^{\frac{2-p}{2(p+4)}} \Gamma_{0,2}^{\frac{2(p-2)}{p+4}} \Delta_{0,13}^{\frac{p-2}{2(p+4)}} A_{*, -1}^{\frac{p+2}{p+4}} \epsilon_{e, -1}^{\frac{2(p-1)}{p+4}} \epsilon_{B, -2}^{\frac{p+2}{2(p+4)}} t_2^{-1},$$

$$\nu_{m,r} < \nu_{a,r} < \nu_{c,r}, \quad (8.354)$$

$$\nu_{a,r} = (1.7 \times 10^{13} \text{ Hz}) \hat{z} \frac{g^{\text{X}}(p)}{g^{\text{X}}(2.3)} E_{52}^{-1/10} \Gamma_{0,2}^{-3/5} \Delta_{0,13}^{1/10} A_{*, -1}^{19/10} \epsilon_{B, -2}^{6/5} t_2^{-2},$$

$$\nu_{a,r} < \nu_{c,r} < \nu_{m,r}, \quad (8.355)$$

where

$$g^{\text{VIII}}(p) = \left(\frac{p-1}{p-2} \right) (p+1)^{3/5} f(p)^{3/5}, \quad (8.356)$$

$$g^{\text{IX}}(p) = 1.6 \times 10^{-\frac{100}{p+4}} 2^{-\frac{47}{p+4}} \pi^{-\frac{1}{p+4}} \left(\frac{p-2}{p-1} \right)^{\frac{2(p-1)}{p+4}} (p+1)^{\frac{2}{p+4}} f(p)^{\frac{2}{p+4}}, \quad (8.357)$$

$$g^{\text{X}}(p) = (p+1)^{3/5} f(p)^{3/5}, \quad (8.358)$$

and \hat{z} , $f(p)$, and $G(p)$ are defined in Eqs. (8.113), (8.117), and (8.186), respectively.

After shock crossing ($t > t_{\times}$), taking a BM profile, one has

$$\nu_{m,r} = (9.4 \times 10^{13} \text{ Hz}) \hat{z}^{7/8} \frac{G(p)}{G(2.3)} E_{52}^{-1/2} A_{*, -1}^2 \Gamma_{0,2}^2 \Delta_{0,13}^{11/8} \epsilon_{e, -1}^2 \epsilon_{B, -2}^{1/2} t_2^{-15/8}, \quad (8.359)$$

$$\nu_{\text{cut}} = (3.7 \times 10^{15} \text{ Hz}) \hat{z}^{7/8} E_{52}^{1/2} \Delta_{0,13}^{19/8} A_{*, -1}^{-2} \epsilon_{B, -2}^{-3/2} t_2^{-15/8}, \quad (8.360)$$

$$F_{\nu, \text{max}, r} = (2.6 \times 10^6 \text{ } \mu\text{Jy}) \hat{z}^{17/8} E_{52}^{1/2} A_{*, -1}^{-1} \Gamma_{0,2}^{-1} \Delta_{0,13}^{1/8} \epsilon_{B, -2}^{1/2} D_{28}^{-2} t_2^{-9/8}, \quad (8.361)$$

$$\nu_{a,r} = (1.9 \times 10^{13} \text{ Hz}) \hat{z}^{-2/5} \frac{g^{\text{XX}}(p)}{g^{\text{XX}}(2.3)} E_{52}^{2/5} \Gamma_{0,2}^{-8/5} A_{*, -1}^{2/5} \Delta_{0,13}^{-4/5} \epsilon_{e, -1}^{-1} \epsilon_{B, -2}^{1/5} t_2^{-3/5},$$

$$\nu_{a,r} < \nu_{m,r} < \nu_{\text{cut}}, \quad (8.362)$$

$$\nu_{a,r} = (4.1 \times 10^{13} \text{ Hz}) \hat{z}^{\frac{7p-6}{8(p+4)}} \frac{g^{\text{XXI}}(p)}{g^{\text{XXI}}(2.3)} E_{52}^{\frac{2-p}{2(p+4)}} \Gamma_{0,2}^{\frac{2(p-2)}{p+4}} \Delta_{0,13}^{\frac{11p-14}{8(p+4)}} A_{*, -1}^{\frac{p+2}{p+4}}$$

$$\times \epsilon_{e, -1}^{\frac{2(p-1)}{p+4}} \epsilon_{B, -2}^{\frac{p+2}{2(p+4)}} t_2^{-\frac{15p+26}{8(p+4)}}, \quad \nu_{m,r} < \nu_{a,r} < \nu_{\text{cut}}, \quad (8.363)$$

where

$$g^{\text{XX}}(p) = \left(\frac{p-1}{p-2} \right) (p+1)^{3/5} f(p)^{3/5}, \quad (8.364)$$

$$g^{\text{XXI}}(p) = 5.7 \times 10^{-\frac{82}{p+4}} 2^{\frac{19}{2(p+4)}} 3^{\frac{9}{4(p+4)}} 5^{\frac{21}{2(p+4)}} \pi^{-\frac{1}{p+4}}$$

$$\times \left(\frac{p-2}{p-1} \right)^{\frac{2(p-1)}{p+4}} (p+1)^{\frac{2}{p+4}} f(p)^{\frac{2}{p+4}}, \quad (8.365)$$

and \hat{z} , $f(p)$, and $G(p)$ are defined in Eqs. (8.113), (8.117), and (8.186), respectively.

8.8 Other Effects

8.8.1 Effect of Neutron Decay

As discussed in §7.3.5, the existence of neutrons in a fireball introduces interesting dynamics and observational signatures. The impact on the early afterglow of neutron decay has been studied in detail by Beloborodov (2003a) and Fan et al. (2005a). The basic conclusions are the following:

- Since neutrons do not decelerate in the internal shocks, they stream ahead of the proton shells, and leave a decay trail in front of the proton shells.
- The proton shells shock into the decay trail of the neutron shells and give rise to an interesting re-brightening signature in the early afterglow phase.
- Since the afterglow onset distance is different for the ISM and wind models, the neutron-decay-induced signature is very different in the two cases (Fan et al., 2005a). For a constant density (ISM) model, the neutron-rich early afterglow is characterized by a slowly rising lightcurve followed by a sharp re-brightening bump caused by a collision between the leading neutron decay trail ejecta and the trailing ion ejecta. For a stellar wind model, the neutron-rich early afterglow shows an extended plateau lasting for about 100 s before the lightcurve starts to decay. The plateau is mainly attributed to the emission from the unshocked neutron decay trail.

8.8.2 Radiation Front

The γ -ray photons released during the prompt emission phase travel faster than the relativistic outflow itself. These photons would interact with the ambient medium before the outflow shocks into the medium. The medium profile would therefore be modified from the original one, which would modify the properties of early afterglow emission. This problem has been studied by many authors, e.g. Madau and Thompson (2000), Thompson and Madau (2000), Mészáros et al. (2001), and Beloborodov (2002). Generally, there are two effects. First, as some photons scatter off electrons in the medium, they deposit momentum to protons so that the ambient medium moves forward. Second, some photons are back scattered so that they would interact with the later incoming photons to produce electron-positron pairs. The pairs would be swept by the shock later so that the forward shock would be pair rich. The effect is more important if the ambient density is high. As a result, the effect may be more relevant for GRBs running into a dense stellar wind.

Beloborodov (2002) studied the process in detail and reached the following conclusions:

- The γ -ray photons clear up a gap within a distance $R_{\text{gap}} \simeq 10^{16} E_{54}^{1/2}$ cm. The ejecta moves freely in this cavity and starts to interact with the medium beyond R_{gap} .
- Pairs are loaded all the way to $R_{\text{load}} \sim 5R_{\text{gap}}$. Blastwave emission at $R < R_{\text{load}}$ is impacted.

- For long GRBs in an ISM medium, both R_{gap} and R_{load} are well below R_{dec} . So the standard afterglow model works well. For a wind medium, significant modification of the medium profile is expected.

8.8.3 Evolution of Shock Microphysics Parameters

In the standard afterglow model, ϵ_e and ϵ_B are taken as constant. There is no reason why they should not evolve with the strength of the shocks. Introducing their temporal evolution gives a more complicated afterglow model, with more freedom in parameters. Such a model has been investigated by some authors (e.g. Ioka et al., 2006; Fan and Piran, 2006a; Granot et al., 2006) prompted by the discovery of the shallow decay phase in early X-ray afterglows. The many free parameters introduced are hard to constrain from data in these models. The current data do not demand such models (see more discussion in §8.10).

8.9 Afterglow Polarization

According to the synchrotron polarization theory (§5.1.9), synchrotron emission can be strongly polarized in an ordered magnetic field, but the overall polarization can be cancelled out if the magnetic fields are randomized. In GRB problems, what matters is the average magnetic configuration within the $1/\Gamma$ cone. For FS emission, the B field is likely generated from plasma instabilities, so that the B configuration is randomized (e.g. Medvedev and Loeb, 1999; Nishikawa et al., 2005, 2009). Late optical afterglow observations indeed show low polarization degrees of several percent or upper limits of the polarization degrees (Covino et al., 2003), which is consistent with such a picture. The origin of non-vanishing Π in afterglow emission may be due to the following reasons: first, the magnetic field coherent length may grow after the field is generated at the shock front. According to Gruzinov and Waxman (1999), this mechanism may produce a polarization degree of 1–10%. Second, the emission per unit solid angle within the $1/\Gamma$ cone may not be isotropic, so that the average B configuration within the $1/\Gamma$ cone is not completely cancelled out. This is relevant, e.g. for a conical jet with line of sight mis-aligned with the jet axis or for a structured jet. Depending on the jet configuration and viewing angle, the polarization degree and polarization angle would follow a predictable evolutionary behavior (e.g. Ghisellini and Lazzati, 1999; Sari, 1999; Rossi et al., 2004; Wu et al., 2005a). The observed polarization lightcurves are, however, usually more complicated than the simple predictions, suggesting that the polarization may be related to more complicated effects, e.g. the jet structure or medium density distribution within the $1/\Gamma$ cone may be much more complicated than usually assumed.

For ordered magnetic fields, theory predicts up to $\sim 70\%$ polarization (§5.1.9). If one considered the relativistic aberration effect, within the $1/\Gamma$ cone the B field configuration would be distorted and the maximum polarization degree would be reduced to $\Pi \sim 40\text{--}60\%$ (e.g. Lazzati, 2006).

Early optical afterglow observations revealed interesting polarization signatures. GRB 060418 showed a Type III (FS dominated, Fig. 8.12) lightcurve, which was observed at

203 s after the trigger and an upper limit $\Pi < 8\%$ was derived (Mundell et al., 2007). This is consistent with the FS synchrotron origin of the afterglow, in which no significant ordered B field is expected. GRB 090102, on the other hand, had a Type II (RS dominated, Fig. 8.12) lightcurve. At 161–221 s (which is the RS-dominated phase), a positive detection $\Pi = 10 \pm 2\%$ was made (Steele et al., 2009), suggesting a possible ordered B field component in the emission region. This is consistent with the expectation of a more magnetized RS as revealed through afterglow lightcurve modeling (Fan et al., 2002; Zhang et al., 2003a; Kumar and Panaitescu, 2003). GRB 120308A, another GRB with a Type II lightcurve, was found to have a polarization degree evolving from $\Pi = 28 \pm 4\%$ at 4 minutes after trigger to $(10^{+5}_{-4})\%$ at 10 minutes after the trigger (Mundell et al., 2013). This is consistent with the transition from the RS-dominated phase to the FS-dominated phase (Lan et al., 2016), again consistent with a (not completely) ordered B field in the ejecta. Compared with an even higher polarization degree of γ -ray emission during the prompt emission phase (e.g. Yonetoku et al., 2011, 2012), these results suggest that magnetic field configuration may be partially randomized during the prompt emission phase, consistent with the suggestion that prompt magnetic dissipation would partially (but not completely) destroy the ordered field configuration (e.g. Zhang and Yan, 2011; Deng et al., 2015).

8.10 Theory Confronting Observations

8.10.1 External Shock Model in Perspective

Pre-*Swift* Era

The detailed afterglow theory predated the discovery (Mészáros and Rees, 1997a). The model correctly predicted the general behavior of multi-wavelength afterglow, and therefore has been a great triumph. Later, more detailed observations revealed rich features, forcing the afterglow model to expand to include more ingredients (RS vs. FS, ISM vs. wind, energy injection, jet effect, non-relativistic transition, density fluctuations, patchy jet, etc). In any case, there were no fundamental challenges to the external shock afterglow theory in the pre-*Swift* era. Modeling the broad-band data of afterglow emission was carried out for the handful of GRBs known back then, and the success of the model was claimed (e.g. Wijers et al., 1997; Wijers and Galama, 1999; Panaitescu and Kumar, 2001, 2002; Yost et al., 2003).

Post-*Swift* Era

Swift opened a window to study the early phase of GRB afterglows. The XRT regularly records the early X-ray lightcurves of the majority of GRBs, which show rich features characterized by five temporal components (Zhang et al., 2006; Nousek et al., 2006), see §2.2.2 for details. Whereas the steep decay phase (Component I) and flares (Component V) are linked to the central engine activities, the shallow decay phase (II), the normal decay phase (III), and the late steepening (IV) likely originate from the external

shock, with II originating from energy injection, and IV originating from jet break (Zhang et al., 2006). Such a general picture is consistent with the data of some GRBs. However, it was soon discovered (Panaiteescu et al., 2006a) that a fraction of GRBs show “chromatic” behavior in the X-ray and optical bands. The so-called chromatic behavior states that the two bands behave independently. In particular, when one band (e.g. the X-ray) shows a temporal break, the other band (e.g. the optical) does not show a temporal break at all, or shows a break at a different epoch. Within the afterglow theory, this is allowed if the temporal break is caused by the crossing of a characteristic frequency (e.g. ν_m , ν_c) in the band. However, if this is the case, one would expect a change of spectral index before and after that temporal break. The X-ray afterglow observations, on the other hand, insist that the X-ray photon index remains unchanged before and after the break, between segments II and III or between segments III and IV (Liang et al., 2007b, 2008a). The chromatic behavior in some GRBs therefore posed a *fundamental challenge* to the external shock afterglow model in general. It demands two independent emission components to power the emission in the X-ray and optical bands. A simple fix was to introduce two external shock components (e.g. De Pasquale et al., 2009). However, the demanded parameters for the two components are extremal, and are different from burst to burst, suggesting that this is not an elegant solution. Various authors introduced non-forward-shock models to interpret the X-ray afterglow. Uhm and Beloborodov (2007) and Genet et al. (2007) independently suggested that the entire afterglow may be from a long-lasting RS instead of FS. This model needs to suppress the FS emission significantly (by default, the FS emission outshines the RS emission by about 2 orders of magnitude). Many authors (e.g. Ghisellini et al., 2007; Kumar et al., 2008b,a; Cannizzo and Gehrels, 2009; Lindner et al., 2010; Yu et al., 2010) suggested that most X-ray emission may be directly powered by a decaying central engine, with the emission generated through internal dissipation of the central engine wind. Some other authors (Shao and Dai 2007, but see Shen et al. 2009) invoked external dust scattering to account for the observed X-rays.

How Good/Bad Are the External Shock Models?

Wang et al. (2015b) carried out a comprehensive systematic study of GRB afterglows. By collecting a large sample of GRBs whose X-ray and optical lightcurves are well detected, they confronted the observational data with the external shock afterglow models. Out of 85 GRBs studied, they found more than half (45) are consistent with being “achromatic” and also having temporal decay indices (α) and spectral indices (β) satisfying the model predictions (closure relations, see also Li et al. 2015). Another 37 events are still consistent with being achromatic, even though in at least one temporal segment, in one band, the closure relations are not fully satisfied. By considering more complicated models (e.g. long-lasting RS or structured jet), these GRBs may also be consistent with the external shock models. Only a small fraction (less than 10%) completely violated the principle of the external shock model and require an additional emission component not from the external shock. This study suggests that the external shock model is still valid for the majority of GRBs (at least 50% and up to 90%).

The standard reverse shock model can interpret the early optical, radio, and sometimes GeV observations of a good sample of GRBs, usually with the requirement that the RS is more magnetized than the FS (Fan et al., 2002; Zhang et al., 2003a; Kumar and Panaitescu, 2003; Gomboc et al., 2008; Japelj et al., 2014; Kopač et al., 2015; Gao et al., 2015a; Fraija, 2015; Fraija et al., 2016, 2017).

8.10.2 Model Parameter Constraints from Data

Within the framework of the external shock model, the parameters of the model may be constrained. As shown in §4.6, the shock can be parameterized with several parameters. For FS afterglow emission, data show no evidence of only a small fraction of particles being accelerated, so that both ξ_e and ξ_p are usually taken as unity. For the standard FS model (constant energy), there are six fundamental parameters: the isotropic kinetic energy $E_{K,\text{iso}}$, the density parameter (n for the ISM model or A for the wind model), the jet opening angle (θ_j), and three microphysics parameters (ϵ_e , ϵ_B , and p). Out of these parameters, θ_j enters only when a jet break is detected. The parameter p may be directly measured from the spectral index if one knows the spectral regime of the observational band where the afterglow is observed (e.g. through a closure-relation analysis). The other four parameters ($E_{K,\text{iso}}$, n or A , ϵ_e , and ϵ_B) can be measured once an instantaneous broad-band spectral energy distribution (SED) is constructed (so that $F_{\nu,\text{max}}$, ν_m , ν_c , ν_a are measured).

In reality, only a small sample of GRBs might have enough observed information to pin down all the parameters (e.g. Panaitescu and Kumar, 2001, 2002; Yost et al., 2003). In most cases, one either has incomplete spectral coverage or incomplete temporal coverage, so that an instantaneous SED is not available. For these cases, one has to assume the values of some parameters (e.g. ϵ_e , ϵ_B) to derive other parameters.

One important parameter is $E_{K,\text{iso}}$. It is directly related to the afterglow energetics and the radiative efficiency of prompt emission. It was noticed (Kumar, 1999; Freedman and Waxman, 2001) that above ν_c (e.g. in the X-ray band), the afterglow flux does not depend on n and only weakly depends on ϵ_B , so that the afterglow flux can give a robust measure of $\epsilon_e E_{K,\text{iso}}$. Since data show that ϵ_e is not too small (around 0.1), $E_{K,\text{iso}}$ can be estimated. If the observational frequency is below ν_c , an expression of $E_{K,\text{iso}}$ can be also derived, with explicit dependence on microphysics parameters.

An interesting constraint on ϵ_B may be achieved by considering the location of the cooling frequency ν_c . A high enough ν_c suggests that the magnetic field strength cannot be too high, which poses an upper limit on ϵ_B .

Since the X-ray band has plenty of observational data, it is convenient to write down the expressions of $E_{K,\text{iso}}$ and ϵ_B in terms of observational quantities in different medium models and spectral regimes (Zhang et al., 2007a; Wang et al., 2015b).

For the ISM medium and $\nu > \nu_c$, one has

$$\begin{aligned}
 E_{K,\text{iso},52} = & \left(\frac{\nu F_\nu(\nu = 10^{18} \text{ Hz})}{5.2 \times 10^{-14} \text{ erg s}^{-1} \text{ cm}^{-2}} \right)^{4/(p+2)} D_{28}^{8/(p+2)} (1+z)^{-1} \\
 & \times (1+Y)^{4/(p+2)} f_{p1}^{-4/(p+2)} \epsilon_{B,-2}^{(2-p)/(p+2)} \\
 & \times \epsilon_{e,-1}^{4(1-p)/(p+2)} t_d^{(3p-2)/(p+2)} \nu_{18}^{2(p-2)/(p+2)}, \quad (8.366)
 \end{aligned}$$

and

$$\begin{aligned} \epsilon_{B,-2} = & \left(\frac{6.3 \times 10^{15} \text{ Hz}}{\nu_c} \right)^{(p+2)/(p+4)} \left(\frac{\nu F_\nu(\nu = 10^{18} \text{ Hz})}{5.2 \times 10^{-14} \text{ erg s}^{-1} \text{ cm}^{-2}} \right)^{-2/(p+4)} \\ & \times D_{28}^{-4/(p+4)} (1+Y)^{-2(p+3)/(p+4)} n^{-(p+2)/(p+4)} \\ & \times f_{p1}^{2/(p+4)} \epsilon_{e,-1}^{2(p-1)/(p+4)} t_d^{-2p/(p+4)} \nu_{18}^{(2-p)/(p+4)}, \end{aligned} \quad (8.367)$$

where

$$f_{p1} = 6.73 \left(\frac{p-2}{p-1} \right)^{p-1} (3.3 \times 10^{-6})^{(p-2.3)/2} \quad (8.368)$$

is a function of electron spectral index p ;

$$Y = [-1 + (1 + 4\eta_1\eta_2\epsilon_e/\epsilon_B)^{1/2}]/2 \quad (8.369)$$

is the inverse Compton parameter, with $\eta_1 = \min[1, (\nu_c/\nu_m)^{(2-p)/2}]$ (Sari and Esin, 2001); and $\eta_2 \leq 1$ is a correction factor introduced by the Klein–Nishina correction. For $\nu_m < \nu < \nu_c$, one has

$$\begin{aligned} E_{K,\text{iso},52} = & \left(\frac{\nu F_\nu(\nu = 10^{18} \text{ Hz})}{6.5 \times 10^{-13} \text{ erg s}^{-1} \text{ cm}^{-2}} \right)^{4/(p+3)} D_{28}^{8/(p+3)} (1+z)^{-1} \\ & \times f_{p1}^{-4/(p+3)} \epsilon_{B,-2}^{-(p+1)/(p+3)} \epsilon_{e,-1}^{4(1-p)/(p+3)} n^{-2/(p+3)} \\ & \times t_d^{(3p-3)/(p+3)} \nu_{18}^{2(p-3)/(p+3)}, \end{aligned} \quad (8.370)$$

$$\begin{aligned} \epsilon_{B,-2} = & \left(\frac{6.3 \times 10^{15} \text{ Hz}}{\nu_c} \right)^{(p+3)/(p+4)} \left(\frac{\nu F_\nu(\nu = 10^{18} \text{ Hz})}{6.5 \times 10^{-13} \text{ erg s}^{-1} \text{ cm}^{-2}} \right)^{-2/(p+4)} \\ & \times D_{28}^{-4/(p+4)} (1+Y)^{-2(p+3)/(p+4)} n^{-(p+2)/(p+4)} \\ & \times f_{p1}^{2/(p+4)} \epsilon_{e,-1}^{2(p-1)/(p+4)} t_d^{-2p/(p+4)} \nu_{18}^{(3-p)/(p+4)}. \end{aligned} \quad (8.371)$$

Similar equations can be derived for the wind model. For $\nu > \nu_c$, one has

$$\begin{aligned} E_{K,\text{iso},52} = & \left(\frac{\nu F_\nu(\nu = 10^{18} \text{ Hz})}{2.6 \times 10^{-13} \text{ erg s}^{-1} \text{ cm}^{-2}} \right)^{4/(p+2)} D_{28}^{8/(p+2)} (1+z)^{-1} \\ & \times (1+Y)^{4/(p+2)} f_{p4}^{-4/(p+2)} \epsilon_{B,-2}^{(2-p)/(p+2)} \epsilon_{e,-1}^{4(1-p)/(p+2)} \\ & \times t_d^{(3p-2)/(p+2)} \nu_{18}^{2(p-2)/(p+2)}, \end{aligned} \quad (8.372)$$

$$\begin{aligned} \epsilon_{B,-2} = & \left(\frac{1.7 \times 10^{18} \text{ Hz}}{\nu_c} \right)^{(p+2)/(2p+2)} \left(\frac{\nu F_\nu(\nu = 10^{18} \text{ Hz})}{2.6 \times 10^{-13} \text{ erg s}^{-1} \text{ cm}^{-2}} \right)^{1/(p+1)} \\ & \times D_{28}^{2/(p+1)} (1+z)^{-(p+2)/(p+1)} (1+Y)^{-1} f_{p4}^{-1/(p+1)} \epsilon_{e,-1}^{(1-p)/(p+1)} \\ & \times A_{*, -1}^{-(p+2)/(p+1)} t_d^{p/(p+1)} \nu_{18}^{(p-2)/2(p+1)}, \end{aligned} \quad (8.373)$$

where

$$f_{p4} = 6.73 \left(\frac{p-2}{p-1} \right)^{p-1} (5.2 \times 10^{-7})^{(p-2.3)/2}. \quad (8.374)$$

For $\nu_m < \nu < \nu_c$, one has

$$\begin{aligned} E_{K,\text{iso},52} = & \left(\frac{\nu F_\nu(\nu = 10^{18} \text{ Hz})}{2.0 \times 10^{-13} \text{ erg s}^{-1} \text{ cm}^{-2}} \right)^{4/(p+1)} D_{28}^{8/(p+1)} \\ & \times (1+z)^{-(p+5)/(p+1)} f_{p4}^{-4/(p+1)} \epsilon_{B,-2}^{-1} \epsilon_{e,-1}^{4(1-p)/(p+1)} \\ & \times A_{*, -1}^{-4/(p+1)} t_d^{(3p-1)/(p+1)} \nu_{18}^{2(p-3)/(p+1)}, \end{aligned} \quad (8.375)$$

$$\begin{aligned} \epsilon_{B,-2} = & \left(\frac{1.7 \times 10^{18} \text{ Hz}}{\nu_c} \right)^{1/2} \left(\frac{\nu F_\nu(\nu = 10^{18} \text{ Hz})}{2.0 \times 10^{-13} \text{ erg s}^{-1} \text{ cm}^{-2}} \right)^{1/(p+1)} \\ & \times D_{28}^{2/(p+1)} (1+z)^{-(p+2)/(p+1)} (1+Y)^{-1} A_{*, -1}^{-(p+2)/(p+1)} \\ & \times f_{p4}^{-1/(p+1)} \epsilon_{e,-1}^{(1-p)/(p+1)} t_d^{p/(p+1)} \nu_{18}^{(p-3)/2(p+1)}. \end{aligned} \quad (8.376)$$

Afterglow modeling led to constraints on model parameters. The general conclusions from these analyses (e.g. Panaitescu and Kumar, 2001, 2002; Yost et al., 2003; Zhang et al., 2007a; Wang et al., 2015b; Gao et al., 2015a) are the following:

- The microphysics parameters are not universal. The p distribution is consistent with a Gaussian distribution peaking at ~ 2.3 (e.g. Fig. 4.7). The ϵ_e and ϵ_B parameters, especially the latter, vary in a much wider range. Whereas earlier modeling (Panaitescu and Kumar, 2001, 2002) derived $\epsilon_B \sim 10^{-2}$ – 10^{-3} , later studies showed that ϵ_B can be as low as 10^{-6} (e.g. Kumar and Barniol Duran, 2009; Santana et al., 2014; Wang et al., 2015b). From individual modeling, the preferred ϵ_e value is around 0.1 (Wijers and Galama, 1999; Panaitescu and Kumar, 2001, 2002). However, a morphological study of early optical lightcurves suggests a preferred value of ~ 0.01 (Gao et al., 2015a).
- The inferred isotropic blastwave kinetic energy $E_{K,\text{iso}}$ has a wide distribution (e.g. Wang et al., 2015b). However, it usually scales with the isotropic γ -ray energy $E_{\gamma,\text{iso}}$ released during the prompt emission. The radiative efficiency $\eta = E_{\gamma,\text{iso}}/(E_{\gamma,\text{iso}} + E_{K,\text{iso}})$ varies in a wide range, and also depends on whether $E_{K,\text{iso}}$ is estimated right after prompt emission (beginning of the shallow decay phase) or at the end of the shallow decay phase. According to Zhang et al. (2007a) and Wang et al. (2015b), η can be as high as $>90\%$, with a typical value of tens of percent, if an early epoch is adopted to estimate $E_{K,\text{iso}}$. If one adopts a later epoch to estimate $E_{K,\text{iso}}$, η can still be tens of percent, but with a typical value of several percent. A smaller ϵ_e (Gao et al., 2015a) would imply an even lower η . There is no clear correlation between η and $E_{\gamma,\text{iso}}$.
- The typical jet opening angle is a few degrees (Frail et al., 2001; Wang et al., 2015b). After jet-beaming correction, the γ -ray and kinetic energies (E_γ and E_K) peak around 10^{50} – 10^{51} erg. The distributions are narrower than the isotropic energies, but still span a range of 3–4 orders of magnitude.

Exercises

- 8.1 Derive the dynamical scaling relations for a blastwave with arbitrary medium stratification parameter k and energy injection parameter q .
- 8.2 Derive the blastwave scaling laws for Blandford–McKee solutions in a constant energy, constant density model, i.e. Eqs. (8.38) and (8.39).
- 8.3 Apply Eq. (8.73) to the treatment of fast cooling in a decaying magnetic field as discussed in §5.1.5, and prove that the asymptotic electron spectral index is $-(6b - 4)/(6b - 1)$ rather than $-(2b - 2)/(2b - 1)$.
- 8.4 Check the $\hat{z} = (1 + z)$ dependences in the expressions of v_a in Eqs. (8.110)–(8.112).
- 8.5 Derive the α and β for all the regimes of the constant energy wind model in the deceleration phase.
- 8.6 Derive the expression of jet opening angle for the constant energy wind model.
- 8.7 Derive the afterglow decay indices for an on-beam power-law structured jet for both the ISM and wind models, i.e. Eqs. (8.163) and (8.164).
- 8.8 Derive the temporal decay indices of a blastwave for different slow cooling spectral regimes in the non-relativistic phase, i.e. Eq. (8.180).
- 8.9 Derive the α and β values for both FS and RS-emission during the RS-crossing phase, and those of RS emission after RS crossing, as presented in the various tables in this chapter.
- 8.10 Derive the scaling laws of the characteristic parameters for RS emission in the wind model.